Developments for broadband spectral and spatial characterization of tin plasma light sources for EUV lithography

Zoi Bouza

Developments for broadband spectral and spatial characterization of tin plasma light sources for EUV lithography

Zoi Bouza

Ph.D. thesis, Vrije Universiteit Amsterdam, 2023
Developments for broadband spectral and spatial characterization of tin plasma light sources for EUV lithography
Zoi Bouza
ISBN: 978-94-6469-500-7

An electronic version of this dissertation is available at: research.vu.nl
Print: ProefschriftMaken, www.proefschriftmaken.nl

VRIJE UNIVERSITEIT

DEVELOPMENTS FOR BROADBAND SPECTRAL AND SPATIAL CHARACTERIZATION OF TIN PLASMA LIGHT SOURCES FOR EUV LITHOGRAPHY

ACADEMISCH PROEFSCHRIFT

ter verkrijging van de graad Doctor of Philosophy aan
de Vrije Universiteit Amsterdam,
op gezag van de rector magnificus
prof.dr. J.J.G. Geurts,
in het openbaar te verdedigen
ten overstaan van de promotiecommissie
van de Faculteit der Bètawetenschappen
op vrijdag 6 oktober 2023 om 11.45 uur
in een bijeenkomst van de universiteit,
De Boelelaan 1105

door

Zoi Bouza

geboren te Patras, Griekenland

promotoren:	dr. O.O. Versolato prof.dr. W.M.G. Ubachs prof.dr.ir. R.A. Hoekstra
copromotor:	dr. M. Bayraktar
promotiecommissie:	prof.dr. A.J. den Boef dr. L.V. Amitonova prof.dr. P. Dunne prof.dr. M.D. Ackermann prof.dr. P.C.M. Planken

The research reported in this thesis was funded by TKI-HTSM with the project name "Spectral Unraveling of EUV Lithography Light Sources (SUN)" carried out in part at the Advanced Research Center for Nanolithography (ARCNL), a public-private partnership between the University of Amsterdam (UvA), Vrije Universiteit Amsterdam (VU Amsterdam), the Netherlands Organization for Scientific Research (NWO), and the semiconductor equipment manufacturer ASML. The transmission grating spectrometer was developed in the Industrial Focus Group XUV Optics at the University of Twente in Enschede, The Netherlands.

Cover: For the cover I would like to thank dr. Oscar O. Versolato and dr. Christos Messinis.

To my family...

Contents

Chapter 1

Introduction

In our times, most of the population uses electronic equipment, such as smartphones, computers, cars, or household equipment, and every year there are demands and expectations for further improvements in such devices. Having started from a single transistor on a chip in 1947, current semiconductor technology is now capable of fabricating billions of transistors of nanometer dimensions on a computer chip [1]. This fact offers humanity among others, better quality, faster, and more energy-efficient devices. The progress of the semiconductor industry follows the well-known Moore's law [2] according to which the number of transistors in a dense integrated circuit doubles roughly every two years.

Semiconductor devices are fabricated using a repetitive photochemical process. In this process, thin layers of different materials are first deposited onto a silicon wafer, then patterned, and finally etched via a chemical procedure. In this repetitive process, photolithography occurs when features of a mask are finely patterned onto a photosensitive layer with light. The wavelength of this light determines the minimum size of the features that can be patterned onto the photosensitive layer. The shorter the wavelength, the smaller the features that can be imprinted [3]. In the Rayleigh criterion equation, the critical dimension (CD) expresses the smallest reachable feature size:

$$\mathrm{CD} = k_1 \cdot \frac{\lambda}{\mathrm{NA}}, \tag{1.1}$$

where the k_1 is a constant related to the chip manufacturing process, λ is the wavelength of the in-use light and NA is the numerical aperture that defines the range of angles over which the system can accept or emit light. As we will motivate in the following, it is important to understand the spectral and spatial characteristics of the source providing the light, as well as those of the optics used.

1.1 Tin laser-produced plasma as light source in semiconductor industry

Starting from 436 nm wavelength light used in photolithography back in 1985, ever shorter wavelengths have been used during the subsequent years in the drive to minimize features on chips. A prominent example is deep ultraviolet (DUV) lithography which uses light at 193 nm wavelength to drive Moore's law for over 20 years. From 2018 onward an extreme ultraviolet (EUV) wavelength of just 13.5 nm was introduced in high-volume manufacturing of semiconductor devices [3]. The EUV light at 13.5 nm wavelength is generated when a high-intensity laser pulse interacts with tin microdroplets, leading to the creation of a dense and hot plasma [4, 5, 6, 7, 8, 9, 10].

The latest generations of plasma light sources used in lithography use a two-step process to increase the EUV production efficiency. First, a low-energy pre-pulse deforms the tin microdroplets into disk-like shapes [5, 11, 12]. Next, a high-energy main pulse hits the pre-shaped droplets, producing a plasma that generates the required EUV light [5, 4]. Currently, the industry uses 10.6-µm-wavelength CO_2 gas lasers to provide the pulses [5]. Tin plasma produced by CO_2 gas lasers is characterized by a high conversion efficiency of drive laser power to lithographically useful EUV light. However, CO_2 gas lasers are not the most efficient option in terms of converting electrical power into laser power. Using solid-state lasers instead of the CO_2 gas lasers may lead to higher overall efficiency, more stability, and better scalability of EUV source power [13]. For example, the 1-µm-wavelength solid-state Nd:YAG laser has been rather extensively studied for driving plasma [14, 15, 16]. Recent studies have also focused on 2-µm-wavelength solid-state lasers which have been shown to have a better conversion efficiency than the 1-µm-wavelength lasers [13, 17].

Tin laser-produced plasma (LPP) is characterized by a strong emission peak around 13.5 nm, originating from transitions between complex excited states in multiply charged Sn^{8+}–Sn^{14+} ions [18, 19, 20, 21, 22, 23, 24, 25, 26, 27]. Such plasma however also inherently radiates over a broader spectral range from soft x-rays to the visible. The lithographically useful wavelength region is defined as 13.5 nm$\pm$1% and called the "in-band" (IB). This $\pm$1% bandwidth originates from the in-use optics (see below). Light emitted outside of this in-band range is referred to as out-of-band radiation. However, not only in-band radiation is transmitted from the light source to the wafer through the photolithography optics. In the following, spectral characteristics of the photolithography optics are explained, not only in the EUV but in the full range from soft x-rays to infrared wavelengths.

1.2 Spectral characteristics of photolithography optics

The EUV light is transmitted from the LPP light source to the wafer using multilayer mirrors (MLMs), made from molybdenum/silicon (Mo/Si), which are designed to efficiently reflect in-band EUV light. Mo/Si MLMs however also have significant reflectance at longer wavelengths as shown in Fig. 1.1. The reflectance (R), absorbance (A), and transmittance (T) shown in the figure are calculated using the IMD computer code for a representative 50-period Mo/Si multilayer mirror coating with a period of 6.9 nm and a thickness ratio of 0.4 Mo to a period in normal incidence geometry [28]. The refractive indices of Mo and Si are taken from Ref. [29] and Ref. [30], respectively, for below and above 65 nm.

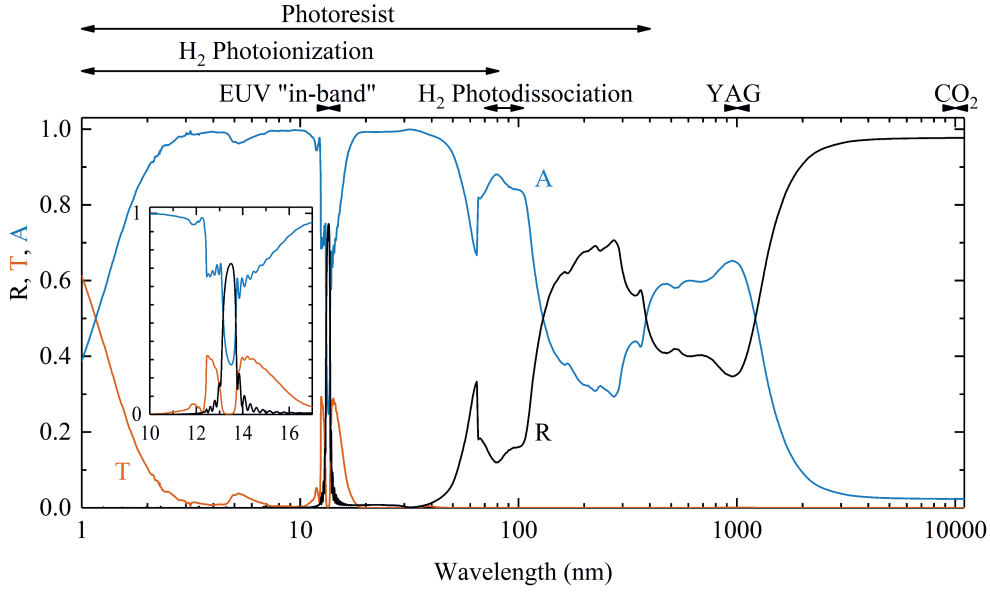

Figure 1.1: Calculated reflectance (R), transmission (T), and absorbance (A) of a 50-period Mo/Si multilayer mirror. The relevant physical phenomena at different wavelength bands are also indicated at the top (see main text).

Below 10 nm the reflectance drops to insignificant values. In the same range, we notice that the absorbance is dominant. The range from ∼13 to 14 nm around the in-band (see inset) can be reflected by Mo/Si multilayer mirrors. Constructive interference of the reflections from the numerous Mo/Si interfaces leads to a high (optimally ∼70%) but narrow (∼13–14 nm) reflection peak. It is the use of several (∼10) mirrors under several incident angles that in the end results in the aforementioned

acceptance bandwidth of 13.5 nm$\pm$1%. In this ($\sim$13–14 nm) range of interference the absorbance and transmittance have a dip at the peak position of the reflectance. In the absorbance curve in the inset, it is also possible to see the Si-L absorption edge at $\sim$12.4 nm, below which the absorbance significantly increases. Beyond this range and up to $\sim$40 nm, light is not reflected from the mirrors, but it is absorbed by them, something that could cause heating and lifetime problems in the optics.

Inspecting the even longer wavelengths in the figure, the reflectance starts to increase. The sharp feature at $\sim$65 nm is due to the concatenation of two data sets for the refractive index of Mo, therefore we attribute this sharp feature to a systematic uncertainty – not a physical effect. Beyond this feature and especially above 100 nm the reflectance of mirrors increases, with the transmission at zero level while absorbance decreases. Between $\sim$130 and $\sim$400 nm, the reflectance is higher than the absorbance and exceeds 60% in most of the range, and light is reflected almost as effectively as the in-band EUV. Above this range, the reflectance first decreases before increasing again at $\sim$1000 nm all the way up to $\sim$10000 nm (note that these two wavelengths correspond to the emission wavelengths of the in-use Nd:YAG and CO_2 laser systems). In summary, Mo/Si MLMs have a strong but narrow reflectance peak at 13.5 nm but also significantly reflect at longer wavelengths. Light at such longer wavelengths may be relevant for certain physical processes due to the operating environment and materials used in the photolithography systems as explained in the following.

In photolithography systems, H_2 is used as a buffer gas mainly to prevent damage to optics from the fast ions generated in the violently expanding plasma. This gas also interacts with the light generated by the LPP. Moving down in wavelength, the gas will start absorbing the light significantly for wavelengths shorter than 112 nm, where molecular hydrogen has a line absorption spectrum below the dissociation threshold ($H_2 \rightarrow H(1s) + H(2s)$). The absorption spectrum is governed by broad and sharp resonances also beyond the ionization threshold at 80.3 nm [31], from which point on photoionization ($H_2 \rightarrow H_2^+ + e^-$) adds to the photoabsorption cross-section (see Fig. 1.1). After a peak in absorption cross-section relatively close to the ionization threshold, the absorbance rapidly decreases with decreasing wavelength facilitating a significant transmission of EUV light through the buffer gas at the relevant gas column densities. Absorption of light, generated from the LPP, by the H_2 buffer gas may lead to secondary plasma that could influence the quality of the optical components [32]. Another important aspect to consider is the sensitivity of the photoresist itself. Typical photoresists at the wafer level are based on organic molecules that are intrinsically sensitive for longer wavelengths up to 300 nm [33].

After having discussed the spectral response of the Mo/Si mirrors as well as the

physical processes in the presented wavelength regime of Fig. 1.1, we next combine these aspects to better understand how the various wavelength regimes may affect the lithographic process. Between approximately 14 and 112 nm light is not transmitted to the wafer level because the light is either absorbed by the MLM or H_2 buffer gas and this light will not negatively impact the exposure. However, secondary plasma and mirror heating have to be dealt with. The range of 112–300 nm is reflected by the Mo/Si mirrors, and is transmitted by the buffer gas – and can result in possible parasitic exposure and contrast loss (see Fig. 1.1). As a side note, given that mirror reflectivity only rises above 50% value at 130 nm, the range relevant for exposure is typically given as 130–300 nm. For all the reasons outlined above, the study of the out-of-band wavelength regime of the emission from tin LPP is of particular importance.

1.3 Spatial characterization of tin laser-produced plasma

Besides the spectral characteristics of the LPP, its spatial character also influences the photolithography process. Every ML mirror is designed and fabricated to operate in a spectral and angular bandwidth, implying that it can accept and focus but a specific source size at any given wavelength. In case the source size is bigger than what can be accepted by the ML mirror, only a part of the source can be collected and reflected by the ML mirror – only part of generated light can be used for lithography. The non-collected part of the radiated energy will end up as energy loss, reducing efficiency. Efforts related to the ever-continuing upscaling of EUV source power thus need to include critically assessing any possible related increase in source size. Using an imaging tool, an estimate of the size of the source can be made, and thus a conclusion about this energy loss can be drawn [34]. The fact that not all emitted light is collected, may be beneficial for reducing the contribution of the out-of-band wavelengths, as these may originate from different spatial positions in the plasma. To assess the level of such reduction, the source size needs to be understood as a function of wavelength.

Imaging of plasma emission may also shed light on the critical plasma dynamics and in this way generate insights for future optimization of EUV sources. Two representative LPP examples, a droplet and a thin sheet, are shown in Fig. 1.2 where an ML mirror was used to image in-band, 13.5 nm wavelength radiation. In both cases, the laser is launched from the right side of the image, and the plasma is imaged orthogonally to the laser light propagation direction. In Fig. 1.2(a) we observe the EUV light emitted from plasma generated from a spherical tin droplet. Here, the in-band EUV emission follows an arc shape following the droplet's curvature, with the highest intensity at the center. In Fig. 1.2(b), plasma is observed from a thin sheet

formed by a prior pre-pulse. In this case, the emission is more diffuse and extends into a larger volume in space. These two plasmas may be scaled to produce the same EUV-IB energy but will have very different imaging responses when used in a photolithography system because of the different emitting volumes. Without the available imaging data, such conclusions could not have been drawn.

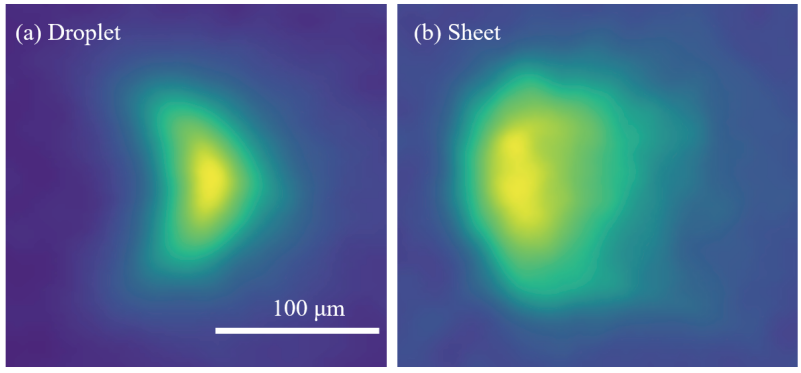

Figure 1.2: EUV plasma imaging using an MLM. (a) Plasma from a spherical droplet, (b) plasma from a thin sheet. Laser impacts from the right.

A disadvantage of imaging the plasma source using a ML mirror is that it can only image within a narrow wavelength band. Plasma images can also be taken using pinhole imaging [35, 36, 37], in conjunction with the use of transmission filters, to provide information on a particular wavelength band. However, the spatial resolution of pinhole imaging is usually low, being practically constrained in NA, and spectral dependency of source size will not be apparent. Another method of plasma imaging is by using Fresnel zone plates [38, 39, 40]. Zone plates can be fabricated very precisely with nanofabrication methods and can operate over a large wavelength range, from the soft x-ray to the infrared. However, zone plates are highly chromatic and can image only one specific wavelength depending on their zone widths. It is possible to cover a broad wavelength range by designing several zone plates having different zone widths according to the desired wavelengths. As outlined in the Thesis, the combination of a spectrometer with zone plates of varying zone widths, matching the spectrometer dispersion, allows for spectral and one-dimensional spatial imaging of plasma in a broad wavelength range with high spectral resolution.

1.4 Thesis outline and summary

In this Thesis, we experimentally study the emission from both a 1- and 2-µm-wavelength-laser-driven tin microdroplet plasma over a wide, 5–265 nm wavelength

range. Part of the experiments described in this Thesis has been conducted in the laboratory of the EUV Plasma Processes group of the Advanced Research Center for Nanolithography (ARCNL) in Amsterdam, The Netherlands. The presented electron beam ion trap (EBIT) measurements have been performed at the Max Planck Institute for Nuclear Physics in Heidelberg, Germany. The measurement tool used for both the spectroscopy and imaging experiments was developed in collaboration with the Industrial Focus Group XUV Optics at the University of Twente in Enschede, The Netherlands.

In **Chapter 2**, tin emission spectra are measured from an electron-beam ion trap and laser-produced plasma in the EUV regime. The emission line features of the EBIT data in the 12.6–20.8 nm wavelength regime are studied and assigned to specific charge states using the Cowan code. The ions observed in this range are Sn^{5+}–Sn^{10+}. The advantage of using the EBIT data for such purposes is the fact that the EBIT allows charge-state-resolved spectroscopy whereas the emission from the plasma originates from several charge states simultaneously. Next, the knowledge obtained from the EBIT data is used to identify the features in the LPP spectra. In this chapter, LPP spectra from both a liquid microdroplet and a planar solid target are studied. Differences in the emission and absorption spectra are attributed to the different plasma geometries. This study shows how out-of-band emission can be used to individually monitor several tin charge states that contribute to the unresolved transition array at 13.5 nm.

In **Chapter 3**, the calibrated emission spectrum of a 1-µm-wavelength-driven tin microdroplet LPP in the 5.5–265.5 nm range is presented. The spectrum presented is free of any higher diffraction orders due to carefully calibrated transmission filters that are used in tandem with the in-use custom-built transmission grating spectrometer. Such a spectrum can offer information for the minimization of the unwanted wavelength bands, over many orders of magnitude in emission intensity, and provide input for optimizing current and future sources of EUV light for nanolithography.

In **Chapter 4**, a fully calibrated emission spectrum in the 6.5–264.5 nm range from a tin microdroplet plasma produced using a 2-µm-wavelength drive laser is presented using the setup and method as in the previous Chapter. Emission spectra from LPPs generated by various drive laser pulse energies are shown, and are compared to 1-µm one. The emitted energy is calculated in different wavelength regimes relevant for the lithographic process. Finally, emission line features in the $\sim$15–37 nm wavelength regime are identified using Cowan and FAC atomic codes. This study presents the advantages and disadvantages of the 2- vs the 1-µm-wavelength drive laser and shows evidence for increasing plasma size with increasing wavelength.

In **Chapter 5**, a novel imaging spectrometer is presented that allows simultaneously performing spectroscopy and one-dimensional imaging. For the imaging part, zone plates with varying zone widths which match the grating dispersion, have been designed and fabricated. Experimental results of the imaging of a tin LPP are shown in the 5–75 nm wavelength regime. The imaging performance is compared to numerical wave propagation simulations. The imaging data support the evidence of the previous Chapter – of an increasing source size with increasing emission wavelength.

In the **Conclusions** we summarize the key learnings and present an outlook for future measurements employing the newly developed imaging spectrometer, and offer suggestions for improvement of the experimental apparatus.

Chapter 2

EUV spectroscopy of Sn^{5+}–Sn^{10+} ions in an electron-beam ion trap and laser-produced plasmas

Z. Bouza[1], J. Scheers, A. Ryabtsev, R. Schupp, L. Behnke, C. Shah, J. Sheil, M. Bayraktar, J. R. Crespo López-Urrutia, W. Ubachs, R. Hoekstra, and O. O. Versolato, J. Phys. B **53**, 195001 (2020)

Abstract

Emission spectra from multiply-charged Sn^{5+}–Sn^{10+} ions are recorded from an electron-beam ion trap (EBIT) and from laser-produced plasma (LPP) in the extreme ultraviolet range relevant for nanolithographic applications. Features in the wavelength regime between 12.6 and 20.8 nm are studied. Using the Cowan code, emission line features of the charge-state-resolved Sn ion spectra obtained from the EBIT are identified. Emission features from tin LPP either from a liquid microdroplet or planar solid target are subsequently identified and assigned to specific charge states using the EBIT data. For the planar solid tin target, the $4d$–$5p$ transitions of Sn^{8+}–Sn^{10+} ions are shown to dominate the long-wavelength part of the measured spectrum and transitions of type $4d$–$4f$ + $4p$–$4d$ are visible in absorption. For the droplet target case, a clear increase in the charge-state distribution with increasing laser intensity is observed. This qualitatively demonstrates the potential of using long-wavelength out-of-band emission features to probe the charge states contributing to the strong unresolved transition array at 13.5 nm relevant for nanolithography.

[1]The authors Z. Bouza and J. Scheers contributed equally to this work

2.1 Introduction

Highly charged Sn ions in laser-driven transient and dense plasmas are the emitters of extreme ultraviolet (EUV) light near 13.5 nm that is used in nanolithographic applications [10, 9, 41, 4]. In such applications, hot plasma is produced when molten Sn microdroplets are illuminated by energetic laser pulses. The responsible ions for emitting EUV photons near 13.5 nm are Sn^{8+}–Sn^{14+} with their resonance transitions $4p^6 4d^m$–$4p^5 4d^{m+1}$ and $4d^m$–$4d^{m-1}4f$ (m = 6–0) [22, 41, 4]. Spectroscopic investigation of these plasmas is challenging due to the many, densely-packed transitions in these open-$4d$-subshell Sn ions. Furthermore, spectral lines belonging to adjacent ionic charge states may blend in wavelength. Charge-state–resolved measurements would facilitate line identifications in these complex systems. Such measurements can, e.g., be obtained from single-charge-state beam experiments of which the charge-exchange spectroscopy (CXS) of tin ions by Ohashi *et al.* [24] is a notable example. Charge-state-resolved tin spectra can also be obtained from an electron-beam ion trap (EBIT), using, e.g., matrix inversion techniques to deconvolve the mixed-charge-state EBIT spectra [42].

In EUV nanolithography machines, molybdenum-silicon multi-layer mirrors are used as projection optics. These optics are characterized by a 2% reflectivity bandwidth centered at 13.5 nm wavelength [43, 44]. The EUV radiation generated from the Sn laser-produced plasma (LPP) overlaps with the peak reflectivity of these mirrors. Most of the detailed spectroscopic studies in the literature focus on emission near 13.5 nm [45, 20, 19, 41, 46, 21, 47, 48, 23, 42, 49]. However the majority of the EUV emission occurs out-of-band, i.e., outside of the 2% reflectivity bandwidth [4]. From the application perspective, this out-of-band radiation reduces the efficiency of converting drive laser light into useful EUV photons. Moreover, such radiation can influence the optics lifetime or introduce unwanted thermal loads in the scanner [50, 51]. It is thus of particular interest and importance to quantify tin spectra over the full spectral band. Recent studies have shed light on the short-wavelength side of the out-of-band emission from LPP in the 7–12 nm range [52], complementing earlier work [46]. These insights regarding short-wavelength EUV radiation were subsequently used to obtain the relative contributions of charge states Sn^{9+}–Sn^{15+} to the main unresolved emission feature at 13.5 nm, and to successfully diagnose the plasma [53], obtaining, for instance, the temperature of an industrial EUV light source.

In this work, emission features of the multiply-charged Sn^{5+}–Sn^{10+} ions in the long-wavelength, 12.6–20.8 nm region are studied. Spectra are obtained from an EBIT and from LPP. Understanding the emission features enables quantifying the contributions in LPP from the lower charge states that could not be assessed from the pre-

vious short-wavelength studies [52, 53]. First, following the procedure outlined in Ref. [42], mixed-charge-state EBIT spectra are deconvolved to obtain single-charge-state spectra. Next, the line features from Sn^{5+}–Sn^{10+} ions are assigned using the semi-empirical Cowan code [54, 55], which allows for adjusting scaling factors in the calculation in order to fit observed spectra using initial preliminary assignments. These identifications are compared to literature where available. Finally, spectral features in the emission from Sn LPP, generated from liquid droplets as well as from planar solid tin targets over a wide range of laser intensities (and thus, plasma temperatures), are identified using the EBIT spectra. These investigations extend the set of diagnostic tools for monitoring EUV-producing tin LPP in an industrial setting.

2.2 Experiment

Two types of experiments are introduced in the following. First, the experimental setup used to record emission spectra of trapped Sn ions at the FLASH-EBIT facility [56] at the Max Planck Institute for Nuclear Physics in Heidelberg, Germany, is discussed. Second, experiments on laser-produced tin plasma that are carried out at the Advanced Research Center for Nanolithography (ARCNL) in Amsterdam, The Netherlands, are presented.

2.2.1 Electron beam ion trap (EBIT)

Spectroscopic measurements of Sn ions in the EUV regime have been performed using the FLASH-EBIT facility [56]. In an EBIT, an electron beam is used to trap, ionize, and excite ions for spectroscopic measurements. It enables the investigation of a wide range of Sn ion charge states. The FLASH-EBIT can deliver an electron beam with well-defined kinetic energies. A 6 T magnetic field is applied to guide and compress the electron beam down to a diameter of about 50 µm at the center of the trap. This magnetic field is generated by a pair of superconducting Helmholtz-coils. A molecular beam of tera-i-propyltin ($C_{12}H_{18}Sn$) is injected into the trap center region. Molecules are dissociated while crossing the electron beam. The electron beam rapidly excites, ionizes, and traps the Sn ions up to the desired charge state, while the lighter elements overcome the trapping potential and leave the EBIT. Trapping of a specific charge state can be achieved by adjusting the acceleration potentials that define the kinetic energy of the electron beam.

Radiation by the Sn ions is dispersed by a 1 200-lines/mm flat-field, grazing-incidence grating with a variable line spacing [57] and is recorded on a Peltier-cooled charge-coupled device (CCD) camera. Background frames are recorded for the same exposure time as in the measurements with Sn present in the trap, and these images were

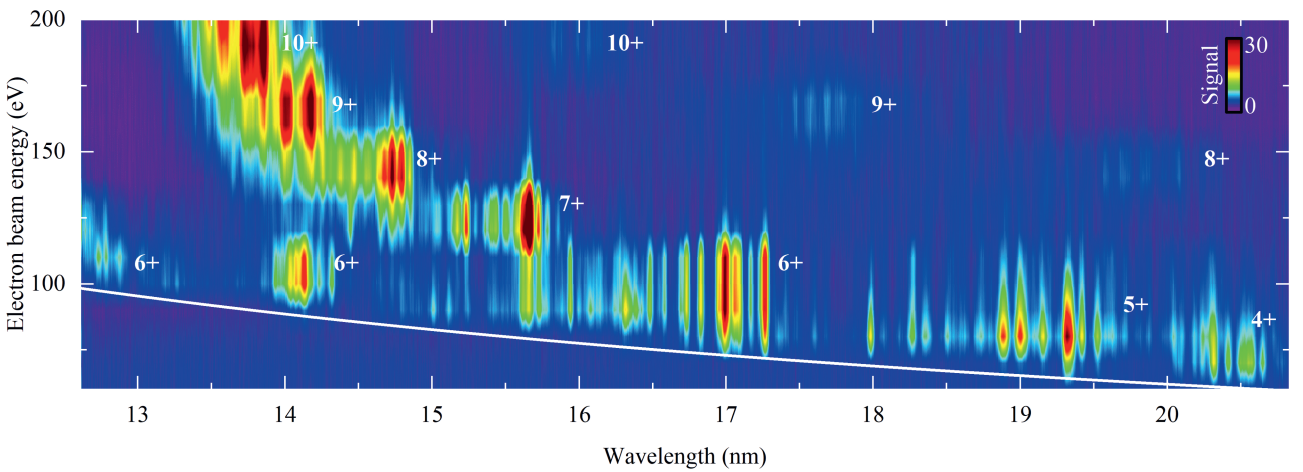

Figure 2.1: Two-dimensional spectral intensity map of Sn^{4+}–Sn^{10+} emission constructed from EBIT measurements (1.5 mA series). The map is produced by interpolating along the electron-beam energy between discrete spectra which are taken at 10-eV steps. The color bar indicates the signal or the emission intensity. The white line indicates where the electron-beam energy equals the photon energy (see main text). Charge-state-specific emission islands are labeled by the charge state of the emitting Sn ion.

then subtracted from the recorded plasma emission to eliminate the dark counts as well as read-out counts. The resulting CCD images are cropped and corrected for spectrometer aberrations. Subsequently, the images are integrated along the non-dispersive axis. The resulting spectra are then corrected for diffraction efficiency, as well as the quantum efficiency of the camera following Ref. [58] (also see, e.g., Ref. [59]). The wavelength calibration of the spectrometer is performed by injecting oxygen into the trap, using well-known O^{2+}–O^{4+} lines in the EUV range [60]. A wavelength range spanning 12.6–20.8 nm is captured with a resolution of about 0.03 nm at full width at half maximum (FWHM). A more detailed description of the EBIT experiments is given in Refs. [61, 26, 42].

Two measurement series are conducted. In the first series, the electron-beam energy is increased from 60 to 200 eV in steps of 10 eV. The electron-beam current is set to a constant 1.5 mA. Sn charge states 4+ to 10+ are observed using these EBIT settings. A two-dimensional map (wavelength, electron-beam energy), composed by interpolating between discrete EBIT spectra, is presented in Fig. 2.1. In the second series, the electron-beam energy is increased from 180 to 610 eV in steps of 5 eV, and the electron-beam current is set to a constant 13 mA. The Sn charge states that can be observed in this series range from 8+ to 20+.

2.2.2 Laser-produced plasma (LPP)

Two different experimental setups are used to produce Sn plasmas with a laser: (i) a droplet tin target and (ii) a planar solid tin target. Both experimental setups are detailed below. The targets are irradiated by a Nd:YAG laser operating at a wavelength of 1064 nm, with a Gaussian pulse length of 10 ns FWHM.

In both setups, spectral emission from the Sn-produced plasma is measured under an angle of 60° with respect to the propagation direction of the laser light, using a broadband transmission grating spectrometer [62, 63]. The spectrometer is operated with an entrance slit width of 25 µm and a 10 000 lines/mm transmission grating achieving a FWHM instrument resolution of 0.1 nm at 13 nm [62, 15]. The recorded wavelength regime is 5–25 nm. The diffracted light is recorded on a back-illuminated CCD from Greateyes (GE2048 512BI UV1), cooled to -30°C to reduce thermal noise. Background frames are recorded for the same exposure time as in the measurements with Sn plasma present, and these images were then subtracted from the recorded plasma emission to eliminate the dark counts as well as read-out noise. The exposure time is varied from 1–5 s to collect sufficient signal-to-noise ratio. The resulting CCD images are cropped and corrected for shear and tilt introduced by a slight misalignment of the slit and grating with respect to the CCD pixel array. Subsequently, the images are integrated along the non-dispersive axis. The resulting spectra are then

corrected for first- and second-order diffraction efficiency, as well as the quantum efficiency of the camera.

The dispersion of the grating is obtained by observing well-documented Al^{3+} and Al^{4+} lines [60] from a laser-produced Al plasma [15]. Based on the position of the zeroth diffraction order, and known tin lines, an accurate wavelength calibration is obtained.

Droplet tin target

Molten Sn microdroplets of 99.995% purity with a diameter of 18 µm are dispensed from a droplet generator inside a vacuum vessel of 5×10^{-7} mbar pressure. The droplets travel at a speed of approximately 10 m/s in the vacuum vessel and pass through a horizontal light sheet produced by a He-Ne laser. The light scattered by the droplets is detected using a photomultiplier tube which subsequently triggers the Nd:YAG laser system. The droplets are irradiated by a laser pulse with an 80 µm (FWHM) Gaussian spot size. Additional details regarding the droplet-based experimental setup can be found in Ref. [11].

Planar solid tin target

A 1 mm thick Sn planar solid polycrystalline target of 99.995% purity is mounted onto a 2D-translation stage in a vacuum vessel which is kept at a pressure of 10^{-6} mbar. The solid target is irradiated by the same Nd:YAG laser system as is used for the droplet targets. The FWHM spot size at the planar target surface is 130 µm. Only two consecutive pulses are recorded on the same spot of the Sn target to prevent any influence of target deformation on the recorded spectra. The translation stage enables a stepwise motion of the target to guarantee a fresh target spot after each series of two pulses. Additional details regarding the planar solid-based experimental setup can be found in Ref. [64].

		Average wavelength (nm)		
Ion	Transition	CXS [24]	COWAN	Width (nm)
Sn^{5+}	$4d$–$4f$	19.0	19.4	0.6
	$4p$–$4d$	–	18.0	0.1
Sn^{6+}	$4d$–$4f$	16.0	17.1	0.5
	$4p$–$4d$	–	15.9	1.2
	$4d$–$5f$	–	14.2	0.4
	$4d$–$6f$	–	13.0	0.3
Sn^{7+}	$4d$–$4f$	15.6	15.8	0.7
	$4p$–$4d$	–	15.1	0.6
	$4d$–$5f$	12.5	12.6	0.3
Sn^{8+}	$4d$–$4f$	14.2	15.0	0.7
	$4p$–$4d$	–	14.3	0.7
	$4d$–$5p$	19.5	19.8	0.6
Sn^{9+}	$4d$–$4f$	14.0	14.4	0.7
	$4p$–$4d$	–	13.9	0.6
	$4d$–$5p$	17.7	17.7	0.5
Sn^{10+}	$4d$–$4f$	13.8	13.9	0.4
	$4p$–$4d$	–	13.6	0.5
	$4d$–$5p$	16.0	16.0	0.5

Table 2: Average wavelength of various transition arrays in Sn^{q+} (q = 5–10), see also Fig. 2.4. Results obtained from the Cowan code are presented as gA-weighted average wavelength of the transition array (first moment of the distribution according to UTA formalism [65, 66]), and the width represents the standard deviation of the distribution (square root of the variance). CXS results (center of the distribution of emission lines) are obtained from collisions of $Sn^{(q+1)+}$ with Xe, reproduced from Ref. [24]. We note that the Table entries from Ref. [24] may refer to the average position of the $4d$–$4f$ and $4p$–$4d$ transitions arrays combined.

2.3 Measurements

In the following, we first discuss the results of the EBIT measurements. Spectra from individual charge states are presented (see Fig. 2.2), as obtained from EBIT measurements by using the matrix inversion introduced in Ref. [42]. Identifications of the observed line features are made using the Cowan code (Figs. 2.2 and 2.3). An overview of the wavelength positions of relevant configurations is presented in Fig. 2.4 as well as in Table 2. Next, the EBIT data is employed to qualitatively study the contribution of individual charge states to the emission from laser-produced plasmas created from both droplet or planar solid tin targets (see Fig. 2.5).

2.3.1 EBIT spectra

In Fig. 2.1, a two-dimensional (wavelength, electron-beam energy) spectral intensity colormap of Sn ions constructed from EBIT measurements is presented (1.5-mA series). Emission features from Sn^{4+} to Sn^{10+} ions can be observed. The white line indicates the threshold at which the photon energy equals the electron-beam energy, above which a particular transition can energetically be excited directly by single-electron impact.

The individual EBIT spectra contain a mixture of charge states, dependent on EBIT conditions such as electron-beam energy and current. Following the procedure outlined in Ref. [42], spectra of the individual charge states are obtained using a matrix inversion method. This method enables unraveling blended spectra by assuming that every spectrum contains a linear combination of contributions from individual charge states. The contributions from these charge states are weighted by their respective fluorescence curve (a curve defined as the emission intensity of the various spectral lines as function of the electron-beam energy). Following the work of Scheers *et al.* [42], to obtain fluorescence curves, we project vertical regions of interest from the data as shown in Fig. 2.1. Several lines per charge states are used to construct a generic fluorescence curve. Chosen lines are preferably isolated, mostly outside of dense spectral regions. The observed energy dependencies of the line strengths are typically very similar for all lines associated with a particular charge state. Individual fluorescence curves are normalized and subsequently averaged such that a generic fluorescence curve per charge is constructed. A matrix inversion technique is subsequently invoked. In it, the colormaps are represented by a matrix E. The matrix elements of $\boldsymbol{E}$ contain spectral intensities directly obtained from measurements. Fluorescence curves span a fluorescence matrix $\boldsymbol{F}$ in $\boldsymbol{FS} = \boldsymbol{E}$, where $\boldsymbol{S}$ contains the individual, charge-state-resolved spectra. The solution of matrix $\boldsymbol{S}$ is given by $\boldsymbol{S} = (\boldsymbol{F}^T\boldsymbol{F})^{-1}\boldsymbol{F}^T\boldsymbol{E}$.

The charge-state-resolved spectra obtained from both the lower- and higher-current measurement series are nearly identical. An improved signal-to-noise ratio is obtained in the higher-current case. A consequence of using a different electron-beam current might be variations in level population within the respective tin ions and therefore line intensities may change [67], but such an effect was not observed in our spectra. Because of the higher signal-to-noise ratio, the higher-current series is used in the following for the spectra of Sn^{8+}–Sn^{10+}. The lower-current series is used for Sn^{5+}–Sn^{7+} as these ions could not be observed in the higher-current series. Sn^{4+} is not included because its dominant line features largely fall outside the spectrometer range [68, 24].

In the following, the spectral fingerprints of the EBIT spectra from individual charge states are discussed. For convenience, the transitions of type of $4d^m$–$4d^{m-1}4f$, $4p^64d^m$–$4p^54d^{m+1}$, $4d^m$–$4d^{m-1}5f$, $4d^m$–$4d^{m-1}6p$, $4d^m$–$4d^{m-1}6f$ and $4d^m$–$4d^{m-1}5p$, where m = 9–4 in the case of Sn^{5+} to Sn^{10+}, will be written as $4d$–$4f$, $4p$–$4d$, $4d$–$5f$, $4d$–$6p$, $4d$–$6f$ and $4d$–$5p$, respectively.

The Hartree-Fock method with relativistic corrections incorporated in the RCN-RCN2-RCG chain of the Cowan code [54, 55] is used for the calculation of energy levels, transition wavelengths, and gA values (multiplicity g times the Einstein coefficient A). Spectral line intensities recorded from an EBIT may deviate from calculated gA values (see, e.g., Ref. [67]) as excited-state populations, which together with these gA values determine the line intensities, depend on the specifics of electron impact excitation. Inclusion of such effects in our calculations would require detailed collisional-radiative modeling [69] which is beyond the scope of the current paper. In this work, we find that emission features can here be reliably identified using gA values.

Spectrum of Sn^{5+}

Strong emission line features of Sn^{5+} are observed between 18–20 nm in the EBIT spectrum (Fig. 2.2). These line features are related to transitions of type $4d$–$4f$ and $4d$–$6p$. They were identified in Ref. [47], where the Cowan code was used to analyze measurements performed using a spark source. A comparison between our spectrum with gA factors calculated by Cowan code using scaling parameters based on the line identifications from Ref. [47], convoluted with the spectrometer resolution (0.03 nm FWHM), is presented in Fig. 2.2. Calculations and experiment are in good agreement. Further, we observe a strong and isolated line at 17.98 nm wavelength. Cowan code calculations indicate that this feature can be identified as the $4p^6\ 4d^9\ {}^2D_{5/2}$–$4p^5\ 4d^{10}\ {}^2P_{3/2}$ transition.

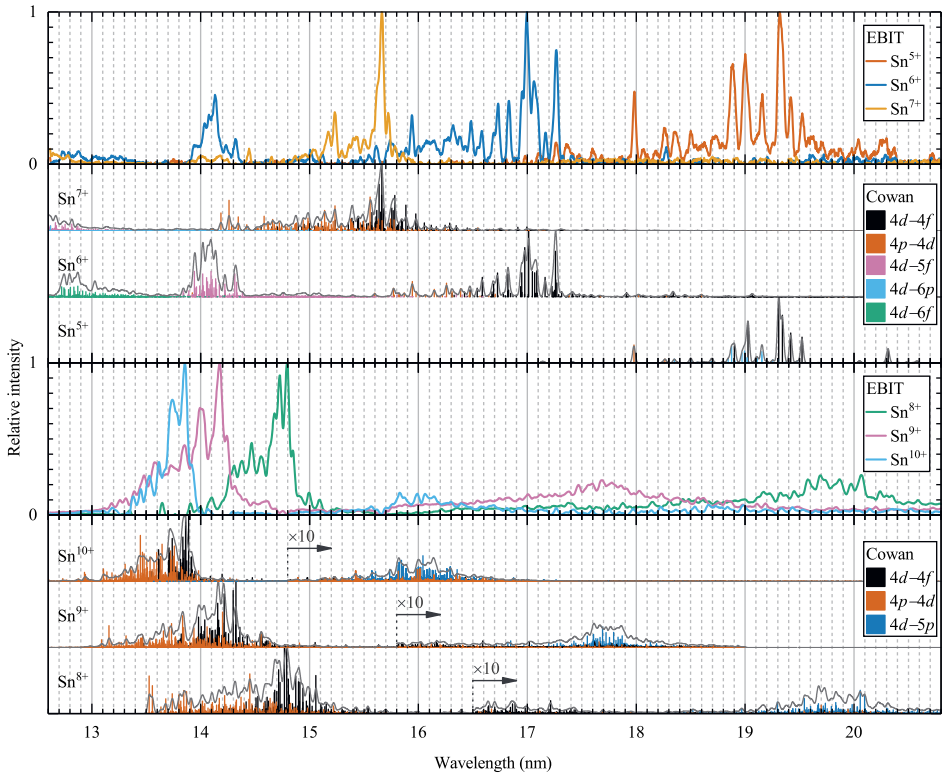

Figure 2.2: Normalized charge-state-resolved spectra from Sn^{5+}–Sn^{10+} ions obtained from the EBIT measurements using the matrix inversion method (see main text). The results for Sn^{5+}–Sn^{7+} originate from the 1.5 mA electron beam current measurements, and the Sn^{8+}–Sn^{10+} results derive from the 13 mA current measurements (see main text). Results from Cowan code calculations are presented with gA factors normalized to maximum gA value for the corresponding charge state (shown as sticks in the plot). The envelopes (shown in gray) represent a convolution of the gA factors with a Gaussian function accounting for the spectrometer resolution (0.03 nm FWHM). These envelopes are separately normalized to a maximum value of one at their respective maximum.

Spectrum of Sn^{6+}

In the case of Sn^{6+}, prominent emission line features can be observed in Fig. 2.1 in three separate wavelength regions: 12.6–13.6 nm, 14–14.5 nm, and 16–17.5 nm. For the identification of the emission line features between 12.6–14.5 nm, we use the Cowan atomic structure code. The level energies of the $4d^7 5f$ and $4d^7 6f$ configurations of Sn^{6+} are optimized using configuration-interaction between the following

configurations: $4p^6(4d^8 + 4d^7 5s + 4d^6 5s^2)$ in the even set and $4p^6 4d^7(5p + 6p + nf$ (n = 4–7)) $+4p^5(4d^9 + 4d^8 5s)$ in the odd set. The fitting of the levels of the $4p^6 4d^8$, $4p^6 4d^7(5p+4f)$ and $4p^5 4d^9$ configurations was performed using known data [48, 70]. The electrostatic energy parameters of the unknown configurations $4d^7 6p$, $4d^7 7f$ and $4p^5 4d^8 5s$ were scaled by a rather standard factor 0.85 with respect to their *ab initio* Hartree-Fock with relativistic corrections (HFR) values. The interaction integrals were scaled by 0.8. The *ab initio* HFR values for the $4d^7 5f$ and $4d^7 6f$ configurations were improved using the same scaling factors and effective parameters as were obtained previously for $4d^7 4f$. The final fitted and adopted energy parameters as well as scaling factors for configurations $4d^7 nf$ (n = 4–6) and $4p^5 4d^9$ responsible for most of the features in our EBIT spectrum, including those in the 16–17.5 nm region, are presented in Table 2.2.

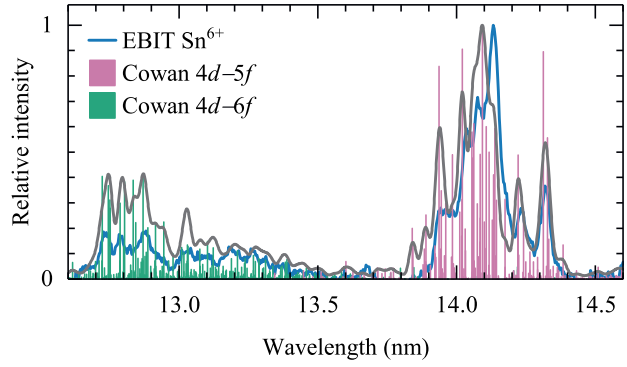

Figure 2.3: Identification of spectral features in Sn^{6+} obtained from the EBIT measurements using the matrix inversion method (see text). Vertical lines indicate calculated gA factors of $4d$–$(5f + 6f)$ transitions normalized to the strongest transition in this range. The gray envelope is a convolution of the presented gA values with a Gaussian function accounting for the spectrometer resolution of 0.03 nm (FWHM). The envelope is separately normalized for better visibility.

The results of the Cowan code calculations for both $4d$–$5f$ and $4d$–$6f$ transitions are presented in Fig. 2.3, along with the spectrum of Sn^{6+} obtained from the matrix inversion technique. The heights of the vertical lines represent the calculated gA values for individual lines within the transition arrays $4d$–$(5f + 6f)$. They are normalized to the strongest transition in the here-presented wavelength range. The gray envelope is a convolution of these gA factors with a Gaussian function representing the spectrometer resolution (0.03 nm FWHM). This envelope is separately normalized to a value of one for better visibility. The EBIT spectrum of Sn^{6+} presents a smaller relative emission amplitude, by a factor of approximately two, in the 12.6–13.2 nm

range as would be expected from a direct comparison of the calculated gA values of the $4d$–$5f$ to the $4d$–$6f$ transitions. This relatively small amplitude may in part be explained by the fact that the electron-beam energy is barely sufficient to excite to the levels giving rise to the $4d$–$6f$ transitions. Collisional-radiative modeling, left for future work, would enable assessing the dependence of the observed line strengths on electron-beam energy and its density. In general, our calculations, including those for the $4d$–$4f$ and $4p$–$4d$ transitions, are in good agreement with the spectra (see Fig. 2.2).

Spectrum of Sn^{7+}

Emission line features of Sn^{7+} lie between 15–16 nm, as seen from Fig. 2.2. These line features correspond to the $4d$–$4f$, $4p$–$4d$ transitions identified by Churilov and Ryabtsev [19] employing a vacuum spark setup. Fig. 2.2 also shows transition probabilities for the Sn^{7+} ion spectrum calculated with the Cowan code using scaling parameters from Ref. [19]. A convolution of these transitions with Gaussian function accounting for the spectrometer resolution is in agreement with the experimental spectrum. The $4d$–$6p$ transitions are not visible in our EBIT spectra. However, we note that our calculations of the $4d$–$6p$ transitions are in excellent agreement with unidentified spectral features around 14 nm observed in charge-exchange spectroscopy, whereby spectra resulting from collisions of Sn^{8+} with He and Xe were observed [24]. The small feature at the edge of our detection region (near 12.8 nm) may be tentatively associated with the $4d$–$5f$ transition array as was previously noted in Ref. [46].

Spectrum of Sn^{8+}

Strong emission features of Sn^{8+} are found between 14 and 15 nm, as shown in Fig. 2.2. Identified lines stem from $4p$–$4d$ and $4d$–$4f$ transitions [20]. Although more recent studies [26] have found that the level energies of the ground manifold from Ref. [20] in Sn^{8+}–Sn^{10+} may not be fully correct, the accuracy of the line determination in the EUV is sufficient for the current investigations. Configurations used in those [20] and the current Cowan calculations for the charge states Sn^{8+}–Sn^{10+} are of type $4d^{m-1}(5p+6p)+4d^{m-1}(4f+5f+6f)+4p^5(4d^{m+1}+4d^m5s)$. Scaling factors were estimated by extrapolation from Sn^{6+}, Sn^{7+}, and isoelectronic Ag ion spectra [71]. The results, shown in Fig. 2.2, are in agreement with our measurements. Emission features located near 20 nm belong to the $4d$–$5p$ transition array in Sn^{8+}–Sn^{10+} ions, as previously identified by Ohashi and coworkers [24] in their CXS work. No individual line assignments were made in that work. There are thousands of lines contributing to these features, thus making line identifications of specific transitions

inaccessible, which is also true in the current work. However, the origin of the emission features can be well understood from Cowan code calculations.

Spectrum of Sn^{9+}

The $4p$–$4d$ and $4p$–$4f$ transitions of Sn^{9+} are located around 14 nm, as shown in Fig. 2.2, and line identifications are described in Ref. [20]. A comparison of the spectrum, as obtained by the matrix inversion technique, with the listed transitions of Ref. [20] show that the strongest peak at 14.17 nm cannot be satisfactorily explained. However, using instead Cowan calculations based on an extrapolation of scaling factors, similar to the case of Sn^{8+} (see above), enables obtaining a reasonable match with the experimental spectrum (see Fig. 2.2) including the $4d$–$5p$ transitions located between 16 and 19 nm.

Spectrum of Sn^{10+}

The $4p$–$4d$ and $4d$–$4f$ transitions in Sn^{10+} are found between 13 and 14 nm (Fig. 2.2) according to line identifications performed on this transition array in Ref. [20]. Transitions of the type $4d$–$5p$ are observed between 15 and 17 nm. The Cowan calculations (for details, see above) for the aforementioned transition arrays are in excellent agreement with the experimental data, as shown in Fig. 2.2.

Summary of EBIT spectra

Fig. 2.4 summarizes our findings of the emission characteristics of the $4d$–$4f$, $4p$–$4d$, $4d$–$5f$, $4d$–$6f$, and $4d$–$5p$ transitions of the charge states Sn^{5+}–Sn^{10+}. We note that the positions found for the $4d$–$4f$ and $4p$–$4d$, smoothly scaling with charge state, are in accordance with literature values. These configurations become more and more intertwined with increasing charge state. We note that the $4d$–$5p$ transitions in Sn^{8+}–Sn^{10+} may be easily confused with $4d$–$4f$ or $4p$–$4d$ transitions of the lower charge states when diagnosing a tin plasma.

2.3.2 Diagnosing LPP spectra

Fig. 2.5 presents EUV emission spectra for various laser intensities from laser-produced plasmas using two target geometries: droplet and planar-solid. Plasma is produced from a Sn droplet target (top panel) and from a planar solid target (middle panel). Charge-state-resolved EBIT spectra of Sn^{5+}–Sn^{10+} ions are shown also (bottom panel).

In the top panel of Fig. 2.5, emission spectra from illumination of a Sn droplet target using laser intensities of 0.2, 0.6, 0.8, and $2.6 \times 10^{11}\,\mathrm{W\,cm^{-2}}$ are presented. The

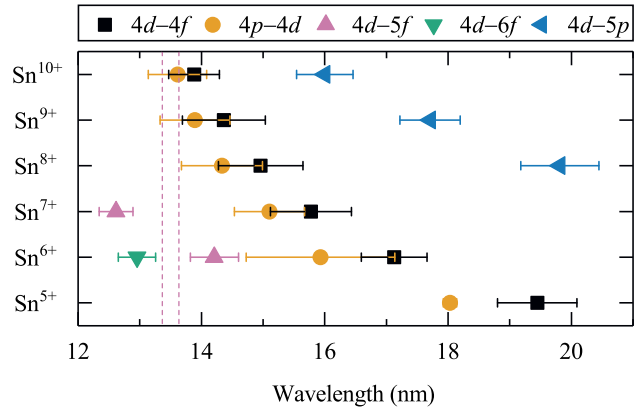

Figure 2.4: Wavelengths of spectral features of various transition arrays in Sn^{q+} (q = 5–10) as obtained from our Cowan code calculations. Symbol location represents the gA-weighted average wavelength of the transition array (first moment of the distribution according to UTA formalism [65, 66]), while the indicated width represents the standard deviation of the distribution (square root of the variance). Dashed vertical lines indicate a 2% bandwidth around 13.5 nm. Wavelengths and distribution widths shown in this figure are presented in Table 2.

laser intensity was calculated as described in Ref. [15]. The dependence of the main feature near 13.5 nm wavelength on laser intensity has been discussed in detail elsewhere (see, e.g., Ref. [15, 14]) and the current discussion focuses on the wavelengths above 13.5 nm. For the lowest laser intensity, line features associated with the $4d$–$4f$ transition arrays in Sn^{5+}–Sn^{7+} particularly stand out. Their visibility strongly decreases with increasing laser intensity. Instead, line features associated with $4d$–$5p$ transitions of the more highly charged Sn^{8+} and Sn^{9+} ions become more prominent in this wavelength range with increasing laser intensity. The reduction of observed intensities of lines associated with the lower charge states is most pronounced for Sn^{5+} and Sn^{6+}; lines of Sn^{7+} also reduce in relative amplitude but remain visible for all laser intensities shown. The expected evolution of the apparent charge state distribution with laser intensity is thus observed: higher laser intensity produce a hotter plasma with a higher average charge state. A more quantitative study would yield important insights regarding the population of charge states relevant for in-band emission at 13.5 nm wavelength, analogous and complementary to the work of Torretti *et al.* [53] for the shorter-wavelength emission features.

In the middle panel of Fig. 2.5, emission spectra are shown from a planar solid tin target for laser intensities of 0.3, 0.4, 0.8, and $3.0 \times 10^{11}\,\mathrm{W\,cm^{-2}}$. This series of intensities is similar to those used in the droplet target case. The spectral differences between planar solid and droplet targets for wavelengths larger than 14 nm are strik-

ing. Generally, much more emission occurs at these longer wavelengths than in to the droplet target case. No emission line features of the low charge states Sn^{5+}–Sn^{7+} stand out. Instead, for all laser intensities, the $4d$–$5p$ transitions of the more highly charged Sn^{8+}–Sn^{10+} ions dominate this part of the spectrum. These emission features slowly decrease in relative amplitude as the laser intensity increases. Noteworthy are dips in the spectra observed at wavelengths where emission peaks appear for the droplet target.

More specifically, the strong dip around 15.6 nm seems to coincide with the expected location of the $4d$–$4f$ + $4p$–$4d$ transition array of Sn^{7+}. Similarly, two other particularly visible dips, located around 14.8 nm and 14.2 nm, line up with $4d$–$4f$ + $4p$–$4d$ transitions of Sn^{8+} and Sn^{9+}, respectively. The latter dip position also overlaps with the $4d$–$5f$ transition in Sn^{6+}. These dips can thus be explained by absorption by the plasma constituents.

Briefly, the spectral differences between the two target cases can be traced to geometrical arguments. The particular initial phase (liquid vs planar solid tin) has little bearing on the ensuing plasma given the energies involved. The geometry of the target affects the plasma emission in two aspects. First, size: the small, 18 µm-diameter droplet interacts mainly with the most intense part of the 80 µm laser pulse spot. In contrast, the large solid target interacts with the full beam spot. Second, dimensionality: the plasma expands and rarefies. The dimensionality of the rarefaction can be related to that of the target: a one-dimensional, linear expansion for the planar target and a quasi-three-dimensional expansion for the small droplet [72]. The rarefaction is much more rapid in the droplet case leading to less (self-)absorption of light [15]. Thus, the absorption features of the solid target spectra may be attributed to absorption in a rather dense but colder part of the plasma[2], which contains the relevant charge states that exhibit significant opacity [49], surrounding the main, hot and dense emission zone [73, 16]. For near-infrared drive lasers such as those operating at 1-µm wavelength, a spherical target appears to be better suited for obtaining a large fraction of the emitted EUV radiation in-band.

[2]We note that Filevich *et al.* [Phys. Rev. E **67**, 056409 (2003)] likewise postulated that a cool, dense plasma, created by EUV emission from the tin LPP leads to strong absorption by low ion stages in the peripheral zone.

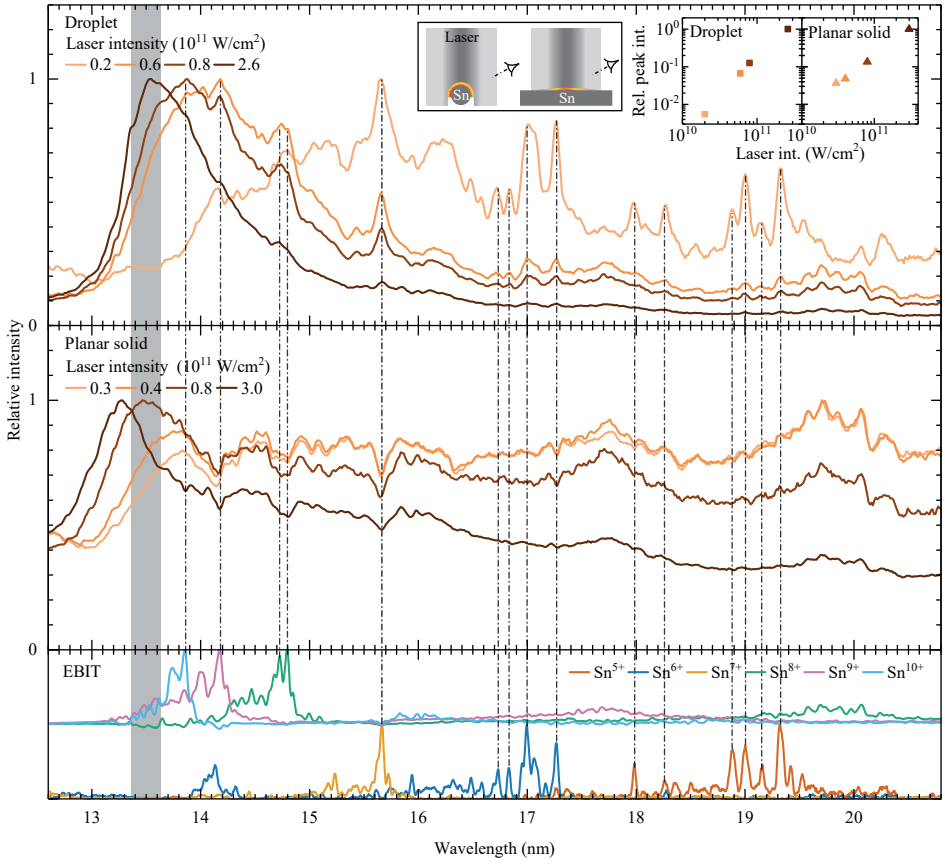

Figure 2.5: Top: normalized experimental LPP emission spectra in the extreme ultraviolet range for various Nd:YAG laser intensities, using a liquid droplet-based tin target with a droplet diameter of 18 µm and a FWHM laser beam spot of 80 µm. Middle: normalized experimental LPP emission spectra in the extreme ultraviolet region for various Nd:YAG laser intensities, using a planar solid tin target with a laser beam spot of 130 µm FWHM. Bottom: normalized charge-state-resolved spectra of Sn^{5+}–Sn^{10+} obtained from the EBIT measurements using the matrix inversion method (see text); the spectra of the three highest charge states are vertically offset for better visibility. The gray-shaded area shows the 2% bandwidth around 13.5 nm relevant for nanolithographic applications. The vertical dashed-dotted lines trace particular features from the EBIT in the LPP spectra. A schematic layout of both LPP experiments is presented as an inset in the top panel. The additional inset graph shows relative peak intensities as a function of laser intensity for both target cases.

	$4d^7 4f$			$4d^7 5f$		$4d^7 6f$	
Parameter	HFR	FIT	FIT/HFR	HFR	Adopted	HFR	Adopted
E_{average} $(4d^7 nf)$	535000	533917 (271)		694284	693283	779714	779714
$F^2(4d, 4d)$	102377	85801 (200)	0.838	103411	86649	103642	86843
$F^4(4d, 4d)$	68285	59966 (468)	0.878	69065	60650	69238	60802
$\alpha(4d)$		50[f]		50			50
$\beta(4d)$		-540[f]		-540			-540
$T^1(4d)$		-2[f]		-2			-2
$\zeta(4d)$	3681	3799[f]	1.032	3740	3861	3757	3877
$\zeta(nf)$	110	110[f]	1	52	52	28	28
$F^2(4d, nf)$	65286	54159 (1254)	0.829[r1]	22023	18257	10343	8574
$F^4(4d, nf)$	40129	33290 (771)	0.829[r1]	12342	10232	5631	4669
$G^1(4d, nf)$	75280	60314 (331)	0.801[r2]	20272	16238	8371	6705
$G^3(4d, nf)$	45662	36584 (201)	0.801[r2]	13362	10703	5781	4630
$G^5(4d, nf)$	31866	25530 (140)	0.801[r2]	9627	7711	4241	3397

	$4p^5 4d^9$		
Parameter	HFR	FIT	FIT/HFR
E_{average} $(4p^5 4d^9)$	616908	597881 (506)	0.969
$\zeta(4p)$	40711	44357 (539)	1.09
$\zeta(4d)$	3599	3714[f]	1.032
$F^2(4d, 4d)$	108221	102669 (3811)	0.949
$G^1(4p, 4d)$	137494	107607 (1666)	0.783[r3]
$G^3(4p, 4d)$	85454	66898 (1035)	0.783[r3]

Table 2.2: Cowan code Hartree-Fock with relativistic corrections (HFR) and least-squares-fitted (LSF) parameter values of the $4d^7 nf$ (n = 4–6), and $4p^5 4d^9$ configurations in Sn^{6+}. All parameters are given in units of cm^{-1}. One-standard-deviation uncertainties are given in brackets. Fixed parameters are indicated with a superscripted "f". Parameters superscripted with r1, r2, and r3 are also fixed in the fitting procedure.

2.4 Conclusion

Emission spectra from multiply-charged Sn^{5+}–Sn^{10+} ions are recorded from an EBIT and from LPP in the EUV range. In particular, features in the wavelength range between 12.6 and 20.8 nm are studied. A matrix inversion method is employed to produce charge-state-resolved spectra from the EBIT measurements. The Cowan code is used to identify the emission line features. Particular attention is given to the newly identified $4d$–$5f$ and $4d$–$6f$ transitions in Sn^{6+}. We have also identified a previously unreported $4p$–$4d$ transition in Sn^{5+}. The obtained spectroscopic information is employed to diagnose the Sn LPP produced from a liquid droplet and a planar solid Sn target. Emission features are identified and assigned to specific charge states us-

ing the EBIT data. For the planar solid Sn target, the $4d$–$5p$ transitions of Sn^{8+}–Sn^{10+} ions dominate the long-wavelength part of the EUV spectrum. Transitions of type $4d$–$4f$ + $4p$–$4d$ appear as self-absorption dips in the spectra. For the droplet target relevant for nanolithography, a more clear evolution of the charge-state distribution with laser intensity is observed: higher laser intensities produce a hotter plasma with a higher average charge state. Transitions of type $4d$–$4f$ + $4p$–$4d$ in Sn^{5+}–Sn^{7+} smoothly give way to $4d$–$5p$ type transitions in Sn^{8+}–Sn^{10+}. This study demonstrates the inherent potential of out-of-band emission to individually monitor several Sn charge states that strongly contribute to the unresolved transition array at 13.5 nm.

2.5 Acknowledgments

Part of this work has been carried out within the Advanced Research Center for Nanolithography, a public-private partnership of the University of Amsterdam, the Vrije Universiteit Amsterdam, the Netherlands Organisation for Scientific Research (NWO) and the semiconductor equipment manufacturer ASML and was financed by Toeslag voor Topconsortia voor Kennis en Innovatie from the Dutch Ministry of Economic Affairs. The transmission grating spectrometer was developed in the Industrial Focus Group XUV Optics at the University of Twente and supported by the FOM Valorisation Prize 2011 awarded to F. Bijkerk and NanoNextNL Valorization Grant awarded to M.Bayraktar in 2015. This project received funding from the European Research Council Starting Grant No. 802648 and is part of the VIDI research program with Project No. 15697, which is financed by NWO. Work by C.S. was supported by the Max-Planck-Gesellschaft and by the Deutsche Forschungsgemeinschaft Project No. 266229290. J.S. and O.O.V. thank the MPIK in Heidelberg for the hospitality during the measurement campaign.

Chapter 3

The spectrum of a 1-µm-wavelength-driven tin microdroplet laser-produced plasma source in the 5.5–265.5 nm wavelength range

Z. Bouza, J. Byers, J. Scheers, R. Schupp, Y. Mostafa, L.Behnke, Z. Mazzotta, J. Sheil, W. Ubachs, R. Hoekstra, M. Bayraktar, and O. O. Versolato, AIP Adv. **11**, 125003 (2021)

Abstract

We present a calibrated spectrum in the 5.5–265.5 nm range from a microdroplet-tin Nd:YAG-laser-produced plasma under conditions relevant for the production of extreme ultraviolet light at 13.5 nm for nanolithography. The plasma emission spectrum, obtained using a custom-built transmission-grating spectrometer, results from a careful calibration of a series of filters enabling measurements free of any higher diffraction orders. Specifically, Zr, Si and Al thin-foil filters, and bulk LiF, MgF_2 and UV fused silica filters are employed. A further filter using four SiC mirrors is used to record the otherwise inaccessible 40–100 nm range. The resulting corrected and concatenated spectra are shown to accurately match in their respective overlap regions. The possibility to measure spectra over this broad range enables the optimization of current and future sources of EUV light for nanolithography by providing the diagnostics required for minimizing the emission of unwanted wavelength bands.

3.1 Introduction

Laser-produced plasma (LPP) generated from liquid tin (Sn) microdroplets provides extreme ultraviolet (EUV) light for modern nanolithography [4, 5, 6, 7, 8, 9, 10], enabling the continued reduction of feature sizes on affordable integrated circuits (ICs). Such laser-produced plasmas of tin are characterized by a strong emission peak near 13.5 nm, originating from transitions between complex excited states in multiply charged Sn^{10+}–Sn^{15+} ions [18, 19, 20, 21, 22, 23, 24, 25, 26, 27].

Multilayer optics are used in industrial lithography machines to collect the EUV light from its source, and to provide an image of the so-called mask onto the wafer. These optics are designed to reflect wavelengths in a 2% wavelength bandwidth centered around 13.5 nm (the bandwidth limitation is in part due to the many, ~ 10 required reflective surfaces) [43, 44]. As such, most spectroscopic works on Sn LPPs have focused on the "in-band" wavelength region [41, 49, 27, 45, 46, 47], or on nearby out-of-band (OOB) EUV emission features [46, 24, 52, 53, 15, 14, 74, 75, 13], spectral regions which may help diagnose the plasma in terms of its main in-band emitters' charge states or temperature. Little spectroscopic information is available for longer, vacuum (VUV)- and deep-ultraviolet (DUV) wavelengths in particular in terms of relative (or absolute) emission intensities. Available spectra in the literature either show vacuum- or deep-ultraviolet spectra without the EUV region around 13.5 nm [76, 77, 78, 79, 80], or if the EUV region is presented, the spectral range between EUV and DUV is not shown [81, 82, 83, 84, 85, 33].

VUV/DUV emission may be transported through the multilayer optics systems and expose the wafer. Given the significant photon energy, this exposure may influence the chemical processes on the wafer and negatively impact imaging contrast and quality [50, 51]. As such, it is of significant interest to understand in detail the spectrum of EUV generating LPPs in terms of their absolute emission intensity. This will enable identifying the origins of many yet-unknown emission features and enable the development of mitigation strategies, i.e. minimize the OOB emission. In particular, the wavelength range of 30–90 nm is important for EUV lithography due to the strong absorption by hydrogen which is present as a buffer gas in the EUV source chambers. Photoionization of hydrogen molecules by DUV radiation generates plasmas in the scanner which can degrade important optical components [32]. It is challenging to obtain the source spectrum in this wavelength range due to strong contributions from higher diffraction orders of the very strong emission feature centered around 13.5 nm.

We present an intensity-calibrated spectrum of a droplet-based tin plasma driven by 1-µm laser light in the wavelength range between 5.5–265.5 nm. A custom-built

transmission grating spectrometer (TGS) is used to record the spectrum using a 1000 lines per mm grating. Higher diffraction orders, which would otherwise render impossible the detection of longer wavelengths, are eliminated by using Zr, Si, Al, LiF, MgF_2, and UV fused silica (UVFS) filters. An additional novel filter using four SiC mirrors is used to record the 40–100 nm region which would, given the dominant contribution from the higher diffraction orders of the EUV band if unfiltered, otherwise remain inaccessible. Careful calibration of these filters and the transmission grating combined with the response of the camera enables the absolute calibration of the full operating band and to obtain a spectrum free of any higher diffraction orders.

3.2 Experimental setup

In our experiments, molten tin microdroplets of 46 µm diameter are first irradiated by a relatively low intensity ($\sim 10^9$ W/cm^2), 1-µm wavelength pre-pulse (PP) from an Nd:YAG laser [86]. The microdroplets are dispensed from a droplet generator inside a vacuum vessel with a background pressure of approximately 10^{-6} mbar. The beam profile of the PP laser is Gaussian of with a spatial full width at half maximum (FWHM) of 97 µm. The temporal profile is a Gaussian with a FWHM of 29 ns. For the presented experiments a constant PP energy of 6.8 mJ was used. The PP deforms the droplets into thin sheet targets which are radially symmetric and thickest in their center [11, 87, 12, 88, 17]. The target diameter is controlled via a time delay between the pre- and main pulses, and for our experiments the time delay is set to 2000 ns, leading to a target diameter of ~ 320 µm.

After the PP, the targets are irradiated with a high-intensity 1-µm-wavelength main pulse (MP) from a Nd:YAG laser. The pulse duration of the MP is 10 ns and the focal spot has a Gaussian beam profile with a FWHM of 103 µm. For the presented experiments, a fixed laser intensity of 2.3×10^{11} W/cm^2 was employed using a pulse energy of 293 mJ. The intensity was calculated as described in Ref. [15]. Additional details regarding the droplet-based experimental setup can be found in Ref. [11]. Finally, a simplified scheme of the experimental setup is presented in Fig. 3.1.

The spectral emission from the Sn laser-produced plasma is recorded using a broadband transmission grating spectrometer [62, 63] which is placed under an angle of 60° with respect to the incoming laser light. The different elements in the TGS are shown schematically in Fig. 3.1. The spectrometer is operated with a slit width of 50 µm and a 1000 lines/mm transmission grating, achieving a FWHM instrument resolution of 0.8 nm at 13.5 nm [62]. The use of the 1000 lines/mm transmission grating allows one to record emission in the 5.5–265.5 nm wavelength region. The limits

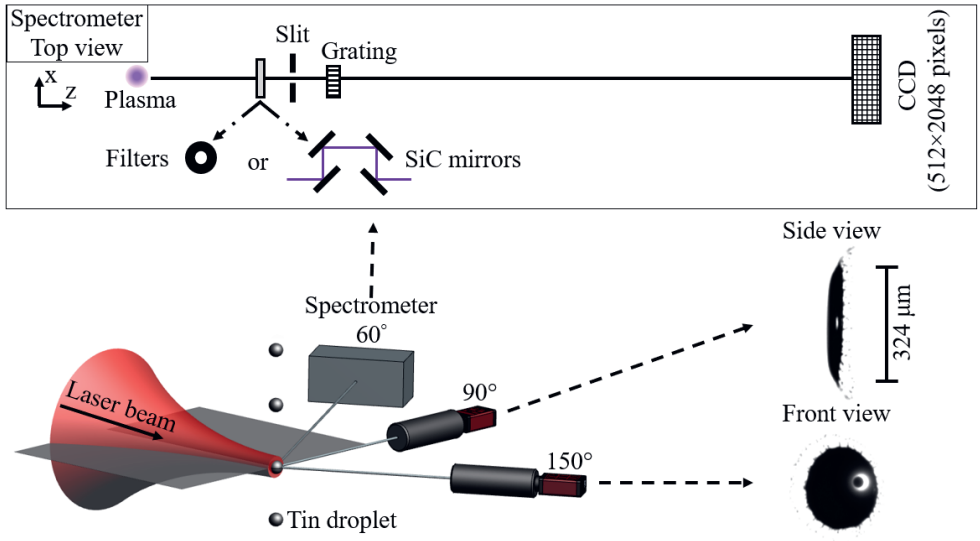

Figure 3.1: Experimental setup showing the front- and side-view shadowgraphs of the tin targets used for plasma generation as recorded by two cameras. The upper, boxed figure is a schematic of the transmission grating spectrometer.

to this specific 5.5–265.5 nm range are set on the short wavelength side by the onset (> 5.5 nm) of the availability of calibration data for the diffraction grating (see Section 3.3.2). On the long wavelength side, the limit (< 265.5 nm) is due to the geometry of the spectrometer. Furthermore, the spectrometer contains Zr, Si, Al, LiF, MgF_2, UVFS as well as SiC mirrors as tabulated in Table 1. The Zr, Si, and Al filters are foil filters with a common thickness of 200 nm. The foils are supported with a Ni mesh with 10 lines/inch period. The SiC system comprises four bulk-SiC mirrors which are placed under an angle of 45° with respect to the optical axis (see Fig. 3.1). The transmission grating, the filters Zr, Si, Al and the SiC mirrors are calibrated at the beamline facilities of the Physikalisch-Technische Bundesanstalt (PTB), at the BESSY-II synchrotron, Berlin, limited to wavelengths > 5.5 nm. The LiF, MgF_2 and UVFS filters are calibrated for wavelengths down to 115 nm using a vacuum-ultraviolet spectrograph equipped with a deuterium lamp.

The diffracted light in the TGS is recorded on a back-illuminated charge-coupled device (CCD) from Greateyes GmbH (GE2048 512BI UV1). The CCD is cooled to -30°C to reduce thermal noise. Background images are then subtracted from the recorded spectra to eliminate the dark counts as well as read-out noise. The resulting CCD images are cropped and corrected for shear and tilt that may be introduced by a misalignment of the slit and the grating with respect to the CCD pixel array. Next,

Filter material	Filter type	Thickness	Short wavelength cut-off (nm)
Zr	Foil	200 nm	6.1
Si	Foil	200 nm	12.5
Al	Foil	200 nm	17
SiC	Mirrors	1 mm	55
LiF	Window	2 mm	129
MgF_2	Window	2 mm	$<115^*$
UVFS	Window	2 mm	165

Table 1: Filters used in the spectral measurements with the transmission grating spectrometer. All short wavelength cut-offs are specified at 50% of the maximum transmission shown in the figures. * At 115 nm the transmission is ∼53% of the maximum.

the pixel counts are averaged along the non-dispersive axis and corrected for the respective exposure times. The resulting spectra are then corrected for filter efficiency, the first-order diffraction efficiency of the grating, the camera response and the solid angle of the spectrometer. The spectrometer has a solid angle of 37×10^{-11} sr that is calculated using the slit width, pixel size and the distance to the plasma.

For the wavelength calibration, a measurement with the Al filter is used. The sharp filter edge at 17.056 nm [29] and its higher orders enable accurate calibration of the wavelength axis. Here, the higher diffraction orders are advantageous - for wavelength calibration.

3.3 Results

In this section, three necessary types of corrections are applied to the raw spectra, namely the (A) filter transmission, (B) grating diffraction efficiency, and (C) CCD response.

3.3.1 Filter transmission

Spectra were recorded in the 5.5–265.5 nm wavelength region using different filters. The advantage of capturing spectra using different filters is that each filter allows for the measurement of different wavelength regions clear from higher order contributions. In the following, we sub-divide our discussion of the 5.5–265.5 nm spectra into three regions: (1) 5.5–40 nm, (2) 40–115 nm and (3) 115–265.5 nm, and we discuss each region individually.

5.5–40 nm wavelength range

For the investigation of the 5.5–40 nm wavelength range we recorded four sets of spectra using (i) no filter and the filters (ii) Zr, (iii) Si, and (iv) Al. The measured spectra are presented in Fig. 3.2(a).

The Zr filter has a cut-off at ∼6.1 nm which allows for recording a higher-order-free tin LPP spectrum in the ∼6.1–12.2 nm region. The Si filter exhibits a cut-off at ∼12.5 nm so in that way the spectrum is pure in the range of ∼12.5–25 nm. The Al filter has the advantage of a longer wavelength cut-off at ∼17 nm such that all orders of the strong 13.5 nm emission feature are absent and a clean measurement in the range ∼17-34 nm is possible.

The transmission functions of the various filters are tabulated in the CXRO database [29], however such transmission data is only valid for pristine samples. These filters typically suffer from oxidation and are subject to contamination from hydrocarbons and tin deposition. To obtain reliable transmission functions, the filters are calibrated at the PTB in Berlin. The calibration results are shown in Fig. 3.2(b), (c) and (d). The calibration procedure comprises two steps. First, for each filter type, the entire filter area was sampled at a single wavelength (13.5 nm for the Al filter, 17.5 nm for the Si and Zr filters) using a 0.5x0.5 mm^2 beam, enabling to obtain a detailed "map" of the transmission. Second, at one particular position on the filter (indicated by red squares in the inset figures), the full wavelength range is measured. The recorded transmission function was subsequently scaled by a factor proportional to the average transmission at the wavelength of the first measurement step (within the filter window indicated by the black circle in the inset figures). The error bars on this scaled transmission curve (red data points in Fig. 3.2(b), (c) and (d)) represent one standard deviation from the average across the filter.

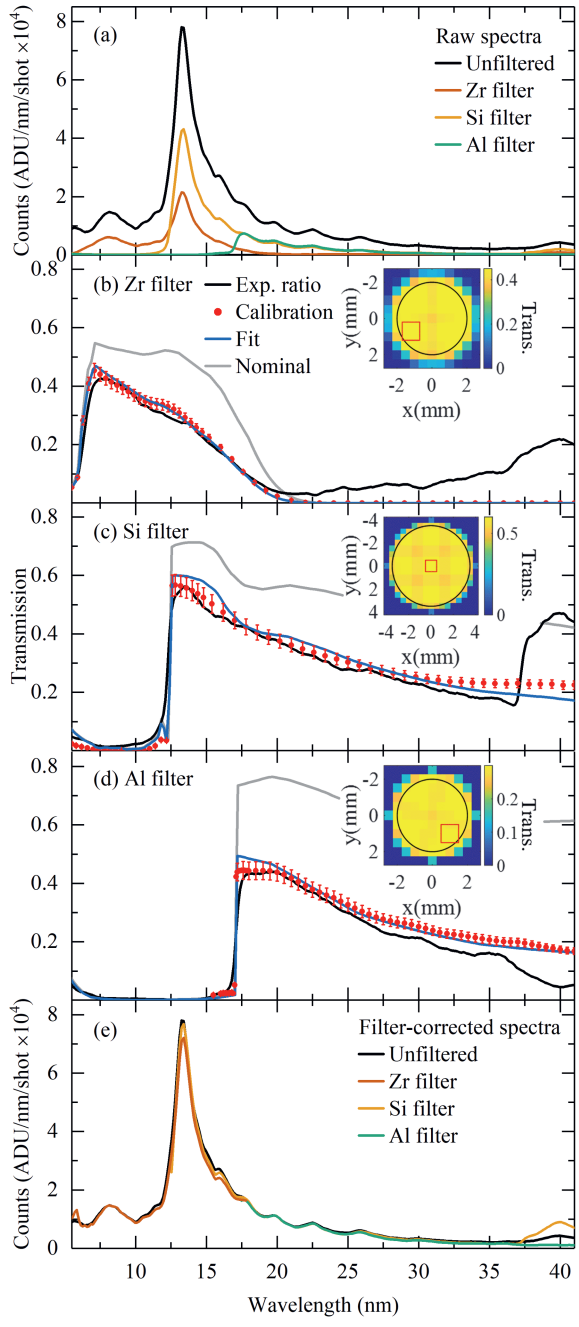

Figure 3.2: (Caption on the following page).

Figure 3.2: (a) Raw emission spectra obtained from tin LPP using Zr, Si, and Al filters, as well as using no filter. ADU: arithmetic digital unit. Filter transmissions for (b) Zr, (c) Si and (d) Al filters. The experimental ratio is the result of the division of the respective filtered by the unfiltered spectra; the calibration is from PTB; and the fitted curve is obtained taking oxidation into account, while the nominal one is the transmission obtained CXRO. Insets: Transmission maps measured at 13.5 nm for Zr and Si, and at 17.5 nm for Al. Red squares depict the location of the filter used for the wavelength scan. (e) Spectra corrected for the respective filter transmission functions.

Superimposed in black in the same figures are experimental estimates of the transmission function. These estimates are obtained by dividing the respective filtered spectra by the unfiltered spectra. These ratios may serve only as estimates as they are influenced by higher diffraction orders.

In all cases, the filter transmission is significantly lower than theoretical transmission that would be obtained from the CXRO database using the nominal thickness (shown as light gray lines). In an attempt to quantitatively explain the differences between the calibration and nominal CXRO database entries, we simulate the influence of finite oxidation of the filter surfaces using the following equation (Al as an example):

$$T = e^{(-n_{Al}\mu_{Al}d_{Al})} \times e^{(-n_{Al_2O_3}\mu_{Al_2O_3}d_{Al_2O_3})} \tag{3.1}$$

The symbols n, μ and d represent the number of atoms per unit volume, atomic photo-absorption cross section and thickness of the material, respectively. Thin film interference effects are verified to be negligible. We also accounted for the thickness of the non-oxidized part of the filter and the fraction of the filter material in the oxide layer sums up to the nominal thickness. The fraction of the filter material in the oxide layer is calculated by considering the atomic weights of the pure filter material and the oxidized filter material. For Al this fraction is calculated as $W_{Al}/W_{Al_2O_3}$, where W is the atomic/molecular weight.

This consideration allows fitting the $T(\lambda)$ function to the PTB measured transmission curve with a single free fit parameter, namely the thickness of the oxide layer. The fit results shown in Fig. 3.2 are in good agreement with the calibration data. The obtained oxide thicknesses range from 17 nm in the Al filter case to 49 nm in the Zr filter case. We find optimum agreement between the simulated and experimentally-determined calibration curves for oxide layer thickness of 49 nm ZrO_2 layer (with 169 nm pure Zr remaining), 19 nm SiO_2 (192 pure Si) and 17 nm Al_2O_3 (193 nm pure Al). The substantial oxide layers (we assume the oxide layer is divided between front and back sides of the filter) are in fact in agreement with the expected oxide layer thickness of such metal foils. More specifically, it has been shown in Ref. [89]

using Auger depth profiling, a 100 nm thick Zr filter can have 10 nm thick oxide layers on both sides of the filter. The total oxide layer thickness in Ref. [89] is of the same order of magnitude as the oxide layer thickness we have found. The same study[89] further shows that carbon and carbide mixed with Zr is also present throughout the filter, decreasing the transmission further. Since carbon and carbide mixing is not taken into account in our analysis, our calculations may overestimate the ZrO_2 layer thickness. For the Si filter, a total oxide layer thickness of 66 nm has been reported, somewhat thicker than what we found [90]. For the Al filter, oxide thicknesses around 15 nm have been reported, which matches well with 17 nm thickness that is found here [90, 91]. All in all, the PTB-calibrated transmission curves can be well understood from our model assuming a relatively thick oxide layer coating the pure filter surfaces.

Next, the spectra are corrected with the filter transmission data from PTB, the results of which are shown Fig. 3.2(e). The corrected spectra are shown starting from the short wavelength cut-off of each filter onward till the calibrated transmission drops below 10%. The corrected spectra are in very good agreement with each other (cf. Fig. 3.2 (e)). The dominant remaining difference is visible at 40 nm wavelength and can be attributed to the third-order contribution of the main emission feature at 13.5 nm that here only impacts the unfiltered spectrum and the Si filtered spectrum (the Zr-filtered spectrum is shown up to 18 nm where the transmission drops below 10%). The Al-filtered spectrum is free of this third-order diffraction feature and will be used for this wavelength range.

40–115 nm wavelength range

For the investigation of the 40–115 nm wavelength range we use the SiC mirrors. In Fig. 3.3(a), the spectrum obtained using the SiC mirrors is presented. In the same figure a scaled unfiltered spectrum is also presented for comparison. The peak in the unfiltered spectrum in the 65–70 nm range can be attributed to the fifth diffraction order of the dominant 13.5 nm emission feature. The spectral intensities in the SiC mirrors measurements are between two and three orders of magnitude lower than the unfiltered spectrum.

The SiC mirrors were sent to PTB for calibration in order to measure its total reflection efficiency. The resulting calibration is compared to the theoretical response curve in Fig. 3.3(b). The difference can be attributed partially to contamination but also to scattering due to roughness.

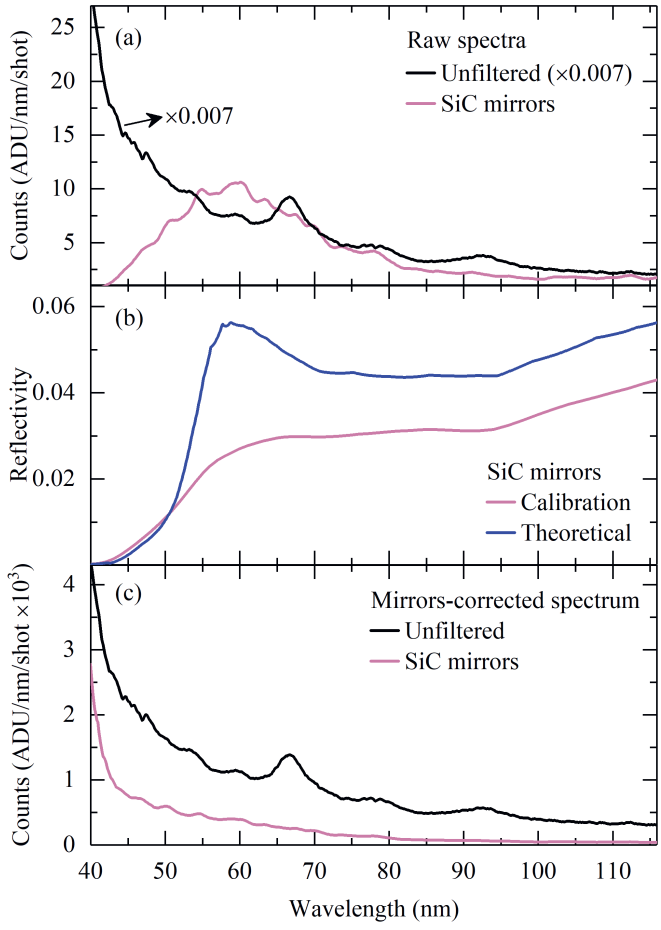

Figure 3.3: (a) Raw tin LPP emission spectra using the SiC mirrors as well as no filter. The unfiltered spectrum is multiplied by $\times 0.007$ for better visibility. (b) SiC mirrors reflectivity curves: one calibrated by PTB and one from theory (see main text). (c) Unfiltered spectrum and spectrum corrected for the SiC mirrors reflectivity.

The LPP spectrum is then corrected with the reflectivity calibration data from PTB, the results of which are shown in Fig. 3.3(c). The unfiltered and SiC filtered spectra show significant differences, highlighting the important contribution from higher orders to the spectrum and emphasizing the need for suppression of higher orders using filters as is done here.

115–265.5 nm wavelength range

To investigate the 115–265.5 nm wavelength range we have recorded spectra using (i) no filter and the filters (ii) LiF, (iii) MgF_2, and (iv) UVFS. The spectra are shown Fig. 3.4(a). The spectrum with the LiF filter extends smoothly below 115 nm but the spectrum recorded using the MgF_2 filter exhibits a steep decrease. The UVFS filter has the longest cut-off wavelength at 165 nm. All filters transmit at wavelengths above 265.5 nm which is the limit of the measurement range, set by the spectrometer.

In Fig. 3.4(b), the calibrated transmission efficiency curves of the three filters used for this wavelength region are presented. Since the upper limit of the wavelength axis of our recorded spectra is $\sim$265.5 nm, a combination of two of the filters (either LiF or MgF_2 with UVFS) in the 115–265.5 nm range will fully suppress all higher order contributions.

We present the filter-corrected spectra in Fig. 3.4(c). The three filter-corrected spectra are generally in good agreement with each other. The most significant difference, occurring below 120 nm, is related to the accuracy of the onset of the transmission of the MgF_2 filter and the precision of the relative wavelength calibration of the experiments and calibration. The comparison between the unfiltered spectrum to the filter-corrected spectra highlights the prominent contribution from high diffraction orders. The apparent intensity, i.e., counts, of the unfiltered spectrum is more than an order of magnitude stronger than the true signal, thus emphasizing the need to use filters.

In Fig. 3.5 we present the full spectrum in the 5.5–265.5 nm wavelength range obtained from concatenating the filtered spectra using only their respective ranges free of any higher diffraction orders. The individual y-axis values are shown to accurately "connect" at the respective overlap regions. We note that no free fit factors have been used to obtain this match. Instead, it is the accurate calibration of the filter transmissions that enables this good agreement. As seen before, strong contributions from higher diffraction orders are visible. In particular the odd multiples of the main 13.5 nm emission feature stand out, starting from the third diffraction order.

3.3.2 Grating diffraction efficiency

The first-order diffraction efficiency of the grating is shown in Fig. 3.6(a), as obtained from calibration at PTB. The feature that stands out is the "kink" near 12 nm that originates from the Si L-edge absorption in Si_3N_4 material present in the transmission grating [62].

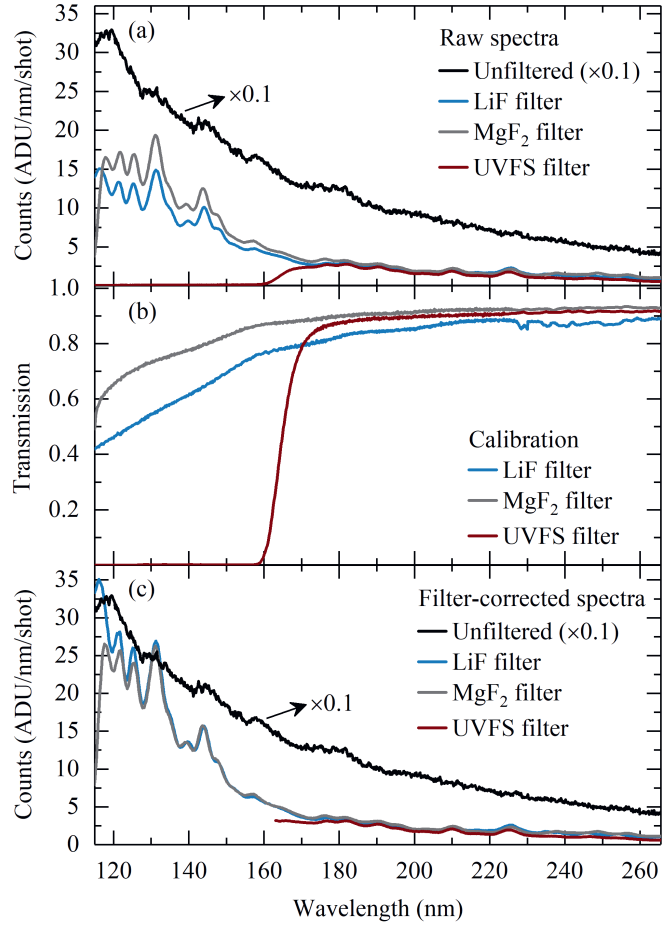

Figure 3.4: (a) Raw emission spectra from a tin LPP using the LiF, MgF_2 and UVFS filter as well as no filter. The unfiltered spectrum is multiplied by $\times 0.1$ for better visibility. (b) Filter transmission curves for the various filters. (c) Spectra corrected for the respective filter transmission functions.

3.3.3 CCD response

The CCD camera response is a product of three components: the gain, quantum yield (QY) and quantum efficiency (QE) [94]. The gain relates the ADU to the generated electrons and has the units of ADU/e^-. For the camera that is used in this experiment, the camera gain is specified by the manufacturer [92] as 0.83 ADU/e^-.

The QY is defined as the number of electrons generated per detected photon, and

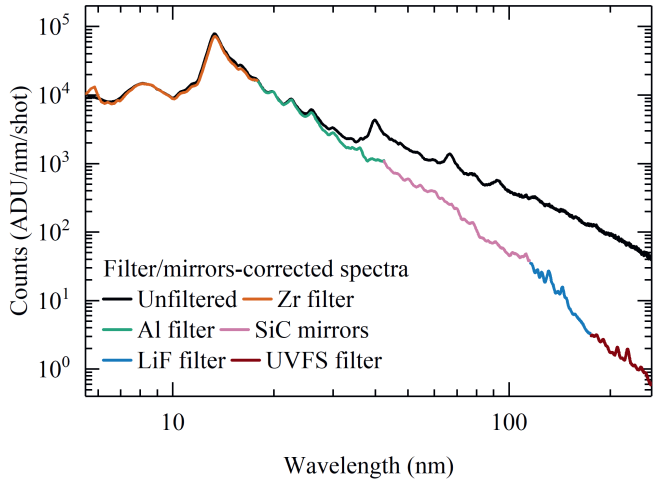

Figure 3.5: Concatenated spectra from tin LPP using the various filters, corrected for the respective transmission functions (see main text). The chosen range for each spectrum is free of any higher diffraction orders. The unfiltered spectrum is also shown for comparison.

is proportional to the energy of the photon. A typical assumption in the EUV and VUV wavelength ranges [93, 95] is that a photon energy of 3.66 eV, which corresponds to the indirect bandgap of Si, is needed to generate an electron. A detected photon of energy E would thus generate $E/(3.66\,\mathrm{eV})$ electrons. As pointed out also by Heymes *et al.* [95] this assumption breaks down in the optical range where QY will instead converge to a value of one (1). In the here studied wavelength range, however, the simple $1/3.66\,e^-/\mathrm{eV}$ rule is in good agreement with a more detailed treatment [93, 94]. Correcting for QY enables converting the number of electrons to the number of detected photons, or to the amount of detected energy in units of eV with a proportionality constant of 3.66. Hence, the QY for the wavelength range explored in this work can be written in units of e^-/eV or e^-/mJ as $\mathrm{QY} = 1/3.66\,e^-/\mathrm{eV} = 1.71 \times 10^{15}\,e^-/\mathrm{mJ}$.

The QE is defined as the ratio of the number of detected photons to the number of photons arriving on the detector surface. Hence, it is also equal to the ratio of detected to incident energy. In Fig. 3.6(a) we show two such quantum efficiency curves. The first is obtained from the manufacturer of the CCD used in our experiments [92]. We note however that the calibration provided by the manufacturer depends, in part, on simulations and not experiments [96]. According to their simulations, the sharp edge around 120 nm originates from thin film interference, assuming a sharp interface between the assumed SiO_2 layer and the active Si CCD surface. In reality, the

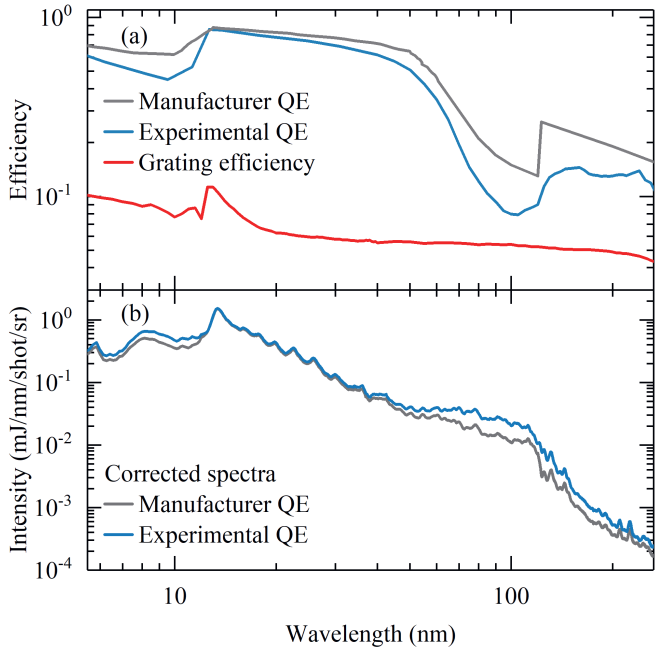

Figure 3.6: (a) Grating efficiency for the first diffraction order and QE of the CCD camera, comparing manufacturer QE [92] or experimental QE [93] data (see main text). (b) Concatenated spectra (cf. Fig. 3.5) after correcting for the diffraction efficiency of the grating, the CCD response using either manufacturer or experimental QE data and solid angle.

boundary is expected to be less sharp due to intermixing. As a result, the QE curve is expected to have a smoother shape. In search of experimental support for our QE calibration we employ the recent results [93]. Further experimental QE studies are found in previous works [96, 97, 98]. Comparing the two QE curves in Fig. 3.6(a) we note that there is a striking difference near 120 nm where a sharp, steep edge is visible in the QE from the manufacturer which is not supported (either in amplitude or shape) by recent experimental work [93]. The differences between the available QE curves may be due to dissimilarities in manufacturing processes or, for instance, to possible aging effects. Considering the significant differences, the overall uncertainty in our final spectrum is expected to be dominated by the QE curve.

As the final step, the concatenated spectra of Fig. 3.5 are corrected for the camera response (gain, QY, and QE) together with the solid angle of the spectrometer (37×10^{-11} sr) and the resulting corrected full-range spectrum is shown in Fig. 3.6(b). Integral energies emitted in the various wavelength ranges, following the filters used, are presented in Table 2. The final corrections, using either QE curve, pro-

Wavelength range (nm)	Corresponding filter	Energy (mJ/shot/sr)	(%) of total energy
5.5–17.5	Zr	7.1	54.7
(13.5 nm ±1%*)	(Zr)	(0.4)	(3.1)
17.5–42.5	Al	4.2	32.5
42.5–115	SiC	1.5	11.4
115–175.5	LiF	0.2	1.2
175.5–265.5	UVFS	0.03	0.2
Total energy		13.0	

Table 2: Energy emitted towards the spectrometer, i.e. under a 60° angle cf. Fig. 3.1, in the various wavelength ranges using manufacturer QE data cf. Fig. 3.6. *The value for the energy emitted in the 2%-wavelength bandwidth centered around 13.5 nm is impacted on by the limited resolution of the spectrometer (0.8 nm at 13.5 nm).

duce a "knee" near 120 nm wavelength that is not visible in the concatenated data of Fig. 3.5 which may point at a discrepancy between the true QE and the available QE curves.

Further corrections for the source size (possibly weakly wavelength-dependent) and for the precise time dependence of the transient emission are required to interpret the obtained intensity in terms of spectral radiance. These steps are left as future work but may be expected to have only limited impact on the overall shape of the emission spectrum as shown in Fig. 3.6(b). Nevertheless, the obtained spectrum enables diagnosing the energy distribution of the LPP that is useful for optimizing the LPP based EUV sources.

3.4 Conclusions

We present a fully calibrated spectrum in the 5.5–265.5 nm range from a microdroplet-tin Nd:YAG-laser-produced plasma. The spectrum, obtained using a transmission grating spectrometer, is the result of a careful calibration of a series of filters enabling measurements free of any higher diffraction orders. Specifically, we use Zr, Si, Al foil filters and bulk LiF, MgF_2, and UVFS filters. A further filter using four SiC mirrors

is used to record the otherwise inaccessible 40–100 nm region. The photon energy in this particular wavelength range is significant and provides input for further studies on the impact of EUV-induced-plasma in the EUV source vessel. The fully corrected and concatenated spectra are shown to accurately match in their respective overlap regions demonstrating the accuracy of the calibration procedure. The dominant remaining uncertainty stems from the correction for quantum efficiency. Our calibration enables the optimization of current and future sources of EUV light for nanolithography by providing metrology for minimizing the emission of unwanted wavelength bands that may limit imaging contrast or even impact machine uptime.

3.5 Acknowledgments

Part of this work has been carried out within the Advanced Research Center for Nanolithography, a public-private partnership of the University of Amsterdam, the Vrije Universiteit Amsterdam, the Dutch Research Council (NWO) and the semiconductor equipment manufacturer ASML and was financed by Toeslag voor Topconsortia voor Kennis en Innovatie from the Dutch Ministry of Economic Affairs. The transmission grating spectrometer was developed in the Industrial Focus Group XUV Optics at the University of Twente and supported by the FOM Valorisation Prize 2011 awarded to F. Bijkerk and NanoNextNL Valorization Grant awarded to M. Bayraktar in 2015. This project is funded by TKI-HTSM with the project name "Spectral Unraveling of EUV Lithography Light Sources (SUN)". This project received further funding from the European Research Council Starting Grant No. 802648 and is part of the VIDI research programme with Project No. 15697, which is financed by NWO. The authors would like to thank Dr. Julian Heymes (The Open University, Milton Keynes, UK) for his valuable contribution to this manuscript.

Chapter 4

Radiation from a 2-µm-wavelength-driven tin microdroplet laser-produced plasma in a 6.5–264.5 nm wavelength band

Z. Bouza, Y. Mostafa, L. Behnke, R. Schupp, W. Ubachs, R. Hoekstra, M. Bayraktar, and O. O. Versolato. Manuscript in preparation.

Abstract

We present a wavelength and intensity calibrated spectrum in the 6.5–264.5 nm range from a microdroplet tin plasma produced using a ns-pulsed 2-µm-wavelength drive laser, which may efficiently drive future plasma sources of extreme ultraviolet light at 13.5 nm for nanolithography. The plasma emission spectrum is obtained by means of a transmission grating spectrometer and is free of higher diffraction orders by concatenating spectra from a series of filters. A comparison between spectra at various laser pulse energies is made. We observe that in all cases the dominant radiative contribution comes from the EUV range (5–70 nm). A relatively broad range of laser pulse energies (100–250 mJ) was found to efficiently produce useful EUV radiation in a 13.2–13.8 nm wavelength band. The further comparison with a spectrum obtained from plasma driven by a 1-µm-wavelength drive laser highlights the higher efficiency of the 2-µm laser for producing 13.2–13.8 nm EUV radiation. The 1-µm wavelength laser light produces predominantly more light over a wider 5–70 nm wavelength range at the expense of emission in the useful 13.2–13.8 nm wavelength band. We next identify key emission features in the ∼15–37 nm wavelength band using results from Cowan and FAC atomic codes, and further find evidence for increasing plasma emission size with increasing wavelength.

4.1 Introduction

Extreme ultraviolet (EUV) light generated from liquid-tin laser-produced plasma (LPP) is used in state-of-the-art nanolithography [5, 4, 6, 7, 9, 10, 41, 8]. Tin LPP emits strongly at wavelengths near 13.5 nm, matching the optimum reflection wavelength of optics available in the EUV range. The radiation originates from electronic transitions between multiply excited states [49] in highly charged tin ions Sn^{10+}–Sn^{15+} [18, 19, 20, 21, 22, 23, 24, 25, 26]. The electronic structure of the tin ions enables a high conversion efficiency (CE) of the laser light into "in-band" radiation, defined as the radiation in a 2% bandwidth centered at 13.5 nm that can be efficiently used in a lithography tool.

To achieve high conversion efficiencies, a specific experimental procedure should be followed. First, a low-intensity pre-pulse (PP) deforms the tin microdroplets into disk-like shapes such that the main pulses (MPs) can interact more efficiently with the targets [5, 4]. Currently, 10.6-µm-wavelength CO_2 gas lasers are used to provide the main pulses to drive plasmas for industrial EUV lithography purposes, reaching a CE value of up to 6% [5]. Recently, 2-µm-wavelength solid-state lasers have been used to deliver main pulses for research purposes [13], achieving a CE of 3% in preliminary experiments [17]. Lasers operating near 2-µm wavelength, and also at 1-µm, may offer significant benefits over the CO_2 gas lasers, e.g., in terms of wall plug efficiency (i.e, converting electrical power to light). Higher CE values may be expected with further upgrades of the experimental setup and the 2-µm laser system, to be able to better match the conditions of recent simulations which predicted a $\sim$5% CE [99].

One of the most important advantages of the strong emission peak of 13.5 nm of such tin LPPs is that this radiation matches the peak reflectivity of multilayer mirrors used in industrial lithographic machines [43, 44]. For this reason, most of the spectroscopy-related works focused on the in-band wavelength region [27, 41, 49, 45, 46, 47] and the nearby out-of-band (OoB) EUV emission [24, 46, 52, 53, 15, 14, 74]. At longer wavelengths, such as vacuum-ultraviolet (VUV) or deep-ultraviolet (DUV) ranges, the available spectroscopic information is limited. Available works present either VUV or DUV speactra without also showing the EUV region [76, 77, 78, 79, 27], while when the EUV region is shown, then the VUV is typically not included [81, 82, 83, 84, 33, 85].

In a recent study [100], a fully calibrated spectrum from a 1-µm-wavelength-driven LPP in the 6.5–264.5 nm wavelength regime was presented. A study of this larger wavelength range is of particular importance as part of the VUV and DUV radiation may be transported by the multilayer mirrors onto the wafer. Due to the still large

photon energy, the chemical processes on the wafer can be influenced, and this can negatively impact imaging contrast and quality [100, 50, 51]. Moreover, the wavelength range of 30–90 nm is absorbed by the hydrogen that is present as a buffer gas in the EUV source vessel. Photoionization and - dissociation of these molecules may generate secondary plasma that could influence the quality of the optical components [32]. Therefore, a detailed study of the radiation from a 2-µm-wavelength-driven LPP over a wide wavelength range is valuable for assessing its application potential.

In the following, we present fully calibrated 2-µm-wavelength-driven tin microdroplet LPP spectra in the 6.5–264.5 nm wavelength regime. First, we present and analyze 2-µm LPP spectra obtained at various laser pulse energies. Next, we add the fully calibrated 1-µm-wavelength-driven tin microdroplet LPP spectra presented previously by Bouza *et al.* [100] and discuss similarities and differences with the 2-µm LPP. We subsequently calculate the energy emitted in the various relevant wavelength bands of all 2- and 1-µm spectra. Finally, we use Cowan and FAC atomic codes to identify emission features of the multiply-charged Sn^{4+}–Sn^{10+} ions, in the ∼15–37 nm wavelength regime of the tin LPP spectrum.

4.2 Experimental setup

In this section, we present and explain the experimental setup that is schematically represented in Fig. 4.1. For the 2-µm laser light experiments, liquid tin microdroplets of ∼39 µm diameter are first irradiated with a relatively low intensity ($\sim 10^9$ W/cm^2), 1-µm wavelength pre-pulse (PP) from an Nd:YAG laser. Microdroplets are dispersed from a droplet generator inside a vacuum vessel with a background pressure of approximately 10^{-6} mbar. The beam profile of the PP laser is Gaussian with a spatial full width at half maximum (FWHM) of 60 µm. Its temporal profile is Gaussian with a FWHM of 10 ns. For these experiments, a single PP energy of 8 mJ was used. The PP deforms the droplets into disk-like targets with a 120 µm diameter (also see Refs. [87, 12, 88, 17] for further information). As described in Chapter 3, the target diameter is controlled through the time delay between the pre- and main pulses. For the current experiment, the time delay is set to 0.5 µs. A more detailed schematic of our experimental setup is shown in Fig. 3.1 of Chapter 3.

As the main pulse (MP), we use a high-intensity 2-µm wavelength laser pulse. The beam profile of the MP laser is a top hat with a spatial full width at half maximum (FWHM) of 80 µm. Its temporal profile approximates a top hat with a FWHM of 30 ns. For the needs of the experiments, the MP energy varies between 30 to 300 mJ (corresponding to MP intensities ranging approximately between 0.2 – 2 ×

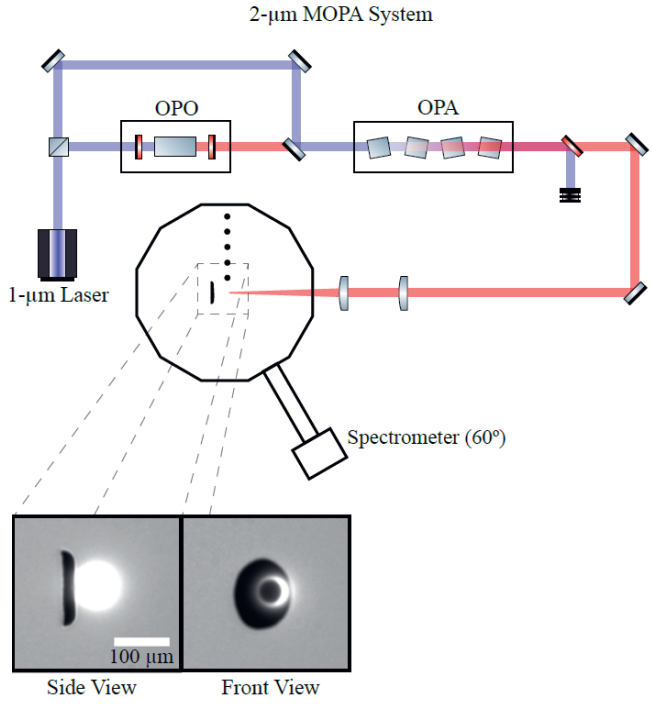

Figure 4.1: Schematic of the experimental setup. A 1-µm Nd:YAG laser is used to seed an Optical Parametric Oscillator (OPO) creating 2-µm light. This light is further amplified by an Optical Parametric Amplifier (OPA) and subsequently imaged onto the disk-like tin targets in a vacuum chamber. Light emitted from the laser-produced plasma is recorded on a spectrometer set up at an angle of -60 degrees with respect to the laser propagation direction. A side and front shadowgraphy view of the tin sheet target before laser impact is shown. The target is produced from the impact of an independent pre-pulse laser on a tin droplet, see main text. For simplicity, the pre-pulse is not included in the schematics.

10^{11} W/cm^2, assuming all energy is enclosed in the FWHM profile for simplicity). The pulses are produced in a home-built master oscillator power amplifier (MOPA) system built following the work of Arisholm *et al.* [101]. The current 2-µm laser system demonstrates tunable spatial and temporal profiles. More detailed information about the MOPA system, and on optimum intensity considerations, can be found in Ref. [75, 17, 13].

The 1-µm experiment has been also described in detail in Chapter 3. The procedure of this experiment is the same as for the 2-µm case. Briefly, first a relatively low-energy 1-µm wavelength PP from an Nd:YAG laser is used, and subsequently a high-energy 1-µm MP from an Nd:YAG laser follows (corresponding to an MP inten-

sity of $\sim 2 \times 10^{11}$ W/cm^2, close to the expected optimum following Ref. [15]). In this experiment liquid tin microdroplets of $\sim$46 µm diameter were used. The beam profile of the PP laser is Gaussian with a spatial full width at half maximum (FWHM) of 97 µm. Its temporal profile is Gaussian with a FWHM of 29 ns. A single PP energy of 6.8 mJ was used. The PP deforms the droplets into thin sheet targets of $\sim$320 µm. The pulse duration of the MP is 10 ns. The MP has a Gaussian spatial profile with a FWHM of 103 µm. For the current experiment, a single laser energy of 293 mJ was employed. A schematic of the specific experimental setup with 1-µm MP is shown in Fig. 3.1 of Chapter 3.

The spectral emission from the tin LPP is measured using a broadband transmission grating spectrometer [62, 63] (also see Chapter 3). The spectrometer is placed at an angle of 60° with respect to the incoming laser light. A single slit width of 50 µm was used to illuminate a 1000 lines/mm transmission grating, leading to an instrument resolution of 0.8 nm (FWHM) at 13.5 nm [62]. The use of the 1000 lines/mm transmission grating allows for capturing the LPP emission spectrum over a large wavelength range, spanning 6.5–264.5 nm. The spectrometer is equipped with various filters (see Table 1 of Chapter 3). These filters are used to avoid contributions from higher diffraction orders inserted from the transmission grating. More information about these filters and their calibration can be found in Chapter 3. A schematic of the transmission grating spectrometer used is provided in the Experimental Setup section of Chapter 3.

The diffracted light is measured on a back-illuminated charge-coupled device (CCD) from Greateyes GmbH (GE2048 512BI UV1) which is cooled to -30°C to reduce thermal noise. Background images are then subtracted from the recorded spectra to eliminate dark counts and read-out noise. The resulting CCD images are cropped and corrected for shear and tilt that may be introduced by a misalignment of the slit and the grating with respect to the CCD pixel array. After that, the pixel counts are averaged along the non-dispersive axis and corrected for the respective exposure times. After that, the resulting spectra are corrected for filter efficiency, the first-order diffraction efficiency of the grating, camera response, and the solid angle of the spectrometer. The spectrometer has a solid angle of 37×10^{-11} sr. In calculating the solid angle we considered the width of the slit in the dispersive direction and height of a CCD pixel in the non-dispersive direction. The choice of pixel height in the non-dispersive direction is due to the averaging of the pixel counts in the previous step.

The wavelength calibration was done in the same way as in Chapter 3, using a measurement with the Al filter. The sharp edge of the Al filter at 17.056 nm [29] and its higher orders allow for sufficiently accurate calibration of the wavelength axis.

4.3 Experimental results

In this section, we discuss the experimental results using a 2- and 1-µm drive laser wavelength. We start by presenting emission spectra of 2-µm tin LPP over a range of laser pulse energies. Next, we compare 2- to 1-µm tin LPP emission spectra. We then calculate and compare the energy emitted from all the presented spectra (of 2- and 1-µm) in various wavelength bins. Finally, we focus on a 2-µm LPP spectrum and identify emission features in the ∼15–37 nm range using the pre-existing Cowan code calculations supplemented by our calculations using the flexible atomic code (FAC).

4.3.1 2-µm-wavelength-driven tin LPP emission spectrum

In Fig. 4.2(a), emission spectra from tin LPP at several laser pulse energies using 2-µm laser pulses are presented. Each spectrum in this plot is the result of the concatenation of several emission spectra individually obtained using various filters (Zr, Al, SiC mirrors, LiF and UVFS), following Ref. [100], in order to reduce or even eliminate contributions from higher diffraction orders, e.g., from the strong emission peak at 13.5 nm wavelength. The presented spectra are normalized to the laser energy and are corrected for exposure time, background, filter efficiency, and 1^{st}-order grating diffraction efficiency. Note that the wavelength x-axis is on linear scale, while the y-axis is on logarithmic scale. In Fig. 4.2(b), the same spectra as in Fig. 4.2(a) are presented, but here both the x- and y-axis are on a logarithmic scale for improved visibility of the emission features. For all laser pulse energies, the 2-µm spectra look very similar around the in-band area, where the emissivity is at a maximum. Only the lowest energy 30 mJ case stands out as LPP plasma is clearly underheated, leading to lower emission in this regime particularly visible in panel (b) of Fig. 4.2. At shorter and longer wavelengths, the various spectra do show discrepancies. At shorter ∼6-10 nm wavelengths the effects of the increasing temperature of the plasma with increasing laser intensity are apparent in the increasing contribution of, e.g., $4p$-$5s$ transitions from the higher charge states [52]. At longer wavelengths, beyond approximately ∼20 nm, spectral differences become more pronounced with increasing wavelength. Increasing laser pulse energy appears to decrease the long-wavelength contributions while the short-wavelength out-of-band emission increases.

4.3.2 2-µm- *vs* 1-µm-wavelength-driven tin LPP emission spectra

In Fig. 4.3 we present the same data shown in figure 4.2(a) and add a spectrum from a 1-µm-laser-driven tin plasma (from Bouza *et al.* [100]) for ease of comparison. Again,

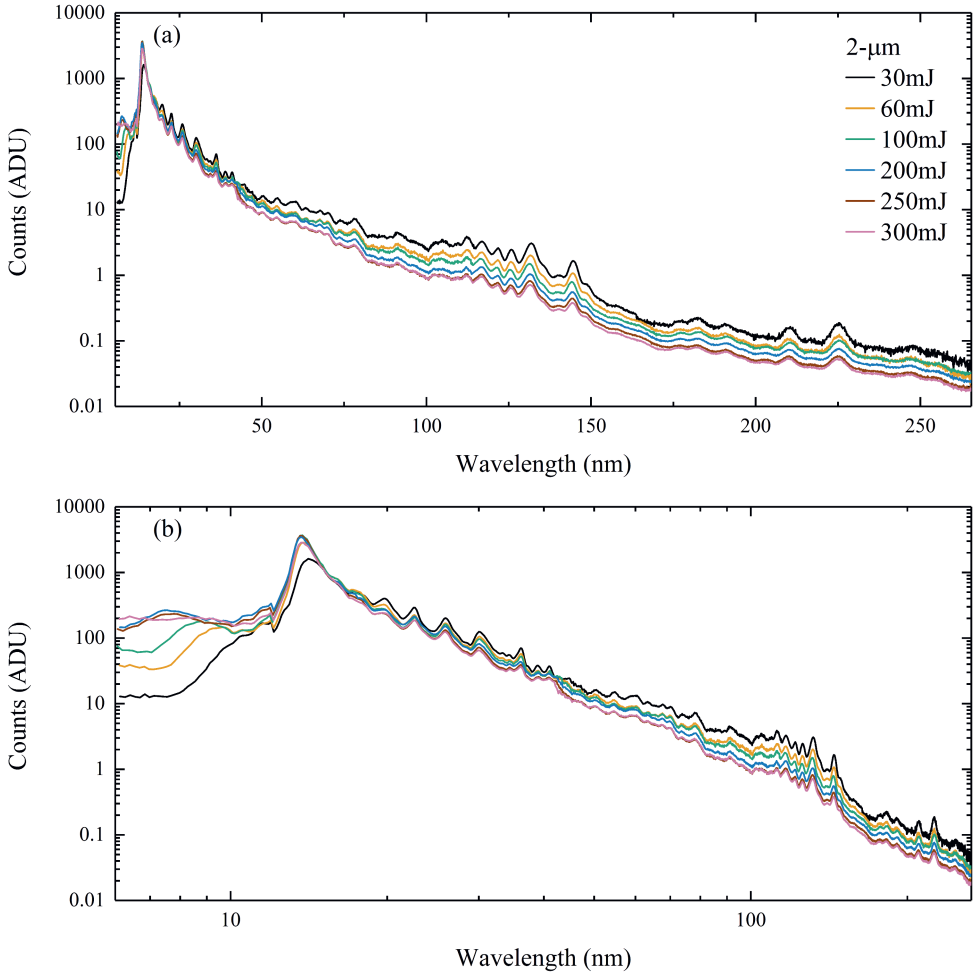

Figure 4.2: Emission spectra from a 2-µm-wavelength driven LPP. (a) Concatenated emission spectra using various filters (Zr, Al, SiC mirrors, LiF and UVFS) for different laser energies. The spectra are normalized to laser energy and are corrected for exposure time, background, filter efficiency, and 1^{st}-order grating diffraction efficiency. Note that y-axis in panel (a) is in log scale while x-axis in lin scale. (b) Same spectra as in (a), but here both x- and y-axis are in log scale. ADU: arithmetic digital unit (see Chapter 3).

all spectra are normalized to laser energy and are corrected for exposure time, background, filter efficiency, and 1^{st}-order grating diffraction efficiency. Furthermore, in contrast to the previous figures 4.2, in this figure we apply additional corrections for the wavelength-dependent CCD response, and for the solid angle of the spec-

trometer. More details about these corrections can be found in Bouza et al. [100] (see Chapter 3).

As in Chapter 3, the correction for the CCD response increases the visibility of a "knee" in the spectrum near 120 nm wavelength (compare panel (a) of Fig. 4.2 panel to Fig. 4.3) which may point at a discrepancy between the true CCD quantum efficiency (QE) and the available QE curves. If we now compare the spectra from the 2-µm to the 1-µm case, we see that the spectrum from the 1-µm case exhibits significantly higher emission intensity in the 13.5–80 nm wavelength range. At longer wavelengths >80 nm the difference becomes much less pronounced with the emission characteristics being very similar to the low-energy 2-µm cases. This is of particular interest, as there are notable differences between the experimental approaches comparing the 1-µm and 2-µm cases such as the different target sizes, and the different spatial and temporal profiles of the respective main pulses. These differences may contribute to the spectral differences beyond the change in drive laser wavelength, as discussed previously [13, 17].

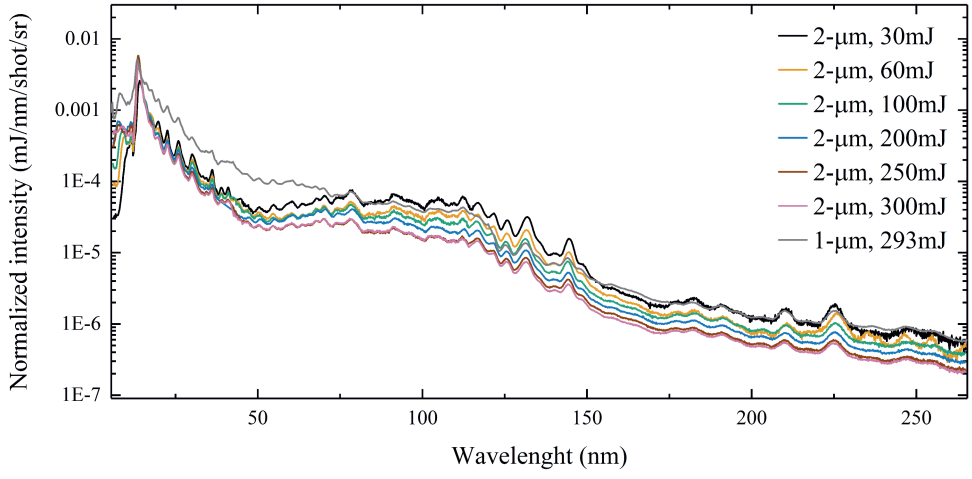

Figure 4.3: Concatenated emission spectra from 2-µm- and 1-µm wavelength LPP (cf. Fig. 4.2). The spectra are normalized to laser energy and are corrected for exposure time, background, filter efficiency, and 1^{st}-order grating diffraction efficiency, as well as for wavelength-dependent CCD response and the detector solid angle.

4.3.3 Quantitative assessment of the radiative energy distribution

Here we analyze the energy deposited in various wavelength ranges of the spectra in Fig. 4.3. The definitions of wavelength ranges that are commonly used in the

industry are listed in Table 1 [102]. To clarify the choice of the specific wavelength bins, we expand this table by including the corresponding physical processes and the induced effects. It should be noted that the correspondence between the wavelength ranges and the physical processes is tentative, i.e. some of the wavelength ranges are broader than the listed physical process. Moreover, we appreciate that the industry naming convention opted for here is not consistent with the commonly used naming in the literature for the VUV and DUV ranges, hence we denote our wavelength ranges with an asterisk (*).

The first wavelength range is the EUV full-band (FB) range, which is set from 13.2 nm to 13.8 nm. This wavelength range is reflected by the Mo/Si multilayer mirrors used in the scanner, even though the reflectivity reduces outside the 13.5 nm$\pm$1% band that is exposing the photoresist on a wafer. The EUV out-of-band (OoB) covers the range of 5–70 nm excluding the EUV-FB. This range is not reflected, but absorbed by the mirrors or partly transmitted to the mirror substrate hence can cause mirror heating and lifetime issues in the illuminator. The presence of consecutive multilayer mirrors in the EUVL scanners reduces this EUV-OoB in each reflection, so this range is not expected to reach the wafer. The next, vacuum ultraviolet (VUV*) range between 70 and 130 nm is effectively absorbed by the background hydrogen gas present in the EUVL source and scanner chamber, but this suppression decreases above $\sim$112 nm. As was pointed out in the Introduction of this Thesis, H_2 gas significantly absorbs light with wavelengths shorter than 112 nm, where the molecular hydrogen photodissociates. The H_2 ionization threshold lies at 80.3 nm [31], from which point on photoionization adds to the photoabsorption cross-section (see Fig. 1.1). After a peak in absorption cross-section relatively close to the ionization threshold, the absorbance rapidly decreases with decreasing wavelength facilitating a significant transmission of EUV light through the buffer gas.

The absorption in hydrogen prevents the light from reaching the wafer but it may ionize hydrogen gas and create a secondary plasma. The last range is the deep-ultraviolet (DUV*) range covering the 130–400 nm band. This range is important because the multilayer mirrors can still reflect significantly in this range. Typical photoresists at the wafer level are based on organic molecules that are sensitive to the light from 150 to 300 nm, thus DUV* may result in parasitic exposure and contrast loss. A more detailed treatment of the impact of light in these wavelength ranges on the imaging performance of an EUVL scanner can be found in Refs. [103, 104, 33, 85]. In our analysis the EUV-OoB is set at 6.5–70 nm (excluding EUV-FB) while the DUV* is set at 130–264.5 nm, due to the lower and upper limits of our spectral range. The wavelength ranges excluded in our experiments are either very narrow (5–6.5 nm) or the intensity is very low (264.5–400 nm) thus they do not significantly impact the amount of energy deposited in either the OoB or DUV* band.

Name	Wavelength range (nm)	Physical process
EUV-FB	13.2–13.8	Reflected by mirrors, lithography
EUV-OoB	5–70 (excl. EUV-FB)	Absorbed by mirrors, heat load
VUV*	70–130	Absorbed by H_2, secondary plasma
DUV*	130–400	Reflected by mirrors, contrast loss

Table 1: Definitions of the four wavelength ranges used to characterize the emitted energy. In our case the EUV-OoB is set as 6.5–70 nm (excl. EUV-FB) and DUV* as 130–264.5 nm.

For the data shown in Fig. 4.3 using the wavelength range definitions in Table 1, we calculated the energy contained in for each wavelength bin. These fractional amounts of energy are presented as a bar chart in Fig. 4.4. For the 2-µm spectra, we see that the EUV-FB significantly increases from 5% to 15% in the 30–250 mJ regime and slightly decreases to 12% at 300 mJ. We note that the 2-µm case presents a broad optimum in the 100–250 mJ range containing at least 14% of the total radiated energy. The EUV-OoB slowly increases from 77% to 81% in the same laser energy range but the relative change is smaller compared to the change in the EUV-FB range. VUV* energy reduces from 16% to 5% in the 30-250 mJ range and slightly increases to 6% at 300 mJ laser energy. This significant decrease has the opposite trend seen in the EUV-FB and approximately the same magnitude. It can be speculated that there is energy transfer from the VUV* range (via the EUV-OoB) to the EUV-FB range with increasing drive laser energy. The DUV* range in all 2-µm cases remains almost constant at a level of 1-2%. We also conclude that the case of 300 mJ concerns an overheated plasma as EUV-FB decreases and EUV-OoB increases. Comparing 2-µm and 1-µm energy distributions at the same drive laser energy of 300 mJ, we observe that the loss in EUV-FB is transferred to the EUV-OoB. We also notice that the case of 1-µm presents half of the maximum EUV-FB of the 2-µm case. This observation of an approximately two times higher EUV-FB generation efficiency of 2-µm compared to 1-µm is in line with a previous work [17].

4.3.4 Origins of emission features

In Fig. 4.5(a) we present the spectrum of an LPP driven by a 200 mJ, 2-µm wavelength laser pulse (cf. Fig. 4.3) and we next identify the emission features in the ∼15–37 nm wavelength regime, using Cowan and FAC atomic codes. The Cowan code is a semi-empirical code [54, 55], which allows for adjustment of the scaling factors in the model to fit the observed spectra using initial preliminary assign-

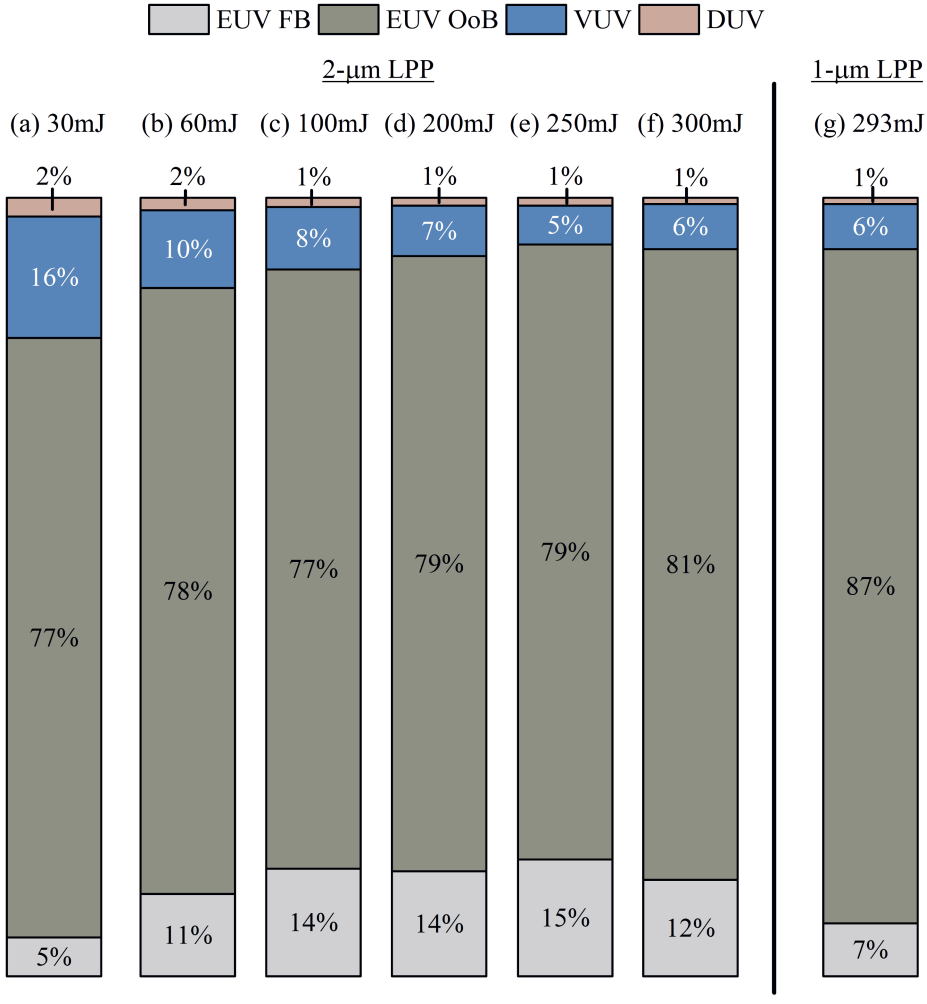

Figure 4.4: Energy emitted towards the spectrometer under a 60° angle in the various wavelength ranges for 2-µm and 1-µm LPP. (a) 2-µm, 30 mJ, (b) 2-µm, 60 mJ, (c) 2-µm, 100 mJ, (d) 2-µm, 200 mJ, (e) 2-µm, 250 mJ, (f) 2-µm, 300 mJ, (g) 1-µm, 293 mJ.

ments. More information on how we perform and use Cowan can be found in Chapter 2. FAC enables performing relativistic calculations of atomic structures including configuration-interaction [105], without any scaling factors. In the current work, we use FAC calculations for Sn^{4+}–Sn^{6+} and available Cowan calculations for Sn^{7+}–Sn^{10+}. We use the same Cowan results as in Chapter 2 but here we also add the Sn^{7+} ion

- also for this tin ion the Cowan calculations are performed exactly the same way as in Chapter 2. For the Sn^{4+}–Sn^{6+} ions, Cowan calculations are not available in the relevant wavelength range and we use FAC calculations instead. Finally, we limit the current analysis to the ∼15–37 nm wavelength range corresponding to the domain where readily identifiable 4*d*-5*p* excitations may be expected to dominate the emission.

For the FAC calculations, we use the following configurations for each tin ion to get our results. For Sn^{4+} we use the configurations $4d^{10}$, $4d^9 4f^1$, $4d^9 5p^1$; for Sn^{5+} $4p^6 4d^9$, $4p^6 4d^8 4f^1$, $4p^6 4d^8 5p^1$, $4p^5 4d^{10}$; and for Sn^{6+} we include $4p^6 4d^8$, $4p^6 4d^7 4f^1$, $4p^6 4d^7 5p^1$, $4p^5 4d^9$. This rather limited set of configurations was found to reproduce the atomic structure with sufficient accuracy for the current analysis.

All major emission features in Fig. 4.5(a) can be attributed to $4d$–$5p$ transitions of Sn^{4+}–Sn^{10+} ions. The codes' results accurately match the observed features of the spectrum. This type of transition ($4d$–$5p$) has been previously studied by Ohashi *et al.* [24]. Our calculated atomic data results are in good agreement with that work. We note that both in the work of Ohashi *et al.* and in the current work, no individual line assignments were made as there are thousands of lines contributing to these features, making line identifications of specific transitions effectively impossible.

In the same Fig. 4.5(a) we also plot a Planck curve for black body radiation to interpret plasma emission in terms of thermal radiation. This curve shows the maximum emissivity for any particular wavelength that can be achieved for thermal radiation (i.e. from a blackbody emitter) at 32 eV temperature. It has been scaled to match the 13.5 nm emission peak, where it is known that optical depth is significant and locally we should expect to meet the Planck curve, following work by Schupp *et al.* [14] on Nd:YAG-laser driven plasma. Clearly, the Planck curve is only met for the largest optical depths, i.e. near the 13.5 nm emission feature, as expected given the large oscillator strengths near that wavelength. For any other wavelength, we may expect the plasma to emit significantly less radiation per unit area, in line with the results in Fig. 4.5(a). However, beyond ∼75 nm wavelength the Planck curve instead lies *below* the actual emission spectrum, as becomes clear from Fig. 4.5(b), which shows the same data as in panel (a) but for a larger wavelength range. As also mentioned in Chapter 3, the QE correction inserts an uncertainty in the final spectrum. More specifically in Fig. 3.6(a) of Chapter 3, we notice a strong dip in the QE around ∼100 nm. This dip translates to a large intensity correction with a systematic uncertainty associated with it, given that the available QE correction curves show a significant spread in this wavelength range (see Chapter 3). However, if we accept that indeed the available QE curves represent the detector response to reasonable accuracy, then an explanation for this effect could be that radiation in the VUV*

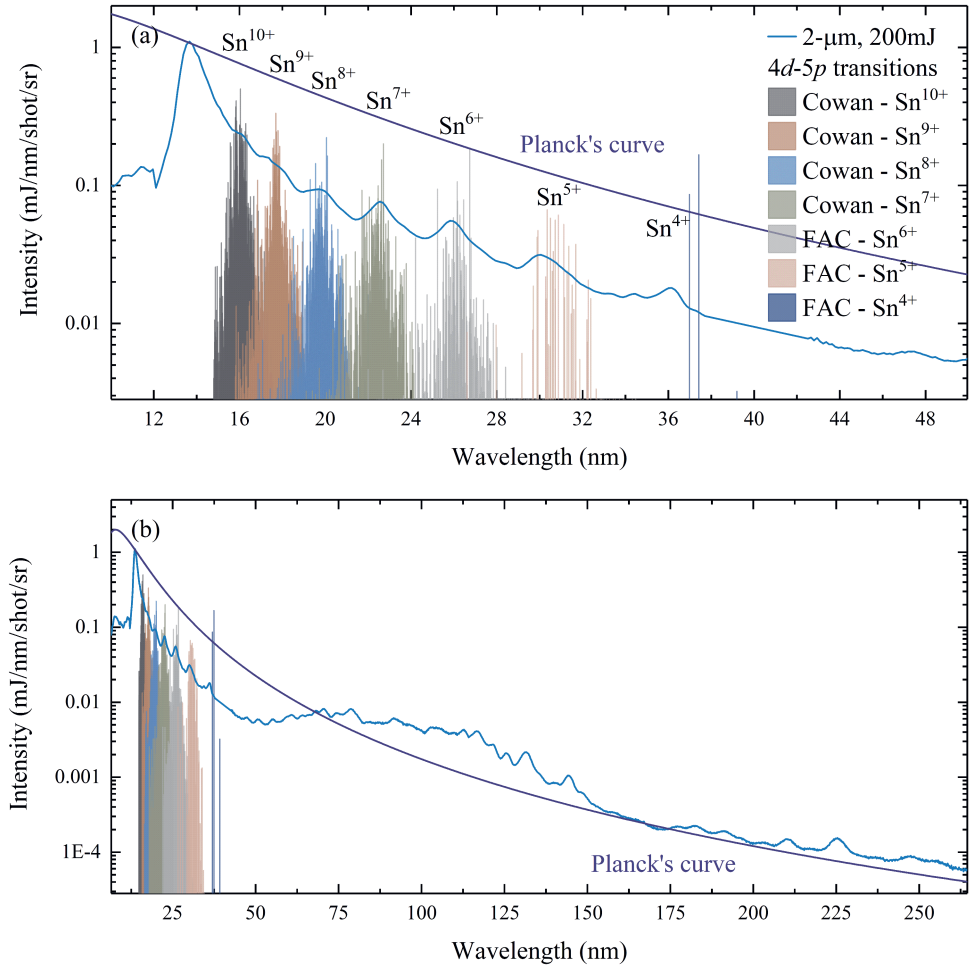

Figure 4.5: (a) Normalized concatenated emission spectra of a 2-µm LPP at 200 mJ laser pulse energy. The spectrum is corrected for exposure time, background, filter efficiency, and 1^{st} grating efficiency. Cowan and FAC calculation results for the $4d$–$5p$ transitions in Sn^{4+}–Sn^{10+} are also presented as individual vertical lines, which were scaled (individually per charge state) in amplitude for improved visibility. The dark purple curve represents Planck's curve. (b) Same spectrum as in (a) but with an extended wavelength axis.

and DUV* ranges are produced from a larger emitter, thus yielding higher intensity light as recorded on the detector. We thus tentatively find evidence that the emitter, "source" size increases in step with the emitted wavelength. To study this further, spectrally resolved imaging of the tin laser-produced plasma would be very benefi-

cial and would enable unambiguously establishing the source size as a function of wavelength.

4.4 Conclusions

We presented a calibrated spectrum in the 6.5–264.5 nm range from a microdroplet-tin plasma produced using a novel master oscillator power amplifier (MOPA) system delivering ns-pulsed 2-µm-wavelength laser light. The plasma emission spectrum was obtained from a transmission grating spectrometer by concatenating spectra as obtained from a series of filters, allowing avoiding higher diffraction orders. A comparison between spectra at various MOPA laser pulse energies was made, and we observed that in all cases the dominant radiative contribution comes from the EUV range (5–70 nm). A relatively broad range of laser pulse energies (100–250 mJ) was found to efficiently produce radiation in a 13.2–13.8 nm wavelength band that is useful for applications in EUV nanolithography. Spectra from over- and underheated plasma were also presented. The further comparison with a spectrum obtained from plasma driven by a 1-µm-wavelength drive laser reaffirmed the larger efficiency of the 2-µm laser for producing useful EUV radiation. The shorter 1-µm wavelength laser light was found to mostly produce more light in the 5–70 nm range, at the expense of emission in the useful 13.2–13.8 nm wavelength band. It was found that the spectra more closely resemble each other for larger wavelengths beyond the EUV range. We next identified key emission features in the ∼15–37 nm wavelength band using available Cowan code results combined with new FAC calculations, and found that $4d$–$5p$ transitions in multiply charged Sn^{4+}–Sn^{10+} ions dominate the emission. Upon comparing the emissivity with Planck's curve for thermal emission, we found evidence for an increasing plasma emission size with increasing wavelength in the range beyond ∼75 nm. This finding calls for further investigations using spectrally resolved imaging over a broad wavelength range.

4.5 Acknowledgments

This work has been carried out at the Advanced Research Center for Nanolithography (ARCNL). ARCNL is a public-private partnership with founding partners UvA, VU, NWO-I and ASML, and associate partner RUG. The transmission grating spectrometer was developed in the Industrial Focus Group XUV Optics at the University of Twente and supported by the FOM Valorisation Prize 2011 awarded to F. Bijkerk and NanoNextNL Valorization Grant awarded to M. Bayraktar in 2015. This project is funded by TKI-HTSM with the project name "Spectral Unraveling of EUV Lithography Light Sources (SUN)". This project received further funding from the Euro-

pean Research Council Starting Grant No. 802648 and is part of the VIDI research program with Project No. 15697, which is financed by NWO. The authors would like to thank Joris Scheers, James Byers, and Randy Meijer for their valuable contributions to this work.

Chapter 5

Broadband EUV–VUV–DUV imaging spectrometer comprising a zone plate dispersion-matched to a transmission grating

Y. Mostafa[1], Z. Bouza, J. Babenko, J. Byers, W. Ubachs, O. O. Versolato, and M. Bayraktar.

Abstract

We present an imaging spectrometer comprising a transmission grating and a zone plate, tapered to match the grating dispersion, for the achromatic one-dimensional imaging of plasma light sources in the extreme, vacuum, and deep ultraviolet (EUV, VUV, and DUV) regimes. The design of the imaging spectrometer and the (nano)fabrication process is detailed. First experimental results of imaging a laser-produced tin plasma in the 5–75 nm range are presented and compared to numerical simulations of the imaging spectrometer's diffracting elements. The effective plasma size obtained from the imaging is shown to increase with emission wavelength.

[1]The authors Y. Mostafa and Z. Bouza contributed equally to this work

5.1 Introduction

The reliability, throughput, and efficiency of EUV lithography machines is dependent on the characteristics of the EUV light source, which is currently a laser-produced plasma (LPP) generated from microdroplets of tin [4, 9, 10, 5, 6, 7, 8]. This LPP emits light from the soft x-ray to the visible region, with its emission maximizing in the 13.5 nm $\pm$ 1% "in-band" region where multilayer optic elements can be employed to guide the light. For applications, it is beneficial to maximize in-band emission compared to out-of-band emission [19, 20, 18, 23, 21, 22, 25, 24, 26, 27]. Out-of-band (OoB) EUV light cannot be used by narrow bandwidth multilayer mirror (MLM) optical systems employed in EUV lithography, but it can contribute to collector mirror heating and ionization of ambient hydrogen stopping gas which can damage the optics [32, 100]. Longer wavelength emission can also be reflected through the MLM optical system and expose the wafer, reducing the pattern resolution [50, 51]. For these and other reasons, it is critical to investigate the total conversion efficiency (CE) of the system into the in-band region and understand the emission in the unwanted OoB regions.

Two fundamental techniques for characterizing EUV plasma sources are spectroscopy and imaging. The spectrum of a microdroplet-tin LPP in a 5.5–265.5 nm wavelength range was recently obtained [100]. Such full-band spectroscopy provides important insights on the relative intensities and origins of the various emission features. However, the emission spectrum represents the average across the entire spatial distribution of the plasma and it is not possible to unravel which regions of the plasma contribute to which ranges of the emission spectrum. The plasma is highly inhomogeneous in terms of its density and temperature, and different regions are in fact expected to produce different emission spectra. Spatial information on the emission can be obtained using pinhole imaging in tandem with spectral filters but such solutions typically have poor resolution both in the spatial and wavelength domains. More generally speaking, established imaging techniques are restricted to either very broad wavelengths (e.g., pinhole imaging combined with a metallic filter) or very narrow bandwidths (e.g., imaging using MLM reflective optics). Fresnel zone plate (ZP) diffractive lens optics provide an alternative method of focusing EUV-DUV light that is absorbed in all materials from which refractive optic lenses can be manufactured [38, 39, 40]. Amplitude ZPs can be accurately fabricated using nanofabrication techniques, and can be designed to operate as high-resolution focusing lenses for any arbitrary wavelength of light in the soft-x-ray to DUV region [39, 106, 107]. The relatively poor transmission of a ZP is typically not a problem in the present application given the high intensity of the emitted radiation. However, ZPs are chromatic, focusing only a single wavelength, which has to be taken into

account in the design of a diffractive imaging system [40, 106].

In this paper, we propose and demonstrate the design of a diffractive imaging spectrometer that uses a transmission grating in tandem with a one-dimensional zone plate that is tapered to carefully match the grating's dispersion. The imaging spectrometer is designed for achromatic one-dimensional imaging of plasma light sources in the extreme, vacuum, and deep ultraviolet (EUV, VUV and DUV) regimes. First, the design of the imaging spectrometer and the (nano)fabrication process of the ZP is detailed. Next, first experimental results of imaging a laser-produced tin plasma in the 5–75 nm range are presented and compared to numerical simulations of the imaging spectrometer's diffracting elements. Independent verification experiments of the image size and optical alignment are additionally performed. Lastly, the effective plasma size is obtained from the imaging and is shown to increase with emission wavelength.

5.2 Design of the imaging spectrometer

A schematic of the optics arrangement of the proposed imaging spectrometer is shown in Fig. 5.1. The top-down view in Fig. 5.1(a) shows the dispersion plane where the incoming light is separated into different wavelengths by the grating and detected on a charge-coupled device (CCD) camera of 2048×512 pixels. The Fresnel zones of the ZP are orthogonal to the dispersion plane, so that the measured spectrum is not influenced by the ZP. In practice, as will be explained in the fabrication Section 5.2.3, there are periodic support bars to keep the integrity of the free-standing absorber bars of the ZP. However, the width of these support bars is chosen to be small compared to the width of the ZP, and the period of these support bars is chosen to be much larger than the period of the grating. Therefore their contributions can be neglected for the spectral analysis. The side-on view in Fig. 5.1(b) shows the imaging axis of the imaging spectrometer. The incoming light passes unhindered through the grating (diffraction due to the support bars of the grating is negligible) and is focused by the zone plate in a point-to-point imaging configuration.

The focusing property of a ZP for performing imaging is simulated in Section 5.2.2. In this simulation a plane wave at 13.5 nm wavelength has been propagated through 15 Fresnel zones with dimensions chosen to form a focus at a distance 0.5 m away from the ZP. As can be seen in Fig. 5.2, a sharp focus forms as a result of interference of waves from different zones. Such a simulation demonstrates the working of the imaging spectrometer for a single wavelength. In the following, we will model how to design a ZP to match the dispersion of a grating over a broad wavelength range from 5 to 75 nm.

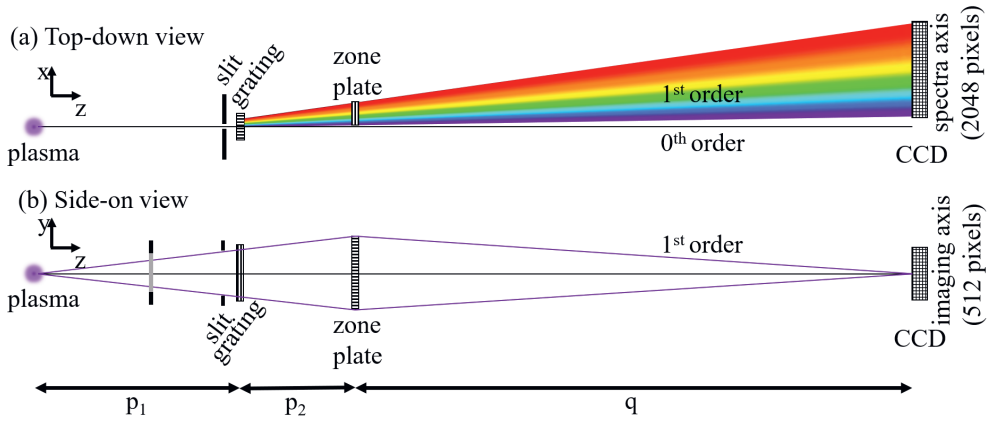

Figure 5.1: Top-down (a) and side-on (b) view schematics of the imaging spectrometer setup. (a) Top-down view shows how plasma generated light enters the spectrometer from the left, passes through the different elements and then diffracts along the horizontal plane. (b) Side-on view shows how in this orientation plasma light is simply imaged using the ZP in a point-to-point imaging configuration.

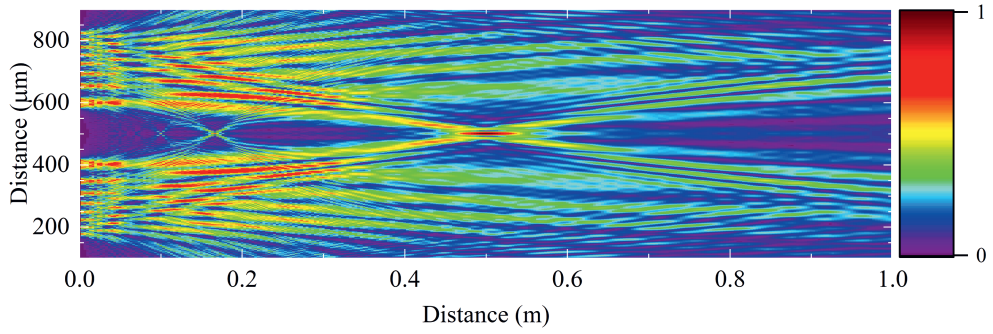

Figure 5.2: Propagation of a plane wave passing through 15 Fresnel zones (simulated). The dimensions of the zones are chosen to form a focus 0.5 m away from the ZP (see main text).

5.2.1 Grating and zone plate theory

A schematic of a one-dimensional ZP that works for a single wavelength is shown in Fig. 5.3(a). In this figure, $r_{i,j}$ (here $i = 1$) denotes the Fresnel zone radius of the i^{th} wavelength and j^{th} Fresnel zone. The Fresnel zone radius is set by the focal length and wavelength of the incident light. Therefore, for a multiwavelength ZP matched to a grating, the focal length is fixed by the experimental setup but the incident wavelength changes at different positions of the ZP. In Fig. 5.3(b), a multi-

wavelength ZP is shown, apt for an increasing wavelength from left-to-right, and as a consequence also the Fresnel zone radii. Such an increase in the zone radii, shows itself as tapering of the designed ZPs. For an ideal multi-wavelength ZP, a continuous taper is expected. On the other hand, in the fabrication of ZPs, the structures are made in discrete steps, as schematically shown in Fig. 5.3(b). In the following, it will be shown that these discrete steps are chosen to be small enough to not significantly negatively impact the operation of the ZP, since the width of each discrete step w_i will be matched to the spectral resolution imposed by the grating.

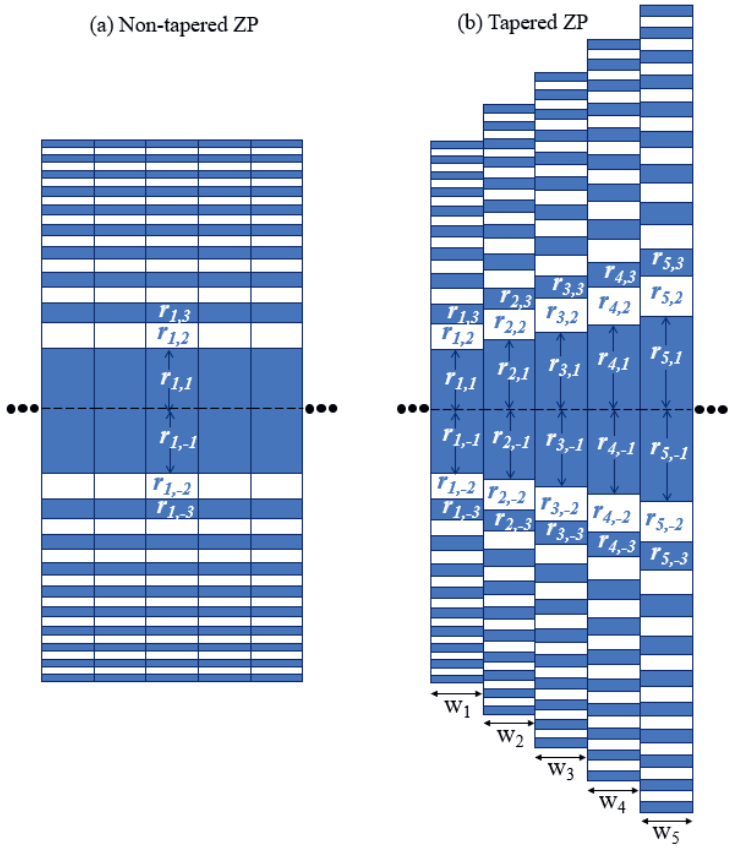

Figure 5.3: Schematic of different types of ZPs. (a) Non-tapered one-dimensional ZP. This type of ZP is used to focus a single wavelength. (b) Tapered ZP. This type of ZP is used to focus a range of wavelengths.

In designing a ZP that is matched to the dispersion of a grating, there are two aspects of the grating to be considered. First aspect is the angular dispersion and second

aspect is the spectral resolution. The wavelength that is diffracted to a specific angle can be calculated using the grating equation.

$$m\lambda = d\sin(\theta) \tag{5.1}$$

where m, d and θ are respectively denoting the diffraction order number, grating period and diffraction angle in normal incidence configuration. The spectral resolution that can be achieved with a transmission grating consists of a dispersion and geometric component, and the total resolution can be written as:

$$\Delta\lambda = \sqrt{\Delta\lambda_{dis}^2 + \Delta\lambda_{geo}^2} \tag{5.2}$$

where $\Delta\lambda_{dis}$ and $\Delta\lambda_{geo}$ are, respectively, the dispersive and geometric resolution terms. Following Ref. [62],

$$\Delta\lambda_{dis} = \frac{d}{m}\left(\frac{\lambda}{w_{slit}}\right) \tag{5.3}$$

where w_{slit} is the width of the slit. The dispersive resolution is determined by the grating period and the width of the slit, and is independent of the distance from the grating. However, the geometric resolution depends on the distance to the grating. The geometric resolution on the ZP plane can be calculated as:

$$\Delta\lambda_{geo} = \frac{d}{m}\left(\frac{\Delta S + w_{slit}}{p_1}\right) + \frac{d}{m}\left(\frac{K}{p_1 + p_2}\right) \tag{5.4}$$

where p_1 and p_2 are the plasma-grating and grating-ZP distances as shown in Fig. 5.1. ΔS is the estimated plasma size and K is the full-width-at-half-maximum of the convolution of w_{slit} across a pixel width w_{pixel}, i.e. $K = \sqrt{{w_{slit}}^2 + w_{pixel}^2}$ [62]. Now, with the position of wavelength and spectral resolution of the ZP calculated using Eq. 5.1 and Eq. 5.2, it is possible to calculate the zone radii of the ZP and the maximum achievable spatial resolution.

In the point-to-point imaging configuration of a ZP, the focal length f can be defined using the lens makers formula in the thin lens approximation regime as:

$$f = \left[\frac{1}{p_1 + p_2} + \left(\frac{1}{q}\right)\right]^{-1} \tag{5.5}$$

where q is the distance from the ZP to the CCD (see Fig. 5.1). The radius of the N^{th} zone r_N is given by the equation:

$$r_N = \sqrt{N\lambda\left(f + \frac{N\lambda}{4}\right)}. \tag{5.6}$$

The spatial resolution Δw of a ZP with N zones is given by [40]:

$$\Delta w = \frac{\lambda}{f}\left(\frac{2}{r_N}\right). \tag{5.7}$$

With a perfectly monochromatic light source, the spatial resolution is limited by the numerical aperture (NA) of the ZP, and therefore by the maximum number of zones. However, real sources, such as our plasma source, are broadband one but after the emitted light passes through the transmission grating it can then be approximated as quasimonochromatic with an associated bandwidth $\Delta\lambda$. Since zone plates are based on diffraction, system performance is sensitive to source bandwidth. Any deviation from the design wavelength of the ZP causes defocusing and worsening of the spatial resolution. In order to maintain near diffraction-limited performance, the magnitude of the focus shift Δf due to $\Delta\lambda$ should be less than the depth of focus (DOF) of the system. This sets a limit on the useful number of zones (N_{max}) of the ZP given by the following equation:

$$N_{max} \leq \frac{\lambda}{\Delta\lambda} \tag{5.8}$$

Any number of zones beyond N_{max} do not contribute to the improvement of the spatial resolution. The magnification M of the system can easily be calculated by $M = q/(p_1 + p_2)$.

5.2.2 Simulation of zone plate wave propagation

Considering the complicated design of the aforementioned zone plates, numerical simulations of free space propagation are implemented. Such implementation will aid in understanding the response, resolution and limitations of the designed devices.

The basis of the numerical simulations follows the work of Matsushima and Shimobaba [108] on band-limited angular spectrum method simulations. Employing such simulations allows for the calculation of the free-space propagation of light, which will be utilized to predict the diffraction of incident light on zone plates. Here, a summary of the mathematical description is provided followed by the implementation of the numerical method to simulate the zone plate response. Finally, limitations of the method and the chosen parameters are discussed.

In the simulations utilized in this chapter, we consider the propagation of a monochromatic planar source field at $z = 0$. The simulations aim to calculate the intensity of the propagated wave at any defined distance z_0 along the propagation path of the

initial plane wave. The intensity distribution in the x-y plane is calculated according to the following mathematical construction.

According to the Rayleigh-Sommerfeld formula for a monochromatic source field $g(x, y, z)$ at $z = 0$ [109], the field at a distance z_0 is calculated as

$$g(x, y, z_0) = \int\int g(x', y', 0) \frac{e^{i2\pi r' \lambda^{-1}}}{r'} \frac{z_0}{r'} \left(\frac{1}{2\pi r'} + \frac{1}{i\lambda} \right) dx' dy' \tag{5.9}$$

where $r' = \sqrt{(x - x')^2 + (y - y')^2 + z_0^2}$. The corresponding solution can be rewritten as a two-dimensional convolution of the input field $g(x, y, 0)$ and a propagation function $h(x, y, z)$ defined as

$$h(x, y, z) = \frac{e^{i2\pi r \lambda^{-1}}}{r} \frac{z}{r} \left(\frac{1}{2\pi r} + \frac{1}{i\lambda} \right) \tag{5.10}$$

Following the work of Matsushima and Shimobaba [108], we assume circular symmetry of the transfer function and additionally impose a band limit, which truncates the contribution of large (Fourier) frequencies in order to reduce sampling limitations. With such frequency band limit, the numerical errors in long distance calculations of propagating light are reduced. Without such a band limit, the whole electromagnetic field propagation would need to be calculated, which presents a large computational barrier. This band limit manifests itself as the multiplication of a circular Heaviside function W in the frequency domain. Such circular band limit reduces aliasing errors and high frequency noise in long distance propagation simulations. We then arrive at the final solution for the field intensity.

$$g(x, y, z_0) = \mathcal{F}^{-1}\{U \circ H \circ W\} \tag{5.11}$$

with $\circ$ representing the Hadamard product, and

$$U = \mathcal{F}\{g(x, y, 0)\} \tag{5.12}$$

and

$$H = \mathcal{F}\{h(x, y, z_0)\}, \tag{5.13}$$

where $\mathcal{F}\{\}$ denotes the 2-dimensional Fourier transformation and $\mathcal{F}^{-1}\{\}$ is the inverse transformation. As is the advantage of the angular spectrum method, the field propagation calculation is reduced to only two Fourier transformations. This allows for a quick yet accurate simulation of the propagation of a pre-defined input field.

In Section 5.3.2, we utilize the propagation calculations described above to find the intensity distribution at focal distance. Such calculations assume a plane wave input field through the zone plate which in imaging applications may not hold fully. They will, however, provide insight into the spectral and imaging capabilities of our setup of a point source at -∞ along the z-direction.

5.2.3 Zone plate fabrication process

The free-standing ZPs are fabricated following the process steps presented in Fig. 5.4. The fabrication process starts with a 400 µm thick double-sided polished Si wafer which is coated on both sides with a Si_3N_4 layer of 200 nm thickness by means of plasma-enhanced chemical vapor deposition (PECVD). After that, a 200 nm lift-off resist (LOR), also known as transfer layer, is spin-coated at 3000 rpm and then baked for 5 minutes at $190\,^{\circ}\mathrm{C}$ on a hot plate. Then a 1200 nm positive optical resist is applied with the same technique but different parameters (at 4000 rpm, $90\,^{\circ}\mathrm{C}$ for 1 minute). To define the high-resolution ZP patterns we use the optical lithography technique. For the current fabrication, a 120 $\mathrm{mJ/cm^2}$ UV dose was chosen. The UV light interacts and degrades only the regions of the optical resist that are allowed by the in-use mask. As a next step, a solvent, also called developer, dissolves away the parts that were exposed to UV light, leaving behind a coating where the mask was placed. In that way the mask imprints its information onto the resist. Additionally, the optical resist is etched vertically. Then the metalization procedure follows. A 200 nm XUV absorber layer of Au (deposition rate = 0.25 nm/min) followed by a 15 nm etch mask layer of Cr are deposited by metal evaporation using an electron beam deposition tool. After that, the lift-off process is carried out by dipping the sample in an acetone bath with ultrasonic vibrations for 15 minutes to form the top absorber layer and the etch mask for patterning the Si_3N_4 layer.

At the back of the wafer, an optical resist is applied and its openings are defined by optical lithography using 4 cm $\times$ 2 cm open windows. The optical lithography is followed by fluorine-based reactive ion etching (RIE) of the Si_3N_4 layer on the backside and an asymmetric wet etch process of 2 days in tetramethyl ammonium hydroxide (TMAH) removing the bulk silicon and stopping on the top Si_3N_4 layer. The final step of the fabrication process is the dry etching of the Si_3N_4 layer from the front side, using the Cr layer as a mask. More information about the fabrication process can be found in other works [62, 63].

In order to keep the integrity of the free-standing absorber bars, periodic support bars orthogonal to the absorber bars are included in the design of the ZPs. The width of the support bars are $4\,\mu\mathrm{m}$ with a period of $40\,\mu\mathrm{m}$ which are determined based on separately fabricated test structures. The support bar period is also used as the width of each wavelength step (w_i in Fig. 5.3). The period of these support bars is also chosen to be much larger than the period of the gratings ($1.3\,\mu\mathrm{m}$). Therefore, the effect of the support bars can be neglected for the spectral analysis.

The optical microscopy images of the fabricated non-tapered and tapered ZPs are shown in Fig. 5.5(a) and (b), respectively. Fresnel zones in the horizontal direction and support bars in the vertical direction are visible in both ZPs.

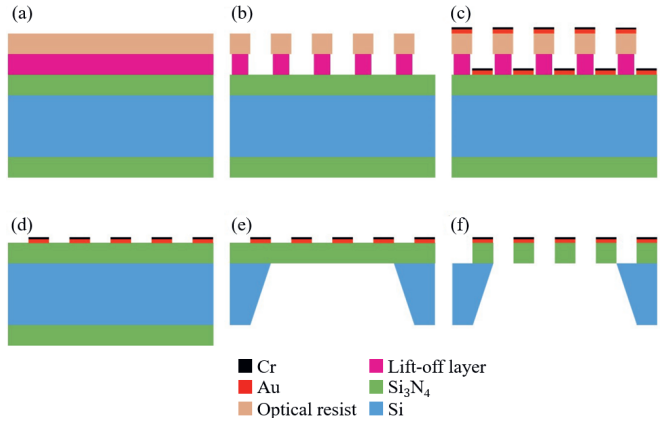

Figure 5.4: Fabrication process for the free-standing ZPs. (a) Si_3N_4 is deposited using PECVD on both sides of a $500\,\mu m$ thick (100) orientation wafer, followed by spinning a lift-off-resist (LOR) layer and a positive optical resist layer. (b) The patterns of ZP zone bars are exposed on positive resist and developed. The LOR has a faster etch rate in the developer than the optical resist causing the LOR to under-etch. (c) $200\,nm$ Au and $15\,nm$ Cr is deposited using evaporation. (d) Lift-off of LOR, optical resist and the metal layers they were supporting. (e) Si_3N_4 on the backside of the wafer removed using dry etching and Si handle layer etched in TMAH. Si_3N_4 acts as a TMAH stopping layer. (f) Exposed Si_3N_4 etched from the front using dry etching, using the Cr layer as a hard mask, suspending the ZP zone bars.

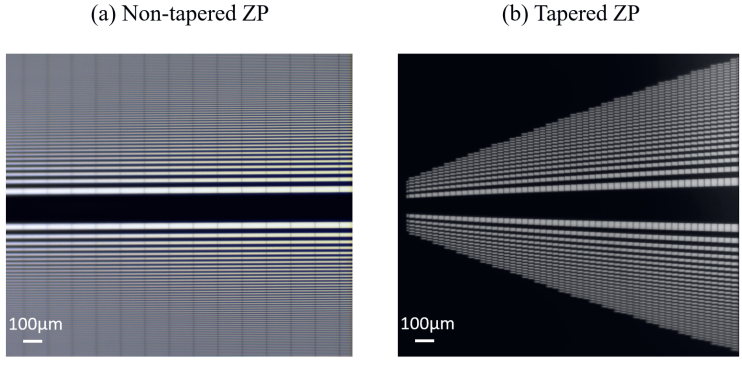

Figure 5.5: Optical microscopy images of ZPs. (a) Non-tapered ZP. (b) Tapered ZP.

5.3 Experiment

In this section, we first present the LPP light source and parameters of the imaging spectrometer. Second, we present the imaging results with the ZPs, their comparison with the simulations, and independent verification of the alignment of the ZP.

5.3.1 Experimental setup

An 1 mm thick planar solid polycrystalline Sn target is mounted onto a 2D-translation stage in a vacuum vessel of pressure of 10^{-6} mbar. This solid target is irradiated by a 10-Hz Nd:YAG laser system (λ=1.06 µm) of 6 ns pulse duration and a variable (∼60–120µm) full width at half maximum (FWHM) spot size at the planar target surface depending on the needs of the measurements. The translation stage enables a step-wise motion of the target to guarantee a fresh target spot after each series of ten pulses. Additional details on the experimental setup based on solid planar targets can be found in other works [13, 74].

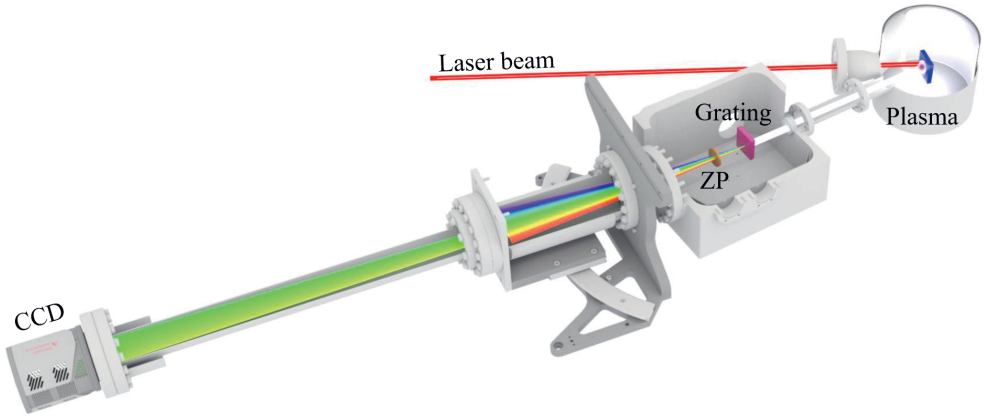

Figure 5.6: Three-dimensional rendering of the laser-produced plasma source and imaging spectrometer experimental setups. The imaging spectrometer is placed head on to the plasma and under an angle of 30° with respect to the propagation direction of the laser light. The imaging spectrometer components grating and ZP are contained in a differentially-pumped chamber followed by a bellows assembly and a long tube carrying a CCD camera.

The spectral emission measurements and the plasma images are obtained by the imaging spectrometer at an angle normal to the target surface but 30° with respect to the direction of propagation of the laser light. A 3D drawing of the experimental setup is shown in Fig. 5.6. The imaging spectrometer is composed of a slit (not shown in Fig. 5.6 for brevity), a grating, a ZP followed by a bellows assembly, a long tube, and finally a CCD. The bellows assembly enables positioning the CCD at different angles to capture different wavelength ranges.

The parameters of the imaging spectrometer in this experimental implementation are primarily imposed by practical conditions, such as available vacuum chambers and space. A summary of the parameters is listed in Table 5.1. We set the source-to-grating distance (p_1) at the minimum possible value determined by the size of the

Table 5.1: Parameters used in the implementation of the imaging spectrometer using a 780 l/mm grating and matched 780-ZP.

Parameter	Value	Explanation
p_1	$53\,\mathrm{cm}$	Source to grating distance
p_2	$5\,\mathrm{cm}$	Grating to zone plate distance
q	$110\,\mathrm{cm}$	Zone plate to CCD distance
M	1.89	Magnification
m	1	Grating diffraction order
d	$1.3\,\mu\mathrm{m}$	Grating period
w_{slit}	$150\,\mu\mathrm{m}$	Slit width
ΔS	$100\,\mu\mathrm{m}$	Estimated source size
w_{pixel}	$13.5\,\mu\mathrm{m}$	Pixel width
$\Delta\lambda$	$0.8\,\mathrm{nm}$	Spectral resolution
Δw	$10\,\mu\mathrm{m}$	Spatial resolution

plasma chamber. The chamber containing the grating and ZP is a modified version of an available transmission grating spectrometer [63]. The grating to ZP distance (p_2) is mainly determined by the maximum available space in this spectrometer chamber. Finally, the ZP to CCD distance (q) is chosen as the maximum distance available on the used optical table, in order to maximize the magnification. We have chosen a 780 lines/mm ($1.3\,\mu\mathrm{m}$ period) grating that enables capturing the zero-order of the grating and the wavelengths till 26 nm in a single CCD image, which is helpful in aligning and identifying the dominant $13.5\,\mathrm{nm}$ emission peak. The slit width (w_{slit}) is chosen to maximize the spectral resolution at the ZP position. The source size (ΔS), which is needed in calculating the spectral resolution, is estimated to be around $100\,\mu\mathrm{m}$, of the order of the laser spot size in the EUV regime (also see [15]).

Based on the parameters of the imaging spectrometer, ZPs for several grating types and spectral ranges have been fabricated. For the experiments in this chapter, two types of ZPs have been used. The first ZP type has zone widths and taper matching the 780 lines/mm grating in the 5–80 mn range. In order to independently verify that the image resolution is not compromised by the spectral resolution or misalignment of the first ZP type, a second type of ZP is used that is designed for much higher grating line density. Specifically, a ZP type that is matched to a $10\,000\,\mathrm{lines/mm}$ in the 7-17 nm range is used. We respectively denote these two ZP types as 780-ZP and 10k-ZP in the following.

The diffracted light from the grating and ZP is recorded on a back-illuminated CCD from Greateyes (GE2048 512BI UV1), cooled to -20°C to reduce thermal noise. The exposure time ranges typically between approximately 1–120 seconds depending on

the wavelength range. Background frames were recorded for the same exposure time as in the measurements with Sn plasma, and these images were then subtracted from the recorded plasma emission to eliminate the read-out noise and dark counts. The resulting CCD images are cropped and corrected for rotation introduced by a slight misalignment of the slit with respect to grating/ZP and the CCD pixel array. The calibration of the wavelength x-axis is performed using the geometrical parameters of the experimental setup following Eq. 5.1.

5.3.2 Experimental results

In this section we show and discuss our experimental results using two different ZPs in tandem with a 780 lines/mm grating. First, we use a tapered zone plate (780-ZP) matched to the grating. Second, we validate the alignment of the imaging spectrometer using the 10k-ZP, which will produce an image at a single wavelength depending on its x-position. We focus on a qualitative analysis of the obtained CCD images. The experimental results will be used in next Section 5.4 to quantitatively assess the emission area as a function of wavelength.

Fig. 5.7 presents a CCD image without using a zone plate. The plasma light in this case passes only through the (150 µm) slit and the (780 lines/mm) transmission grating (see Fig. 5.6) enabling the measurement of the tin LPP emission spectrum. In this CCD image the strong emission near 13.5 nm wavelength is immediately apparent. Resolved, weaker emission features near, for example, 6, 22, and 25.5 nm can readily be assigned to the specific charge states of Sn ions, see Chapter 2 of this Thesis. A further strong emission feature near 0 nm is due to undiffracted, zero-order light passing through the grating.

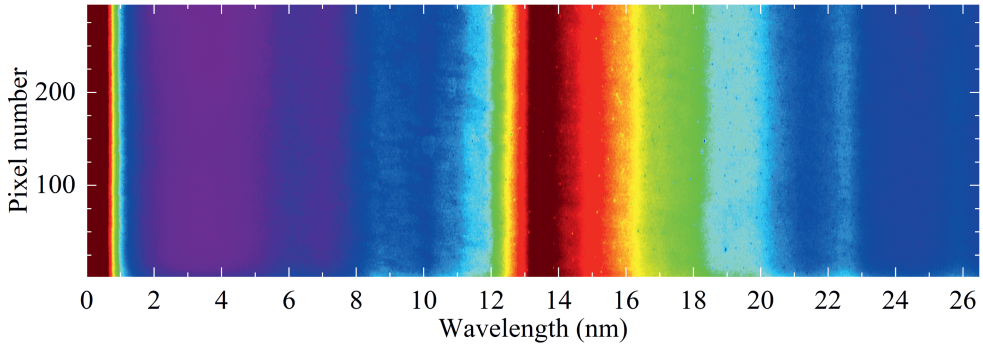

Figure 5.7: Spectrum of the tin LPP recorded by taking the ZP out of the beam path.

Tapered zone plate matched to 780 lines/mm grating

First, we use the 780-ZP matched to a 780 lines/mm transmission grating. This 780-ZP is designed to image at wavelengths between 5 and 80 nm. Given the dispersion of the 780 lines/mm transmission grating, the CCD will need to be moved in three angular steps (see experimental setup) to enable capturing this full range. The range of ∼0–24 nm can be measured when the CCD is placed under an angle of 0° with respect to zeroth diffraction order of the grating. (see Fig. 5.8 (a)). To measure a longer wavelength regime [∼24–47 nm - see Fig. 5.8 (b)] we put the CCD at an angle of 1°, maintaining a small overlap with the previous position for inspection purposes. For the even longer wavelength regime [∼47–68 nm - see Fig. 5.8 (c)] we move the CCD to an angle of 2°. Finally, for the last wavelength regime (∼68–80 nm) we move the CCD by another degree to 3°. The contribution from this last CCD position is shown in the 'stitched' CCD image [∼0–75 nm - see Fig. 5.8 (d)]. We ensure that when we move to the next CCD angle there is always an overlap wavelength region between the new image and the previous one. In that way, the different CCD images can reliably be 'stitched' together to create a full imaged spectrum from ∼8–75 nm (see Fig. 5.8(d)). We note that this composite range is somewhat smaller than the specified design range of 5–80 nm which we attribute to a minor change in the distance between the ZP and grating with respect to the original design. This minor change is however nearly fully compensated by a small lateral (x-axis) repositioning of the ZP as carefully verified in the experiments.

For the combined spectroscopic/imaging measurements of an LPP generated from a Sn target, shown in Fig. 5.8, a 40 mJ laser pulse with a FWHM spot size of 70 ± 7 µm was used. In more detail, Fig. 5.8(a) presents a CCD image taken under an angle of 0° covering the 0–24.7 nm wavelength regime. No emission below 5 nm can be expected given the short-wavelength cut-off of the 780-ZP used. The corresponding plasma image is found on the central line at a pixel number near ∼280. The time-integrated source size can next be extracted from the image as a function of emission wavelength (see next Section 5.4).

Fig. 5.8(b) shows a CCD image taken under an angle of 1° with respect to the zero-order light path in a wavelength regime of ∼24.7–47.2 nm. In this panel the 3rd diffraction order of the strong 13.5 nm emission peak at ∼40.5 nm [100] is particularly striking. The 3rd diffraction order is introduced from the in-use transmission grating [63, 62]. Such higher order contributions to the image plane may complicate image analysis. Therefore, given the strong emission near 13.5 nm, there are some wavelengths regimes that are particularly challenging to analyze, such as ∼(40.5 ± 5) nm (3rd diffraction order of the 13.5 nm) or ∼(67.5 ± 5) nm (5th diffraction order of the 13.5 nm).

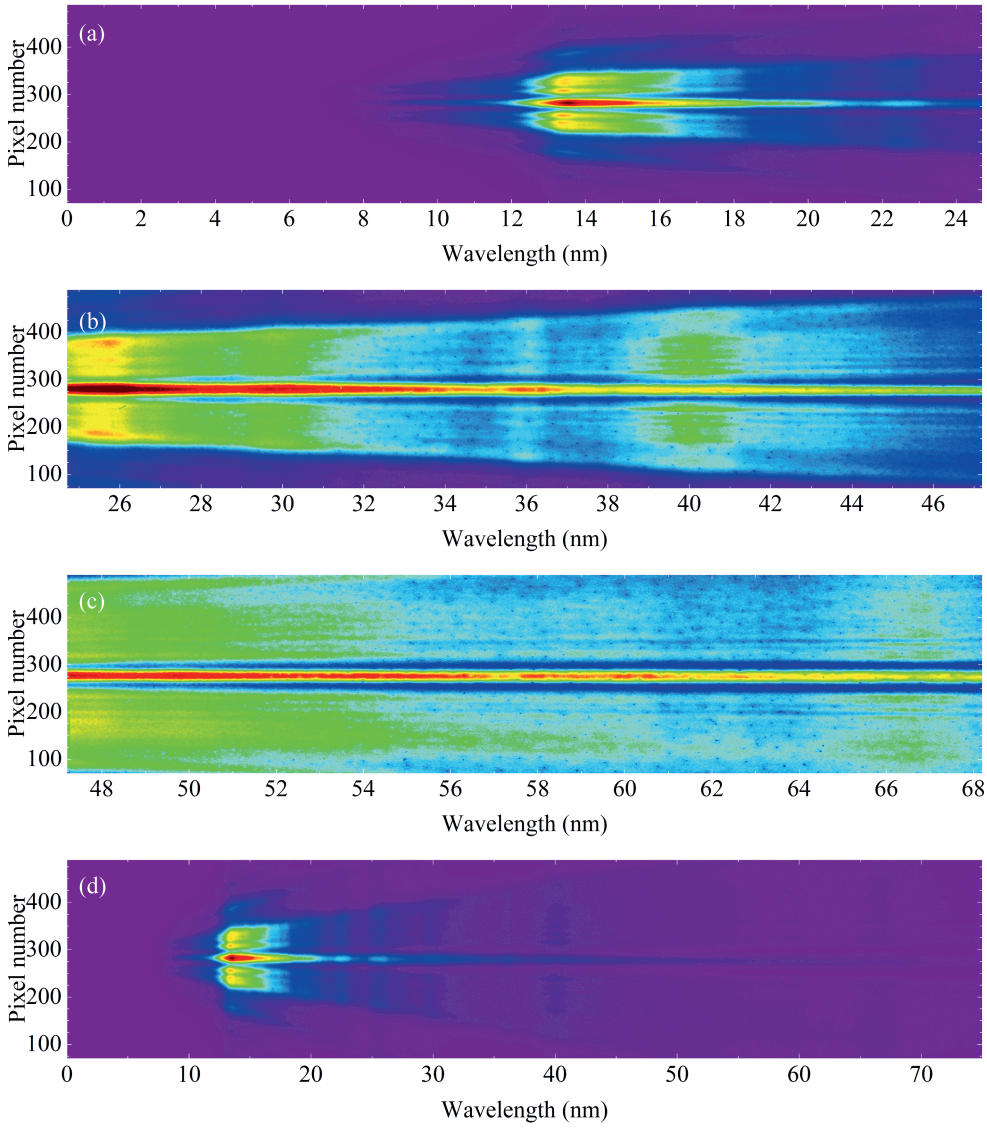

Figure 5.8: CCD images using a 780-ZP with 780 lines/mm transmission grating at bellow angles of (a) 0°, (b) 1° and (c) 2°. (d) Concatenation of the previous three images. Each panel is normalized to its maximum to maximize the visibility of features in each image.

Next, Fig. 5.8(c) shows a CCD image taken under an angle of 2° presenting a wavelength regime spanning ∼47.2–68.2 nm. A clear decrease of signal strength towards

the longer wavelengths is observed in line with the experiments reported in Chapter 3 and 4 in this Thesis. We note that Figs. 5.8(a–c) were individually normalized for optimum visibility of the emission features. Finally, Fig. 5.8(d) presents a concatenated CCD image in the wavelength regime of 0–75 nm. In this panel an extra CCD image taken under an angle of 3° (wavelength regime of ∼68.2–75 nm is included.

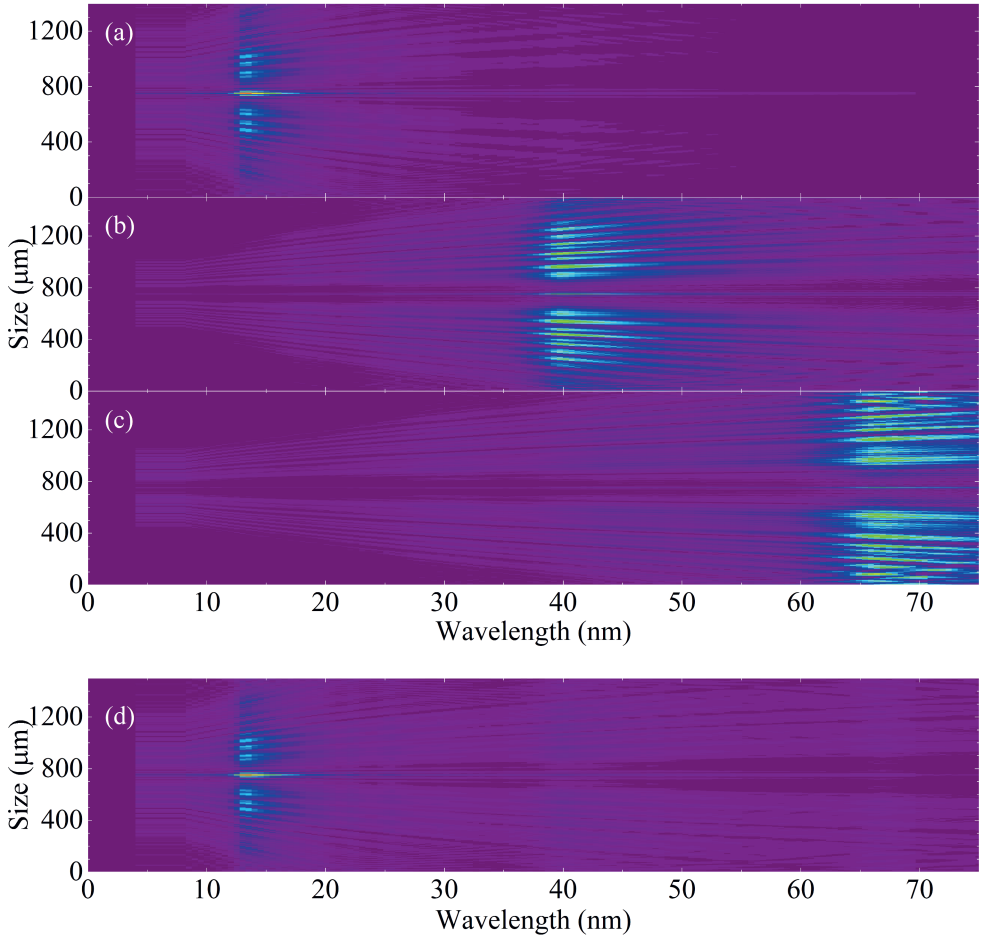

Figure 5.9: Simulations showing CCD images of diffraction grating orders (780 lines/mm) propagating through a tapered zone plate. Figure (a) shows the 1st order, (b) 3rd order and (c) 5th order. The CCD image intensities of the 3 orders are scaled by the inverse of the square of the order and the experimental spectral intensity. The summation is shown in (d) following the amplitude scaling as discussed in the main text.

The response of the tapered zone plate design is studied through the propagation

simulations described in Section 5.2.2. The result for diffracted light from a 780 lines/mm grating incident on a tapered zone plate for such a grating is shown in Fig. 5.9. The input planar waves are scaled by the experimentally measured intensities for each wavelength in the range 5-75 nm. The first-order diffraction from the grating is passed through the zone plate and the intensities at the focal point are calculated and shown in Fig. 5.9(a). Similarly, the 3rd and 5th orders are simulated and shown in Fig. 5.9(b) and Fig. 5.9(c) respectively. In order to be able to compare the simulations results with the experimentally measured images, each order's simulation results are scaled by the inverse of the square of the order number as in a scalar diffraction scenario which holds true in this case with short wavelengths ($<75\,\mathrm{nm}$) in comparison to the grating period ($1.3\,\mu\mathrm{m}$) ratio [110, 111, 62]. The scaled summation of the orders 1, 3 and 5 is shown in Fig. 5.9(d).

On comparison of Fig. 5.8 and 5.9, we find very similar responses, even though our comparison can only remain qualitative because the simulations are performed for plane waves (effectively object at infinity). In particular the feature near 40.5 nm wavelength appearing in Fig. 5.9(b) is instructive. It supports the hypothesis that this feature, observed in the experiments, is due to the diffractive focusing as well as the higher ZP diffraction orders, of a third-order grating diffraction of light near 13.5 nm wavelength. Contributions of the weaker fifth-order imaging of the dominant 13.5 nm feature are also visible in the experiments. We further note that the horizontal (wavelength) width of the feature at 13.5 nm appears to be narrower in the simulations than is found in the experiments. The opposite appears to be the case for the feature near 40.5 nm which extends over a larger wavelength range in the simulations. Further simulations of an emitting object of finite size are required to more quantitatively assess the response of the imaging spectrometer. However, the current good qualitative agreement supports our interpretations and allows for further analysis.

Verification of image size and alignment

The observed image size can be influenced by the spatial resolution and alignment of the spectrometer. One important contribution to the spatial resolution is the monochromaticity or spectral resolution of the incident light. If the spectral resolution of the incident light and the taper of the ZP is not matched, then the spatial resolution will be larger than the design parameters and thus the source size may be overestimated. This corresponds to chromatic aberrations in regular optical systems. The same overestimation may also occur if the grating and ZP are not well aligned with respect to each other. In order to verify that the spatial resolution and hence the image size is not compromised by these two factors, we performed a measurement with a ZP designed for a $10\,000\,\mathrm{lines/mm}$ grating in the 7-17 nm range. With this

10k-ZP, a specific wavelength becomes in focus only when the angle and position of the ZP matches the wavelength. In our experiments, we use this 10k-ZP with a 780 lines/mm grating and a 150 µm slit. The taper of this ZP is much less than the 780-ZP and requires a higher dispersion to image the full 7-17 nm wavelength band in one position. When used with a $780\,\mathrm{lines/mm}$ grating that has a much lower dispersion, the match between the grating dispersion and the taper of the ZP quickly degrades. Therefore, only a narrow wavelength band in the order of $1\,\mathrm{nm}$ moves into focus. Other wavelengths can be brought in to focus simply by moving the ZP in the x-direction.

Fig. 5.10 presents the images captured using the 10k-ZP at three different positions of the ZP along the x-axis. Specifically, the wavelengths in focus are 8.6 nm, 12.5 nm and 16.8 nm in Fig. 5.10(a)-(c), respectively. Here, a laser beam of 40 mJ with a FWHM of 70 $\pm$ 7 µm was used, same as in the measurements of Fig. 5.8. In all cases, we notice that the area around 13.5 nm is always brighter and this is due to the strong emission peak of the tin LPP at this wavelength. Similar verification experiments are repeated for several wavelengths. The images sizes calculated from the verification experiments are compared to previous image sizes in the next section.

5.4 Discussion: Plasma size

The captured CCD images are analyzed to extract the time-integrated effective size of the emission area at different wavelengths. Thus, a wavelength dependent source size is obtained. We extract the wavelength-dependent size by means of Gaussian fits to vertical lineouts of the CCD images. Investigating the vertical lineout on the CCD provides the plane of the source as imaged by the zone plate.

As discussed and shown in earlier simulations (Fig. 5.9), the image plane not only contains the image of the plasma, but also other overlapping diffraction orders resulting from the grating and the zone plate. The zeroth and higher orders may, depending on wavelength and diffraction efficiency, negatively impact our ability to assess the source size from the first order. We therefore restrict our analysis to a smaller wavelength regime, where no odd higher diffraction orders of the intense 13.5 nm peak are present, well below 40.5 nm where the strong third-order contribution would dominate. Since at slightly lower wavelength we still have a considerable third order contribution, we restrict the wavelength range for source size investigations to the 8-35 nm regime.

We find that a procedure using a three-Gaussian fit to the center diffraction feature yields robust results. This procedure is based on the observations of the simulations as in Fig. 5.9. The central peak in the image plane corresponds to the image of the

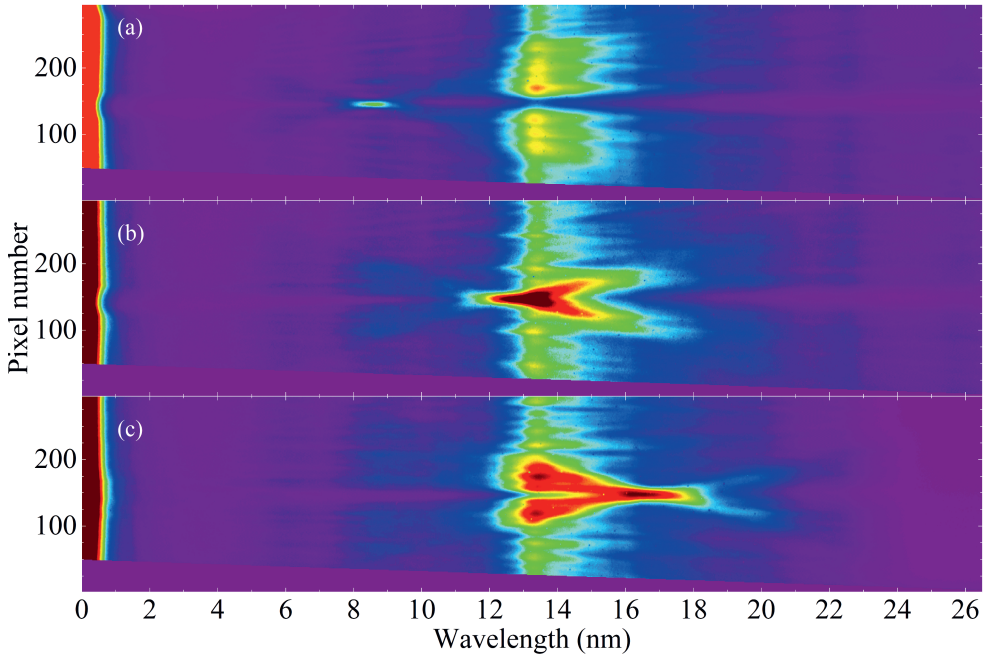

Figure 5.10: CCD images using a 10k-ZP combined with a 780 lines/mm grating at three different positions of the ZP bringing in focus the wavelengths (a) $8.6\,\mathrm{nm}$, (b) $12.5\,\mathrm{nm}$ and (c) $16.8\,\mathrm{nm}$.

source itself, while the two adjacent peaks represent contributions from higher order zone plate diffraction. This fitting procedure is then applied to the vertical lineouts of the CCD image at various wavelengths. The Gaussian fits yield the position and the (FWHM) size of the source. The calculation of FWHM size in μm is based on the estimated magnification ($\sim$1.8) of the system and the known pixel size of 13.5 μm. The resulting source size dependence on the wavelength is shown in Fig. 5.11 for a limited wavelength range of 8–20 nm.

The choice of Gaussian fits is based on the experimental parameters of the studied system. We illuminate the tin target with a laser beam with a Gaussian spatial profile. It is expected that the plasma expansion results in a time integrated source with a Gaussian profile. Through the fits in all the subsequently presented images, we observe always a normal distribution of the source emission. The asymmetry of the source image has been estimated through the skewness of the Gaussian fits to be much smaller than pixel sizes. Consequently, in all the presented fits, the skewness of the Gaussian is not considered.

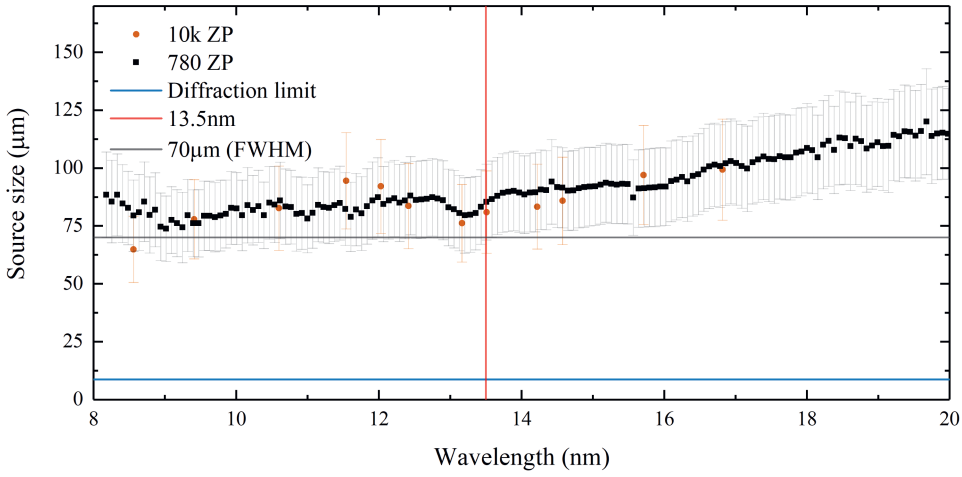

Figure 5.11: Source size characterization for a 40 mJ laser pulse with a focus size of 70 ± 7 µm FWHM diameter (grey line). The orange circles represent data taken using the 10k-tapered ZP with 780 lines/mm grating, while the black squares represent data measured with the 780-tapered ZP with 780 lines/mm grating. The error bars shown are based on estimation of the systematic error (see main text). The blue line represents the diffraction limit based on calculations for 780-ZP with a 780 lines/mm grating. The red line indicates the position of the 13.5 nm emission peak of the LPP.

In Fig. 5.11 the source size analysis is presented first over a wavelength range limited to 8–20 nm. The black square points represent data measured with the 780-ZP. The presented uncertainty error bars ($\sim$ 15–20%) are based on an analysis of the possible systematic errors propagating from uncertainties in accounting for the local baseline. We asses the robustness of our measurements and analysis by considering the source sizes obtained from the 10k-tapered ZP used with the same 780 lines/mm grating. The orange data markers represent data taken with the 10k-ZP at various x-positions (cf. Fig. 5.10) providing image foci at corresponding discrete wavelengths, between approximately 8 and 20 nm explaining the limited wavelength range of the current comparison. We note that the two data sets are in agreement over the entire range shown, which indicates the focal correctness of the alignment of the spectrometer within the accuracy of the measurements. The blue curve represents the calculated diffraction limit (Eq. 5.7) specifically for the 780-ZP. Clearly, all obtained source sizes are much larger than the diffraction limit and there is no need for further correction or deconvolution due to the diffraction limit.

After these additional experimental validation steps, we return to Fig. 5.11 to con-

clude that for the studied wavelength regime, the source size increases in step with emission wavelength. This increase of emission area with wavelength can be qualitatively understood on basis of a heuristic model of the emission from a hot surface, with the temperature monotonically decreasing away from the core (cf. Fig. 13 in ref. [112]). More specifically, the temperature profile may be expected to follow an approximately Gaussian shape given the Gaussian laser intensity distribution. We observe the surface head on. The center of the surface would be hottest and is responsible for the emission of the shortest wavelengths, as these are emitted by the higher charge states (cf. Chapter 2). It is necessarily the smallest region. The longer wavelengths will be emitted from areas with lower temperatures. We would observe this emission over a larger area, also from the center part as low temperature areas are in line of sight in front of the hotter core. The emission area would thus increase with wavelength, following the logic that the emission at ever larger wavelengths originates from ever lower temperatures.

Besides this overall trend, there is a faint indication in our data of a modest drop in the source size values at around $\sim$12–13.5 nm. This may be due to large optical depth precisely near 13.5 nm [49]. Further study would be required to unambiguously identify any such effects.

We next expand the scope of our investigation to the larger 8–34.5 nm wavelength range and actively vary the size of the plasma emission area. We note that in this wavelength range we avoid strong contributions from higher diffraction and imaging orders. Three different source sizes are obtained by changing the size of the beam spot by moving the focusing lens through focus. The laser energy is set to maintain the effective plasma temperature as qualitatively obtained by inspecting the EUV spectrum without the ZP. Fig. 5.12 presents data in this full range using the 780-tapered zone plate matched to the 780 lines/mm grating. The first source size is obtained using a 40 mJ laser energy in combination with a beam's FWHM of 70 ± 7 µm (black square points in Fig. 5.12). The parameters for the second source size are a laser energy of 80 mJ with a FWHM of 86 ± 9 µm (green triangle points in Fig. 5.12). For the third source size a 160 mJ is used with a FWHM of 124 ± 12 µm (yellow rhomboid points in Fig. 5.12). We note that the scaling of the laser pulse energy needed to maintain plasma temperature is monotonic as expected, and roughly follows the expected quadratic scaling of the focus size, assuming that the effective temperature is set by the average laser intensity. Any deviations from this scaling may be attributed to uncertainties in establishing the laser focus size or the finite energy step size in our studies.

Fig. 5.12 demonstrates that the source size monotonically increases with emission wavelength over the full measured range, for all three cases shown. The three dif-

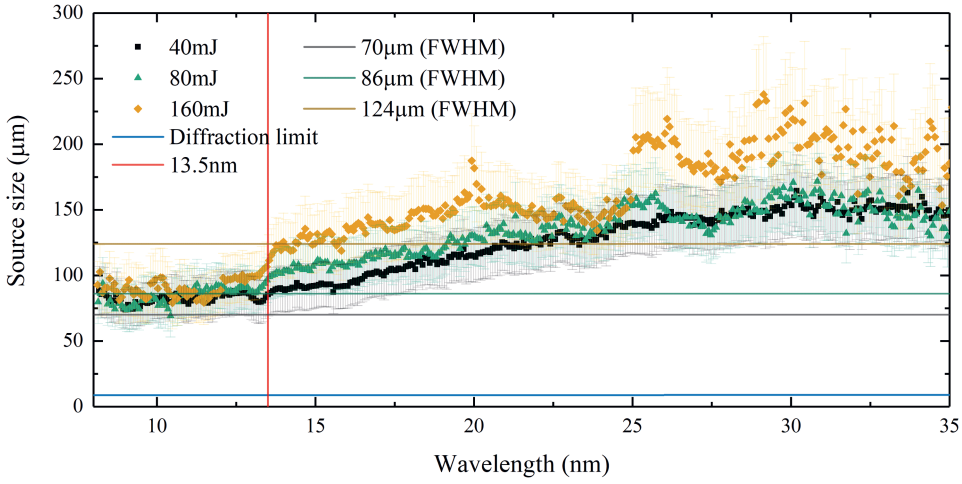

Figure 5.12: Source size measurements. All data were taken with a 780-tapered ZP with a 780 lines/mm grating. The black squares are taken with a laser energy of 40 mJ and a FWHM of 70 ± 7 µm (grey line), the green triangles for 80 mJ and FWHM of 86 ± 9 µm (green line), and the yellow rhomboids for 160 mJ and FWHM of 124 ± 12 µm (yellow line). Uncertainties (error bars) are as in Fig. 5.11, also see main text. The blue curve represents the diffraction limit based on calculations for 780-ZP with a 780 lines/mm grating. The red line indicates the position of the 13.5 nm emission peak of the LPP.

ferent laser focus conditions appear to share a common source size for the shortest wavelengths. Beyond approximately 14 nm however the three cases become clearly distinguishable with the emission size increasing in step with the size of the laser focus.

This increase of emission size with the laser focus is expected as the size of the plasma area with a sufficiently high temperature increases with the laser spot size (when maintaining laser intensity). However, inspection of Fig. 5.12 suggests that the scaling of the emission area with laser spot size is more complex and a quantitative assessment would benefit from detailed radiation-hydrodynamics modeling. In particular, we note again that the size of the emission area for the shortest wavelengths appears to not be dependent on the laser beam size. This is a surprising finding also in light of previous investigations by, for example, Schupp et al. [15] who concluded that the observed increase in conversion efficiency with increasing target size could be explained from an increase in laser-target overlap and, thus, emission area. We note that in our current measurement the geometric overlap of the laser pulse with the target is complete. Further, detailed analysis of the emission

area near the important in-band region is required to resolve this observation, which is in principle possible with the present imaging spectrometer.

5.5 Conclusions

We presented a novel imaging spectrometer where we combined a 780 lines/mm transmission grating and a zone plate, tapered to match the grating dispersion. The design of the imaging spectrometer and the (nano)fabrication process was detailed. We next demonstrated achromatic one-dimensional imaging of plasma light sources in a 8–34.5 nm wavelength range. The obtained images were compared to numerical simulations of the imaging spectrometer's diffracting elements. Finally, we obtained the effective size of the emitting medium of an Sn LPP and showed that it increased with emission wavelength in line with heuristic arguments. Also, the emission area overall increased with laser spot size as expected.

We expect that the imaging spectrometer will find application in assessing the emission sizes of plasmas generated from tin microdroplet targets as used in the industry. It may be employed to further investigate the origins of the relatively strong DUV emission found in Chapters 3 and 4 of this Thesis. Improvements to the current design may be made. In particular, suppression of the higher-order diffraction/imaging contributions would be beneficial and could be enacted by adding suitable filters (cf. Chapter 3) or by actively blocking higher imaging orders. In addition to these improvements to the imaging, the current CCD could be replaced by a gated microchannel plate (MCP) which would enable time-resolved imaging. Such time-resolved imaging would be highly beneficial for better understanding the dynamics of the highly transient plasma.

5.6 Acknowledgments

This project is funded by TKI-HTSM with the project name "Spectral Unraveling of EUV Lithography Light Sources (SUN)". Part of this work has been carried out within the Advanced Research Center for Nanolithography, a public-private partnership of the University of Amsterdam, the Vrije Universiteit Amsterdam, the Dutch Research Council (NWO) and the semiconductor equipment manufacturer ASML and was financed by Toeslag voor Topconsortia voor Kennis en Innovatie from the Dutch Ministry of Economic Affairs. The transmission grating spectrometer was developed in the Industrial Focus Group XUV Optics at the University of Twente and supported by the FOM Valorisation Prize 2011 awarded to F. Bijkerk and NanoNextNL Valorisation Grant awarded to M. Bayraktar in 2015. This project received further

funding from the European Research Council Starting Grant No. 802648 and is part of the VIDI research programme with Project No. 15697, which is financed by NWO. The authors would like to thank Henk-Jan Boluijt, mechanical engineer of AMOLF, for his contribution to the design and the building of the imaging spectrometer setup. The authors would like to thank Caspar Bruineman, Scientec Engineering, for his contribution to the design and the building of the imaging spectrometer setup. The authors would like to thank Dr. Laurens van Buuren, techinician of EUV Plasma Processes group of the Advanced Research Center for Nanolithography, for his contribution to the building of the imaging spectrometer setup. The authors would like to thank Dr. Boris Vratzov, Nanotechnology and Devices, for the fabrication of the zone plates and the transmission gratings. The authors would like to thank Dr. Mengqi Du, postdoctoral researcher of EUV Generation & Imaging of the Advanced Research Center for Nanolithography, Amsterdam, The Netherlands, for her valuable contribution to the simulations' part of this chapter.

Conclusions

This Thesis explored the spectral and spatial characteristics of laser-driven plasma sources of EUV light. The work reported in this Thesis mainly focused on the out-of-band radiation produced by tin laser-produced plasma, in contrast to most of the available literature – which covers mostly the wavelength range close to the in-band radiation near 13.5 nm. Out-of-band radiation can provide key insights into the production of EUV light, and is by itself of particular interest as certain wavelength ranges may be detrimental to the lithography processes. For our work, we carefully calibrated the intensity response of a transmission grating spectrometer and added novel imaging capabilities to the spectrometer. In the following, the main conclusions from each Chapter are first separately formulated, and next synthesized into Thesis-overarching conclusions as well as an outlook.

In **Chapter 2**, emission spectra from Sn^{5+}–Sn^{10+} ions are presented as measured from an electron-beam ion trap (EBIT) and from laser-produced plasma (LPP) in the 12.6–20.8 nm wavelength regime encompassing the 13.5 nm emission used in modern nanolithography. Emission line features were identified in the EBIT spectra using the Cowan code. We newly identified $4d$–$5f$ and $4d$–$6f$ transition arrays in Sn^{6+} as well as $4p$–$4d$ transitions in Sn^{5+}. Next, the EBIT spectra were used to assign contributions of specific charge states to the tin LPP emission spectra. Emission spectra were obtained from plasma produced from both a liquid microdroplet and a planar solid target. For the planar solid Sn target, the $4d$–$5p$ transitions of Sn^{8+}–Sn^{10+} ions were found to dominate. Transitions of type $4d$–$4f$ + $4p$–$4d$ appeared as self-absorption dips in the spectra. For the droplet target, we found a clear evolution of the charge-state distribution with laser intensity – with the transitions apparent in

emission, not absorption. The study demonstrated that out-of-band emissions may be employed to individually monitor charge states that strongly contribute to the unresolved transition array at 13.5 nm.

In **Chapter 3**, a fully calibrated spectrum from a microdroplet-tin plasma driven by 1-µm laser light under conditions relevant for the production of EUV at 13.5 nm for nanolithography is presented in the 5.5–265.5 nm wavelength regime. The spectrum was obtained using a transmission grating spectrometer equipped with a series of filters. We carefully calibrated the gratings and the filters to enable measurements free of any higher diffraction orders. The dominant remaining uncertainty stems from the correction for quantum efficiency of the CCD camera. The now fully calibrated spectrometer provides access to previously inaccessible out-of-band wavelength ranges, and may in the future be used to optimize industrial EUV sources. In fact, over the course of the project, the calibrated spectrometer was employed to diagnose the tin-disk discharge source at TNO Delft as well as the Xe-gas discharge source at ASML Research in Veldhoven.

In **Chapter 4**, a fully calibrated spectrum from 6.5 to 264.5 nm from a microdroplet-tin plasma driven by 2-µm laser light is presented. First, 2-µm LPP spectra are shown from overheated and underheated plasma. In all cases the dominant radiation was emitted in the 5–70 nm wavelength band, while the useful range of 13.2–13.8 nm for applications in EUV nanolithography was produced efficiently. Next, a 2-µm LPP spectrum is compared to the 1-µm LPP spectrum as presented in Chapter 3. This comparison demonstrated that the 2-µm case offers higher efficiency to produce light in the 13.2–13.8 nm EUV regime. From available calculations (using Cowan and FAC atomic codes) we found that $4d$–$5p$ transitions in multiply charged Sn^{4+}–Sn^{10+} dominate the emission spectra of both 1- and 2-µm in the ∼15–37 nm wavelength regime. The spectrum showed evidence that the plasma emission size should increase with increasing wavelength beyond ∼75 nm.

In **Chapter 5**, the development and commissioning of a novel imaging spectrometer, which combines one-dimensional imaging with spectral measurements, is presented. This spectrometer combines a transmission grating with a Fresnel zone plate. This zone plate was engineered, using nanofabrication techniques, to have variable zone widths to match the grating dispersion. Using the newly developed imaging spectrometer, we recorded the emission from LPP generated from a solid tin target over a wide, ∼5–75 nm wavelength range. The observed imaging characteristics were compared to numerical wave propagation simulations, which enabled, e.g., verifying the presence of higher imaging orders. From the recorded spectral images, we obtained strong evidence of increasing plasma emission size with wavelength, in line with the findings of Chapter 4.

Looking forward, the imaging spectrometer could benefit from further expanding the calibration efforts to include the detailed calibration of the Fresnel zone plate, as well as the in-use CCD camera response. Further envisioned developments include the replacement of the CCD with a gated microchannel plate to facilitate time-resolved imaging. The imaging would also benefit from the suppression of higher imaging orders, by for instance adding suitable filters or apertures – or optimizing the zone plate design. For application purposes, the size and weight of the vacuum chamber and its connections should be further optimized.

The commissioning of the newly developed spectrometer marked the key milestone of this Thesis. It enabled us to firmly establish that the size of the emitting area of the plasma, as produced on a solid tin target, is a function of the emission wavelength. The imaging spectrometer should next be employed to study the radiation produced from laser-driven tin-microdroplet plasma, to see if also here the plasma size increases with wavelength. We envision that the apparatus will first be mounted on one of ARCNL's solid-state-laser-driven plasma light sources. The spectrometer may also yield important insights for current industrial CO_2-gas-laser-driven EUV light sources.

Bibliography

[1] J. Bardeen, W.H. Brattain, The Transistor, A Semi-Conductor Triode, Phys. Rev. **74**, 230 (1948)

[2] G.E. Moore, Cramming more components onto integrated circuits, Reprinted from Electronics, volume 38, number 8, April 19, 1965, pp.114 ff., IEEE J. Solid-State Circuits Society Newsletter **11**(3), 33 (2006)

[3] C.D. Young. Enabling semiconductor innovation and growth. BAML 2018 APAC TMT Conference Taipei, Taiwan (2018)

[4] O.O. Versolato, Physics of laser-driven tin plasma sources of EUV radiation for nanolithography, Plasma Sourc. Sci. Tech. **28**(8), 083001 (2019)

[5] M. Purvis, I.V. Fomenkov, A.A. Schafgans, M. Vargas, S. Rich, Y. Tao, S.I. Rokitski, M. Mulder, E. Buurman, M. Kats, J. Stewart, A.D. LaForge, C. Rajyaguru, G. Vaschenko, A.I. Ershov, R.J. Rafac, M. Abraham, D.C. Brandt, D.J. Brown, in *Extreme Ultraviolet (EUV) Lithography IX*, vol. 10583, ed. by K.A. Goldberg. International Society for Optics and Photonics (SPIE, 2018), vol. 10583, pp. 476 – 485

[6] S.K. Moore, EUV lithography finally ready for fabs, IEEE Spectr. **55**(1), 46 (2018)

[7] H. Mizoguchi, H. Nakarai, T. Abe, K.M. Nowak, Y. Kawasuji, H. Tanaka, Y. Watanabe, T. Hori, T. Kodama, Y. Shiraishi, T. Yanagida, G. Soumagne, T. Ya-

mada, T. Yamazaki, T. Saitou, in *2018 China Semiconductor Technology International Conference (CSTIC)* (2018), pp. 1–7

[8] A.Y. Vinokhodov, M.S. Krivokorytov, Y.V. Sidelnikov, V.M. Krivtsun, V.V. Medvedev, K.N. Koshelev, Droplet-based, high-brightness extreme ultraviolet laser plasma source for metrology, J. Appl. Phys. **120**(16), 163304 (2016)

[9] V.Y. Banine, K.N. Koshelev, G.H.P.M. Swinkels, Physical processes in EUV sources for microlithography, J. Phys. D **44**(25), 253001 (2011)

[10] J. Benschop, V. Banine, S. Lok, E. Loopstra, Extreme ultraviolet lithography: Status and prospects, J. Vac. Sci. Technol. B **26**(6), 2204 (2008)

[11] D. Kurilovich, A.L. Klein, F. Torretti, A. Lassise, R. Hoekstra, W. Ubachs, H. Gelderblom, O.O. Versolato, Plasma Propulsion of a Metallic Microdroplet and its Deformation upon Laser Impact, Phys. Rev. Appl. **6**, 014018 (2016)

[12] B. Liu, D. Kurilovich, H. Gelderblom, O.O. Versolato, Mass Loss from a Stretching Semitransparent Sheet of Liquid Tin, Phys. Rev. Appl. **13**, 024035 (2020)

[13] L. Behnke, R. Schupp, Z. Bouza, M. Bayraktar, Z. Mazzotta, R. Meijer, J. Sheil, S. Witte, W. Ubachs, R. Hoekstra, O.O. Versolato, Extreme ultraviolet light from a tin plasma driven by a 2-µm-wavelength laser, Opt. Express **29**(3), 4475 (2021)

[14] R. Schupp, F. Torretti, R.A. Meijer, M. Bayraktar, J. Sheil, J. Scheers, D. Kurilovich, A. Bayerle, A.A. Schafgans, M. Purvis, K.S.E. Eikema, S. Witte, W. Ubachs, R. Hoekstra, O.O. Versolato, Radiation transport and scaling of optical depth in Nd:YAG laser-produced microdroplet-tin plasma, Appl. Phys. Lett. **115**(12), 124101 (2019)

[15] R. Schupp, F. Torretti, R. Meijer, M. Bayraktar, J. Scheers, D. Kurilovich, A. Bayerle, K. Eikema, S. Witte, W. Ubachs, R. Hoekstra, O.O. Versolato, Efficient Generation of Extreme Ultraviolet Light From Nd:YAG-Driven Microdroplet-Tin Plasma, Phys. Rev. Appl. **12**, 014010 (2019)

[16] S. Fujioka, H. Nishimura, K. Nishihara, A. Sasaki, A. Sunahara, T. Okuno, N. Ueda, T. Ando, Y. Tao, Y. Shimada, K. Hashimoto, M. Yamaura, K. Shigemori, M. Nakai, K. Nagai, T. Norimatsu, T. Nishikawa, N. Miyanaga, Y. Izawa, K. Mima, Opacity effect on extreme ultraviolet radiation from laser-produced tin plasmas, Phys. Rev. Lett. **95**(23), 235004 (2005)

[17] R. Schupp, L. Behnke, Z. Bouza, Z. Mazzotta, Y. Mostafa, A. Lassise, L. Poirier, J. Sheil, M. Bayraktar, W. Ubachs, R. Hoekstra, O.O. Versolato, Characteriza-

tion of angularly resolved EUV emission from 2-μm-wavelength laser-driven sn plasmas using preformed liquid disk targets, J. Phys. D: Appl. Phys. **54**(36), 365103 (2021)

[18] V.I. Azarov, Y.N. Joshi, Analysis of the $4d^7 - 4d^6 5p$ transition array of the eighth spectrum of tin: Sn VIII, J. Phys. B **26**(20), 3495 (1993)

[19] S.S. Churilov, A.N. Ryabtsev, Analysis of the $4p^6\ 4d^7$–($4p^6\ 4d^6 4f\ +\ 4p^5\ 4d^8$) transitions in the Sn VIII spectrum, Opt. Spectrosc. **100**(5), 660 (2006)

[20] S.S. Churilov, A.N. Ryabtsev, Analyses of the Sn IX–Sn XII spectra in the EUV region, Phys. Scr. **73**(6), 614 (2006)

[21] A.N. Ryabtsev, É.Y. Kononov, S.S. Churilov, Spectra of rubidium-like Pd X-Sn XIV ions, Opt. Spectrosc. **105**(6), 844 (2008)

[22] I.Y. Tolstikhina, S.S. Churilov, A.N. Ryabtsev, K.N. Koshelev, in *EUV sources for lithography*, ed. by V. Bakshi (SPIE Press, 2006), chap. 4, pp. 113–148

[23] R. D'Arcy, H. Ohashi, S. Suda, H. Tanuma, S. Fujioka, H. Nishimura, K. Nishihara, C. Suzuki, T. Kato, F. Koike, J. White, G. O'Sullivan, Transitions and the effects of configuration interaction in the spectra of Sn XV–Sn XVIII, Phys. Rev. A **79**, 042509 (2009)

[24] H. Ohashi, S. Suda, H. Tanuma, S. Fujioka, H. Nishimura, A. Sasaki, K. Nishihara, EUV emission spectra in collisions of multiply charged Sn ions with He and Xe, J. Phys. B **43**(6), 065204 (2010)

[25] J. Colgan, D. Kilcrease, J. Abdallah, M. Sherrill, C. Fontes, P. Hakel, G. Armstrong, Atomic structure considerations for the low-temperature opacity of Sn, High Energy Density Phys. **23**, 133 (2017)

[26] F. Torretti, A. Windberger, A. Ryabtsev, S. Dobrodey, H. Bekker, W. Ubachs, R. Hoekstra, E.V. Kahl, J.C. Berengut, J.R. Crespo López-Urrutia, O.O. Versolato, Optical spectroscopy of complex open-$4d$-shell ions $\mathrm{Sn}^{7+} - \mathrm{Sn}^{10+}$, Phys. Rev. A **95**, 042503 (2017)

[27] J. Scheers, C. Shah, A. Ryabtsev, H. Bekker, F. Torretti, J. Sheil, D.A. Czapski, J.C. Berengut, W. Ubachs, J.R. Crespo López-Urrutia, R. Hoekstra, O.O. Versolato, EUV spectroscopy of highly charged Sn^{13+}-Sn^{15+} ions in an electron-beam ion trap, Phys. Rev. A **101**, 062511 (2020)

[28] D.L. Windt, IMD—Software for modeling the optical properties of multilayer films, Comput. phys. **12**(4), 360 (1998)

[29] B. Henke, E. Gullikson, J. Davis, X-Ray Interactions: Photoabsorption, Scattering, Transmission, and Reflection at E = 50-30,000 eV, Z = 1-92, At. Data Nucl. Data Tables **54**(2), 181 (1993)

[30] E.D. Palik, *Handbook of optical constants of solids*, vol. 1 (Academic press, 1985)

[31] A. Heays, A.D.v. Bosman, E.F. van Dishoeck, Photodissociation and photoionisation of atoms and molecules of astrophysical interest, Astron. Astrophys. **602**, A105 (2017)

[32] R.M. van der Horst, J. Beckers, E.A. Osorio, D.I. Astakhov, W.J. Goedheer, C.J. Lee, V.V. Ivanov, V.M. Krivtsum, K.N. Koshelev, D.V. Lopaev, F. Bijkerk, V.Y. Banine, Exploring the electron density in plasma induced by EUV radiation: I. Experimental study in hydrogen, J. Phys. D: Appl. Phys. **49**(14), 145203 (2016)

[33] M.A. van de Kerkhof, F. Liu, M. Meeuwissen, X. Zhang, M. Bayraktar, R.C. de Kruif, N.V. Davydova, High-power EUV lithography: spectral purity and imaging performance, J. Micro/Nanolithogr. MEMS MOEMS **19**(3), 1 (2020)

[34] V. Banine, J.P. Benschop, M. Leenders, R. Moors, in *Emerging Lithographic Technologies IV*, vol. 3997, ed. by E.A. Dobisz. International Society for Optics and Photonics (SPIE, 2000), vol. 3997, pp. 126 – 135

[35] G. Joseph, M. Olszewski, T. McCormack, P. Dunne, F. O'Reilly, Laser plasma imaging and spectroscopy to enhance radiance for water window source development, Nucl. Instrum. Methods Phys. Res. B: Beam Interact. Mater. At. **482**, 64 (2020)

[36] B. Jones, C. Deeney, C. Meyer, C. Coverdale, P.D. LePell, J.P. Apruzese, R. Clark, J. Davis, K. Peterson, in *AIP Conference Proceedings*, vol. 926 (American Institute of Physics, 2007), vol. 926, pp. 229–237

[37] C.K. Gary, D.E. Doggett, J.L. Harris, S.A. Pikuz, T.A. Shelkovenko, in *IEEE Conference Record - Abstracts. 2005 IEEE International Conference on Plasma Science* (2005), pp. 180–180

[38] F. Döring, B. Rösner, M. Langer, A. Kubec, A. Kleibert, J. Raabe, C.A.F. Vaz, M. Lebugle, C. David, Multifocus off-axis zone plates for x-ray free-electron laser experiments, Optica **7**(8), 1007 (2020)

[39] J.O. Schunck, F. Döring, B. Rösner, J. Buck, R.Y. Engel, P.S. Miedema, S.K. Mahatha, M. Hoesch, A. Petraru, H. Kohlstedt, C. Schüssler-Langeheine, K. Rossnagel, C. David, M. Beye, Soft x-ray imaging spectroscopy with micrometer resolution, Optica **8**(2), 156 (2021)

[40] G.R. Fowles, *Introduction to modern optics* (Courier Corporation, 1989)

[41] G. O'Sullivan, B. Li, R. D'Arcy, P. Dunne, P. Hayden, D. Kilbane, T. McCormack, H. Ohashi, F. O'Reilly, P. Sheridan, et al., Spectroscopy of highly charged ions and its relevance to EUV and soft x-ray source development, J. Phys. B **48**(14), 144025 (2015)

[42] J. Scheers, C. Shah, A. Ryabtsev, H. Bekker, F. Torretti, J. Sheil, D.A. Czapski, J.C. Berengut, W. Ubachs, J.R.C. López-Urrutia, R. Hoekstra, O.O. Versolato, EUV spectroscopy of highly charged Sn^{13+} - Sn^{15+} ions in an electron-beam ion trap, Phys. Rev. A **101**, 062511 (2020)

[43] S. Bajt, J.B. Alameda, T.W. Barbee, Jr., W.M. Clift, J.A. Folta, B.B. Kaufmann, E.A. Spiller, Improved reflectance and stability of Mo-Si multilayers, Opt. Eng. **41**(8), 1797 (2002)

[44] Q. Huang, V. Medvedev, R. van de Kruijs, A. Yakshin, E. Louis, F. Bijkerk, Spectral tailoring of nanoscale EUV and soft x-ray multilayer optics, Appl. Phys. Rev. **4**(1), 011104 (2017)

[45] S.S. Churilov, A.N. Ryabtsev, Analysis of the Spectra of In XII–XIV and Sn XIII–XV in the Far–VUV Region, Opt. Spectr. **101**(2), 169 (2006)

[46] W. Svendsen, G. O'Sullivan, Statistics and characteristics of xuv transition arrays from laser-produced plasmas of the elements tin through iodine, Phys. Rev. A **50**, 3710 (1994)

[47] S.S. Churilov, R.R. Kildiyarova, A.N. Ryabtsev, A. Kramida, Y.N. Joshi, Analysis of the $4d^9$–$4d^8(4f + 6p)$ transition array of Sn VI, Phys. Scr. **50**(5), 463 (1994)

[48] V.I. Azarov, Y.N. Joshi, S.S. Churilov, A.N. Ryabtsev, Analysis of the $4d^7(4f + 6p)$ and $4p^5 4d^9$ configurations of Sn VII, Sb VIII and Te IX, Phys. Scr. **50**(6), 642 (1994)

[49] F. Torretti, J. Sheil, R. Schupp, M.M. Basko, M. Bayraktar, R.A. Meijer, S. Witte, W. Ubachs, R. Hoekstra, O.O. Versolato, A.J. Neukirch, J. Colgan, Prominent radiative contributions from multiply-excited states in laser-produced tin plasma for nanolithography, Nat. Commun. **11**(1), 1 (2020)

[50] K. Liu, Y. Li, F. Zhang, M. Fan, Transient Thermal and Structural Deformation and Its Impact on Optical Performance of Projection Optics for Extreme Ultraviolet Lithography, Jpn. J. Appl. Phys. **46**(10A), 6568 (2007)

[51] G. Yang, Y. Li, in *Extreme Ultraviolet (EUV) Lithography III*, vol. 8322 (International Society for Optics and Photonics, 2012), vol. 8322, p. 83222V

[52] F. Torretti, R. Schupp, D. Kurilovich, A. Bayerle, J. Scheers, W. Ubachs, R. Hoekstra, O.O. Versolato, Short-wavelength out-of-band EUV emission from Sn laser-produced plasma, J. Phys. B **51**(4), 045005 (2018)

[53] F. Torretti, F. Liu, M. Bayraktar, J. Scheers, Z. Bouza, W. Ubachs, R. Hoekstra, O. Versolato, Spectral characterization of an industrial EUV light source for nanolithography, J. Phys. D **53**(5), 055204 (2019)

[54] R.D. Cowan, *The Theory of Atomic Structure and Spectra* (University of California Press, 1981)

[55] A. Kramida, Cowan code: 50 years of growing impact on atomic physics, Atoms **7**(3), 64 (2019)

[56] S.W. Epp, J.R. Crespo López-Urrutia, M.C. Simon, T. Baumann, G. Brenner, R. Ginzel, N. Guerassimova, V. Mäckel, P.H. Mokler, B.L. Schmitt, et al., X-ray laser spectroscopy of highly charged ions at FLASH, J. Phys. B **43**(19), 194008 (2010)

[57] T. Harada, T. Kita, Mechanically ruled aberration-corrected concave gratings, Appl. Opt. **19**(23), 3987 (1980)

[58] T.M. Baumann, Spektroskopische Untersuchungen resonanter Rekombinationsprozesse an hochgeladenem Silizium in einer Elektronenstrahl-Ionenfalle. Ph.D. thesis, Ruprecht-Karls-Universität Heidelberg (2012)

[59] G.Y. Liang, J.R. Crespo López-Urrutia, T.M. Baumann, S.W. Epp, A. Gonchar, A. Lapierre, P.H. Mokler, M.C. Simon, H. Tawara, V. Mäckel, K. Yao, G. Zhao, Y. Zou, J. Ullrich, Experimental investigations of ion charge distributions, effective electron densities, and electron-ion cloud overlap in electron beam ion trap plasma using extreme-ultraviolet spectroscopy, Astrophys. J. **702**(2), 838 (2009)

[60] A. Kramida, Yu. Ralchenko, J. Reader, NIST ASD Team. NIST Atomic Spectra Database (ver. 5.3), [Online]. Available: `http://physics.nist.gov/asd` [2016, February 2]. National Institute of Standards and Technology, Gaithersburg, MD. (2015)

[61] A. Windberger, F. Torretti, A. Borschevsky, A. Ryabtsev, S. Dobrodey, H. Bekker, E. Eliav, U. Kaldor, W. Ubachs, R. Hoekstra, J.R. Crespo López-Urrutia, O.O. Versolato, Analysis of the fine structure of $\mathrm{Sn}^{11+} - \mathrm{Sn}^{14+}$ ions by optical spectroscopy in an electron-beam ion trap, Phys. Rev. A **94**, 012506 (2016)

[62] S.J. Goh, H.J.M. Bastiaens, B. Vratzov, Q. Huang, F. Bijkerk, K.J. Boller, Fabrication and characterization of free-standing, high-line-density transmission gratings for the vacuum UV to soft X-ray range, Opt. Express **23**(4), 4421 (2015)

[63] M. Bayraktar, H.M.J. Bastiaens, C. Bruineman, B. Vratzov, F. Bijkerk, Broadband transmission grating spectrometer for measuring the emission spectrum of EUV sources, NEVAC blad **54**(1), 14 (2016)

[64] A. Bayerle, M.J. Deuzeman, S. van der Heijden, D. Kurilovich, T. de Faria Pinto, A. Stodolna, S. Witte, K.S.E. Eikema, W. Ubachs, R. Hoekstra, O.O. Versolato, Sn ion energy distributions of ns- and ps-laser produced plasmas, Plasma Sourc. Sci. Tech. **27**(4), 045001 (2018)

[65] J. Bauche, C. Bauche-Arnoult, M. Klapisch, Transition arrays in the spectra of ionized atoms, Adv. Atom. Mol. Phys. **23**, 131 (1988)

[66] J. Bauche, C. Bauche-Arnoult, O. Peyrusse, *Atomic properties in hot plasmas* (Springer, 2015)

[67] H. Bekker, O.O. Versolato, A. Windberger, N.S. Oreshkina, R. Schupp, T.M. Baumann, Z. Harman, C.H. Keitel, P.O. Schmidt, J. Ullrich, J. R. Crespo López-Urrutia, Identifications of $5s_{1/2}$–$5p_{3/2}$ and $5s^2$–$5s\,5p$ EUV transitions of promethium-like Pt, Ir, Os and Re, J. Phys. B **48**(14), 144018 (2015)

[68] S.S. Churilov, Y.N. Joshi, A.N. Ryabtsev, The $4d^{10}\ {}^1S_0$–$4d^9(np + nf)$ transitions in the Pd I isoelectronic sequence from Cd III to Cs X, J. Phys. B **27**(22), 5485 (1994)

[69] Y.V. Ralchenko, Y. Maron, Accelerated recombination due to resonant deexcitation of metastable states, J. Quant. Spectrosc. Radiat. Transf. **71**(2), 609 (2001)

[70] G.J. van het Hof, Y.N. Joshi, The analysis of the $4d^8$, $4d^7\ 5s$ and $4d^7\ 5p$ configurations of six-times ionized tin: Sn VII, Phys. Scr. **48**(6), 714 (1993)

[71] A. Ryabtsev, R. Kildiyarova, E. Kononov, Spectrum of Sn^{5+} in the region 500-–1300 Å, Atoms **5**(4), 47 (2017)

[72] M.M. Basko, V.G. Novikov, A.S. Grushin, On the structure of quasi-stationary laser ablation fronts in strongly radiating plasmas, J. Plasma Phys. **22**(5), 053111 (2015)

[73] M. Lysaght, D. Kilbane, N. Murphy, A. Cummings, P. Dunne, G. O'Sullivan, Opacity of neutral and low ion stages of Sn at the wavelength 13.5 nm used in extreme-ultraviolet lithography, Phys. Rev. A **72**, 014502 (2005)

[74] Z. Bouza, J. Scheers, A. Ryabtsev, R. Schupp, L. Behnke, C. Shah, J. Sheil, M. Bayraktar, J.R.C. López-Urrutia, W. Ubachs, R. Hoekstra, O.O. Versolato, EUV spectroscopy of Sn^{5+}-Sn^{10+} ions in an electron beam ion trap and laser-produced plasmas, J. Phys. B: At. Mol. Opt. Phys. **53**(19), 195001 (2020)

[75] R. Schupp, L. Behnke, J. Sheil, Z. Bouza, M. Bayraktar, W. Ubachs, R. Hoekstra, O.O. Versolato, Characterization of 1- and $2-\mu$m-wavelength laser-produced microdroplet-tin plasma for generating extreme-ultraviolet light, Phys. Rev. Res. **3**, 013294 (2021)

[76] H. Sakaguchi, S. Fujioka, S. Namba, H. Tanuma, H. Ohashi, S. Suda, M. Shimomura, Y. Nakai, Y. Kimura, Y. Yasuda, H. Nishimura, T. Norimatsu, A. Sunahara, K. Nishihara, N. Miyanaga, Y. Izawa, K. Mima, Absolute evaluation of out-of-band radiation from laser-produced tin plasmas for extreme ultraviolet lithography, Appl. Phys. Lett. **92**(11), 111503 (2008)

[77] S. Namba, S. Fujioka, H. Sakaguchi, H. Nishimura, Y. Yasuda, K. Nagai, N. Miyanaga, Y. Izawa, K. Mima, K. Sato, K. Takiyama, Characterization of out-of-band radiation and plasma parameters in laser-produced Sn plasmas for extreme ultraviolet lithography light sources, J. Appl. Phys. **104**(1), 013305 (2008)

[78] N. Gambino, B. Rollinger, D. Hudgins, R.S. Abhari, Spectral emission properties of a laser-produced plasma light source in the sub-200 nm range for wafer inspection applications, J. Micro/Nanolithogr. MEMS MOEMS **14**(3), 1 (2015)

[79] N. Gambino, B. Rollinger, M. Brandstätter, R.S. Abhari, Vacuum ultraviolet spectral emission properties of Ga, In and Sn droplet-based laser produced plasmas, Spectrochim. Acta B: At. Spectrosc. **122**, 149 (2016)

[80] J. Scheers, R. Schupp, R. Meijer, W. Ubachs, R. Hoekstra, O.O. Versolato, Time- and space-resolved optical Stark spectroscopy in the afterglow of laser-produced tin-droplet plasma, Phys. Rev. E **102**, 013204 (2020)

[81] I.V. Fomenkov, D.C. Brandt, A.N. Bykanov, A.I. Ershov, W.N. Partlo, D.W. Myers, N.R. Böwering, G.O. Vaschenko, O.V. Khodykin, J.R. Hoffman, E.V. L., R.D. Simmons, J.A. Chavez, C.P. Chrobak, in *Emerging Lithographic Technologies XI*, vol. 6517, ed. by M.J. Lercel. International Society for Optics and Photonics (SPIE, 2007), vol. 6517, pp. 1021 – 1031

[82] D. Campos, S.S. Harilal, A. Hassanein, The effect of laser wavelength on emission and particle dynamics of Sn plasma, J. Appl. Phys. **108**(11), 113305 (2010)

[83] N. Davydova, E. van Setten, R. de Kruif, B. Connolly, N. Fukugami, Y. Kodera, H. Morimoto, Y. Sakata, J. Kotani, S. Kondo, T. Imoto, H. Rolff, A. Ullrich,

R.K. Jaganatharaja, A. Lammers, D. Oorschot, C.W. Man, G. Schiffelers, J. van Dijk, in *30th European Mask and Lithography Conference*, vol. 9231, ed. by U.F.W. Behringer. International Society for Optics and Photonics (SPIE, 2014), vol. 9231, pp. 1 – 14

[84] H. Parchamy, J. Szilagyi, M. Masnavi, M. Richardson, Ultraviolet out-of-band radiation studies in laser tin plasma sources, J. Appl. Phys. **122**(17), 173303 (2017)

[85] M. van de Kerkhof, F. Liu, M. Meeuwissen, X. Zhang, R. de Kruif, N. Davydova, G. Schiffelers, F. Wählisch, E. van Setten, W. Varenkamp, K. Ricken, L. de Winter, J. McNamara, M. Bayraktar, in *Extreme Ultraviolet (EUV) Lithography XI*, vol. 11323, ed. by N.M. Felix, A. Lio. International Society for Optics and Photonics (SPIE, 2020), vol. 11323, pp. 435 – 450

[86] R.A. Meijer, A.S. Stodolna, K.S.E. Eikema, S. Witte, High-energy Nd:YAG laser system with arbitrary sub-nanosecond pulse shaping capability, Opt. Lett. **42**(14), 2758 (2017)

[87] D. Kurilovich, M.M. Basko, D.A. Kim, F. Torretti, R. Schupp, J.C. Visschers, J. Scheers, R. Hoekstra, W. Ubachs, O.O. Versolato, Power-law scaling of plasma pressure on laser-ablated tin microdroplets, Phys. Plasmas **25**(1), 012709 (2018)

[88] B. Liu, R.A. Meijer, J. Hernandez-Rueda, D. Kurilovich, Z. Mazzotta, S. Witte, O.O. Versolato, Laser-induced vaporization of a stretching sheet of liquid tin, J. Appl. Phys. **129**(5), 053302 (2021)

[89] T.A. Johnson, R. Soufli, E.M. Gullikson, M. Clift, in *Optical Constants of Materials for UV to X-Ray Wavelengths*, vol. 5538, ed. by R. Soufli, J.F. Seely. International Society for Optics and Photonics (SPIE, 2004), vol. 5538, pp. 119 – 124

[90] A. Joseph, M.H. Modi, A. Singh, R.K. Gupta, G.S. Lodha, in *AIP Conference Proceedings*, vol. 1512 (American Institute of Physics, 2013), vol. 1512, pp. 498–499

[91] F.R. Powell, P.W. Vedder, J.F. Lindblom, S.F. Powell, Thin film filter performance for extreme ultraviolet and x-ray applications, Opt. Eng. **29**(6), 614 (1990)

[92] greateyes GmbH. Scientific Full-frame CCD Cameras for VUV, EUV, X-Ray Imaging and Spectroscopy (2017)

[93] J. Heymes, M. Soman, G. Randall, A. Gottwald, A. Harris, A. Kelt, I. Moody, X. Meng, A.D. Holland, Comparison of back-thinned detector ultraviolet

quantum efficiency for two commercially available passivation treatments, IEEE Trans. Nucl. Sci. **67**(8), 1962 (2020)

[94] J.R. Janesick, *Scientific charge-coupled devices*, vol. 83 (SPIE press, 2001)

[95] J. Heymes, M. Soman, T. Buggey, C. Crews, G. Randall, A. Gottwald, A. Harris, A. Kelt, U. Kroth, I. Moody, X. Meng, O. Ogor, A. Holland, in *X-Ray, Optical, and Infrared Detectors for Astronomy IX*, vol. 11454, ed. by A.D. Holland, J. Beletic. International Society for Optics and Photonics (SPIE, 2020), vol. 11454, pp. 263 – 273

[96] R.A. Stern, L. Shing, M.M. Blouke, Quantum efficiency measurements and modeling of ion-implanted, laser-annealed charge-coupled devices: x-ray, extreme-ultraviolet, ultraviolet, and optical data, Appl. Opt. **33**(13), 2521 (1994)

[97] L. Poletto, A. Boscolo, G. Tondello, Characterization of a charge-coupled-device detector in the 1100–0.14-nm (1-eV to 9-keV) spectral region, Appl. Opt. **38**(1), 29 (1999)

[98] H. Garnir, P.H. Lefèbvre, Quantum efficiency of back-illuminated CCD detectors in the VUV region (30–200nm), Nucl. Instrum. Methods Phys. Res. B: Beam Interact. Mater. At. **235**(1), 530 (2005)

[99] D. Hemminga, O. Versolato, J. Sheil, Characterization of plasmas driven by laser wavelengths in the 1.064–10.6 μm range as future extreme ultraviolet light sources, arXiv preprint arXiv:2208.14223 (2022)

[100] Z. Bouza, J. Byers, J. Scheers, R. Schupp, Y. Mostafa, L. Behnke, Z. Mazzotta, J. Sheil, W. Ubachs, R. Hoekstra, et al., The spectrum of a 1-μ m-wavelength-driven tin microdroplet laser-produced plasma source in the 5.5–265.5 nm wavelength range, AIP Adv. **11**(12), 125003 (2021)

[101] G. Arisholm, Ø. Nordseth, G. Rustad, Optical parametric master oscillator and power amplifier for efficient conversion of high-energy pulses with high beam quality, Opt. Express **12**(18), 4189 (2004)

[102] F. Liu, D. Smeets, S. Huang, A. Yakunin, P. Havermans, R. Oesterholt, M. Bayraktar, F. Bijkerk, in *EUVL Workshop* (Berkeley, California, United States, 2019)

[103] G.F. Lorusso, N. Davydova, M. Eurlings, C. Kaya, Y. Peng, K. Feenstra, T.H. Fedynyshyn, O. Natt, P. Huber, C. Zaczek, S. Young, P. Graeupner, E. Hendrickx, in *Extreme Ultraviolet (EUV) Lithography II*, vol. 7969, ed. by B.M.L. Fontaine, P.P. Naulleau. International Society for Optics and Photonics (SPIE, 2011), vol. 7969, p. 79692O

[104] N. Davydova, R. Kottumakulal, J. Hageman, J. McNamara, R. Hoefnagels, V. Vaenkatesan, A. van Dijk, K. Ricken, L. de Winter, R. de Kruif, R. Jonckheere, T. Hollink, G. Schiffelers, E. van Setten, P. Colsters, W. Liebregts, R. Pellens, J. van Dijk, in *31st European Mask and Lithography Conference*, vol. 9661, ed. by U.F. Behringer, J. Finders. International Society for Optics and Photonics (SPIE, 2015), vol. 9661, p. 96610B

[105] M.F. Gu, The flexible atomic code, Can. J. Phys. **86**(5), 675 (2008)

[106] F. Marschall, Z. Yin, J. Rehanek, M. Beye, F. Döring, K. Kubiček, D. Raiser, S.T. Veedu, J. Buck, A. Rothkirch, et al., Transmission zone plates as analyzers for efficient parallel 2D RIXS-mapping, Sci. Rep. **7**(1), 8849 (2017)

[107] F. Marschall, D. McNally, V.A. Guzenko, B. Rösner, M. Dantz, X. Lu, L. Nue, V. Strocov, T. Schmitt, C. David, Zone plates as imaging analyzers for resonant inelastic x-ray scattering, Opt. Express **25**(14), 15624 (2017)

[108] K. Matsushima, T. Shimobaba, Band-Limited Angular Spectrum Method for Numerical Simulation of Free-Space Propagation in Far and Near Fields p. 12 (2009)

[109] F. Shen, A. Wang, Fast-Fourier-transform based numerical integration method for the Rayleigh-Sommerfeld diffraction formula, Appl. Opt. **45**(6), 1102 (2006)

[110] H.W. Schnopper, L.P.V. Speybroeck, J.P. Delvaille, A. Epstein, E. Källne, R.Z. Bachrach, J. Dijkstra, L. Lantward, Diffraction grating transmission efficiencies for XUV and soft x rays, Appl. Opt. **16**(4), 1088 (1977)

[111] K. Eidmann, M. Kühne, P. Müller, G. Tsakiris, Characterization of pinhole transmission gratings, J. X-Ray Sci. Technol. **2**(4), 259 (1990)

[112] M.M. Basko, I.P. Tsygvintsev, A hybrid model of laser energy deposition for multi-dimensional simulations of plasmas and metals, Comput. Phys. Commun. **214**, 59 (2017)

List of publications

Publications related to the chapters of this thesis:

Chapter 2:

Z. Bouza, J. Scheers, A. Ryabtsev, R. Schupp, L. Behnke, C. Shah, J. Sheil, M. Bayraktar, J. R. Crespo López-Urrutia, W. Ubachs, R. Hoekstra, and O. O. Versolato, *EUV spectroscopy of Sn^{5+}–Sn^{10+} ions in an electron-beam ion trap and laser-produced plasmas*, J. Phys. B **53**, 195001 (2020)

Chapter 3:

Z. Bouza, J. Byers, J. Scheers, R. Schupp, Y. Mostafa, L.Behnke, Z. Mazzotta, J. Sheil, W. Ubachs, R. Hoekstra, M. Bayraktar, and O. O. Versolato, *The spectrum of a 1-µm-wavelength-driven tin microdroplet laser-produced plasma source in the 5.5–265.5 nm wavelength range,* AIP Adv. **11**, 125003 (2021)

Chapter 5:

The work presented in this chapter led to the following publication: Y. Mostafa, **Z. Bouza**, J. Byers, Ievgeniia Babenko, W. Ubachs, O. O. Versolato, and M. Bayraktar, *Extreme Ultraviolet Broadband Imaging Spectrometer Using Dispersion-matched Zone Plates,* accepted for publication in Opt. Lett., (2023)

The author has also contributed to the following publications:

F. Torretti, F. Liu, M. Bayraktar, J. Scheers, **Z. Bouza**, W. Ubachs, R. Hoekstra, and O. O. Versolato, *Spectral characterization of an industrial EUV light source for nanolithography,* J. Phys. D: Appl. Phys. **53**, 055204 (2019)

O. Versolato, A. Bayerle, M. Bayraktar, L. Behnke, H. Bekker, **Z. Bouza**, J. Colgan, J. R. Crespo López-Urrutia, M. J. Deuzeman, R. Hoekstra, D. Kurilovich, B. Liu, R. Meijer, A. Neukirch, L. Poirier, S. Rai, A. Ryabtsev, J. Scheers, R. Schupp, J. Sheil, F. Torretti, W. Ubachs and S. Witte, *Spectroscopic investigations of YAG-laser-driven microdroplet-tin plasma sources of extreme ultraviolet radiation for nanolithography*, J. Phys.: Conf. Ser. 1412 192006 (2020)

L. Behnke, R. Schupp, **Z. Bouza**, M. Bayraktar, Z. Mazzotta, R. Meijer, J. Sheil, S. Witte, W. Ubachs, R. Hoekstra, and O. O. Versolato, *Extreme ultraviolet light from a tin plasma driven by a 2-µm-wavelength laser,* Opt. Express **3**, 4475–4487 (2021)

R. Schupp, L. Behnke, J. Sheil, **Z. Bouza**, M. Bayraktar, W. Ubachs, R. Hoekstra, and O. O. Versolato, *Characterization of 1- and* $2-\mu$m*-wavelength laser-produced microdroplet-tin plasma for generating extreme-ultraviolet light,* Phys. Rev. Res. **3**, 013294 (2021)

R. Schupp, L. Behnke, **Z. Bouza**, Z. Mazzotta, Y. Mostafa, A. Lassise, L. Poirier, J. Sheil, M. Bayraktar, W. Ubachs, R. Hoekstra, and O. O. Versolato, *Characterization of angularly resolved EUV emission from 2-µm-wavelength laser-driven Sn plasmas using preformed liquid disk targets,* J. Phys. D: Appl. Phys. **54**, 365103 (2021)

Acknowledgments

I'm feeling very happy that this journey has ended successfully. But this would not have been possible without the help and support of many people whom I would like to thank in this part of my thesis.

I would like to first start with my supervisors Oscar Versolato and Muharrem Bayraktar. Oscar, thanks a lot for the opportunity to join your group and for always being present anytime that I needed help or guidance. Muharrem, even if we were working together from distance with you being in Enschede and me in Amsterdam, you were always managing to make time for me and help me anytime I asked for it. Thank you both for offering me the chance to do this PhD research but mostly for your encouragement and for teaching me so many things within but also outside the research. It was very nice for me to bring closer ARCNL and UT via this project. I would like to also thank you for your understanding and for your respect at all my needs these years and especially the last months of my PhD, I really appreciate it. I would also like to thank Wim and Ronnie for their contributions on my research.

To all of my colleagues, Yahia, Lucas, Lars, Bo, John, Diko, Ruben, Joris, Jane, James, Randy, Edcel, Alex, Javier, Dion, Karl, Stan, Adam, Youssef, Dmitry, Francesco - thank you. I learned a lot from all of you and I really enjoyed your company inside and outside of ARCNL. I would like to especially thank my colleague and friend Yahia who made my days at ARCNL look way better since he came. I really enjoyed our conversations and I will miss them. Thanks a lot for always being there and for making my work way simpler by creating all these python codes.

For their major technical contributions, I would like to thank Laurens, Henk-Jan, Iliya, Ricardo, Caspar, Boris, Marco and Jorijn.

Special thanks to all the ARCNL people and especially the management team and the support staff.

For the needs of my PhD research I had the luck to collaborate with a few people from ASML and TNO. I would to thank everyone who involved on this and for the opportunity to run some experiments in their laboratories.

To my friends Lena, Alex, Georgia, Robin, George, Rafaela, Dora, Katerina, Thanasis, Emy, Stefania, Tasos, Magda, Maria, thanks for your support. Lena and Alex you are family to me - thanks a lot for all your encouragement and for being on my side the good but also the bad times. Georgia, we grew up together and we still are, thanks for that. Robin you are my Dutch family, thanks for everything. George, thanks for making me laughing. Rafaela, thanks for your cheerful presence anytime you are around. Dora, thanks for being such a good friend. Katerina and Thanasis thanks for sharing your time with us but also so many other things the last months. Katerina you were my belly buddy the last months. Emy, thanks for our long discussions. Stefania and Tasos thanks for making the last months look better in the Netherlands. Magda, thanks a lot for the encouragement and for the inspiration. Maria, thanks for your company all these years.

To my parents Dimitra and Kostas thank you so much for your love and for your support on every choice I made in my life. I'm very grateful for the way you raised me and always taking care of me. Mom, thanks for teaching me how to become a better mother for my child.

To my sisters Popi and Sia, thanks for always being there for me. You are both mothers and friends to me.

To my nephew Giannis and my niece Dimitra - thanks for making my life happier. I'm very proud of you and for the way I see you growing up. I will always be there for you.

Last but not least, to my life partner Christos. Thanks for sharing your life with me all these years and for making me happier and stronger. Without you many of my succeeds would not have happened. This year you also offered me the biggest gift of my life, our beautiful daughter Myrto. My lovely girl, thanks for bringing so much light in our life! You came on the very best moment and made everything look way happier and easier! Christos, Myrto, I'm very happy for our family and I am looking forward for the coming moments with both of you!

Zoi Bouza
July 2023, Amsterdam

Developments for broadband spectral and spatial characterization of tin plasma light sources for EUV lithography